Technische Universität München

Fakultät für Chemie

Lehrstuhl II für Technische Chemie

Impact of hydrothermal synthesis parameters on activity and stability of Mo-V mixed oxide catalysts for oxidative dehydrogenation of ethane

Daniel Markus Melzer

Vollständiger Abdruck der von der Fakultät für Chemie der Technischen Universität München zur Erlangung des akademischen Grades eines

Doktor-Ingenieurs (Dr.-Ing.)

genehmigten Dissertation.

Vorsitzender:		Prof. Dr.-Ing. Kai-Olaf M. Hinrichsen
Prüfer der Dissertation:	1.	Prof. Dr. Johannes A. Lercher
	2.	Prof. Dr. Ewald Werner

Die Dissertation wurde am 21.10.2019 bei der Technischen Universität München eingereicht und durch die Fakultät für Chemie am 30.03.2020 angenommen.

It was the tension between these two poles - a restless idealism on one hand and a sense of impending doom on the other - that kept me going.

Hunter S. Thompson, The Rum Diary

Meiner Familie

Statutory Declaration

I declare that I have authored this thesis independently and that I have solely used the declared (re)sources and that I have marked all material, which has been quoted either literally or by content from the used sources. At the end of each chapter all collaborators are named and their specific contribution is addressed. Published content of this thesis is clearly marked.

Kufstein, October 11th, 2019

Daniel Melzer

Acknowledgments

This thesis marks the end of five years of hard work and thought. And although it bears only my name on it, I could never have done it on my own. Therefore, I want to take the chance to say "thank you" to all of you who have accompanied and supported me along the way.

First and foremost, I would like to thank Prof. Johannes A. Lercher for giving me the opportunity to pursue my doctoral studies in his group. Johannes, thank you for interest, support, guidance and patience in me and my work. You offered me the chance to work on an exciting topic and let me become the scientist I am today. Working in your diverse and international group was a great lesson by its own. You taught me to present and stand up for my results, and after all those discussions we had, I agree with you: In the end, it was big fun!

My sincere thanks also belong to Dr. Maricruz Sanchez-Sanchez. Maricruz, thank you for your everyday help on "doing the science". I could not have asked for a better supervisor given your superb knowledge on $MoVTeNbO_x$ chemistry as well as your scientific rigor and support in phrasing our findings. Your contribution to all those reports, presentations, manuscripts and finally this thesis was invaluable. *¡gracias por todo!*

The ODH project was not a one man show. Dr. Philipp Donaubauer was my partner in crime throughout the years. Philipp, you were the best teammate I could wish for. Thanks for always having an open door and open ear for me. I really appreciated our continuous discussions on all scientific and not-so scientific issues, help in data analysis, running the reactor as well as doing the dishes after every Clariant meeting. I would also like to thank the rest of the LOC team, Dr. Felix Kirchberger and Sebastian Standl, for their support, friendship and especially the LOC Weihnachtsfeiern.

Next to being a team effort of PhD students, the ODH project was not only an academic exercise but lived cooperation between university and industry. I thank Clariant Produkte (Deutschland) GmbH, in particular PD Dr. Gerhard Mestl, Dr. Klaus Wanninger and Prof. Dr. Richard Fischer. Thank you for sharing all your expert knowledge with me and your continuous encouragement. Seeing how relevant my work for this team was, was an everlasting source of motivation.

Abstract

Direct crystallization of M1 phase Mo-V mixed oxide catalysts under hydrothermal conditions has been realized by enabling the formation of polyoxometalate intermediates, while avoiding precipitation of amorphous solid. Particles synthesized under such conditions exhibit crystal terminations with high density of active sites, resulting in exceptionally high ethane oxidative dehydrogenation rates. The presence of Te and Nb leads to higher concentration of M1 nanocrystals and reduces the concentration of oxygen species that cause total oxidation of ethene.

Kurzzusammenfassung

Die direkte Kristallisation von M1-Phasen-Mo-V-Mischoxidkatalysatoren unter Hydrothermalbedingungen wurde durch Bildung von Polyoxometalat-Zwischenstufen und gleichzeitiger Vermeidung des Ausfallens von amorphem Feststoff ermöglicht. Partikel, die unter solchen Bedingungen synthetisiert werden, zeigen an ihrer Kristalloberfläche eine hohe Dichte aktiver Zentren. Dies hat außergewöhnlich hohe Raten der oxidativen Dehydrierung von Ethan zur Folge. Die Gegenwart von Te und Nb resultiert in einer höheren Konzentration an M1-Nanokristallen und einer niedrigeren Konzentration an Sauerstoffspezies, welche für die Totaloxidation von Ethen verantwortlich sind.

Table of Contents

1 Introduction

Light olefins and selective oxidation products are among the most important and demanded intermediates in chemical industry. Abundant amounts of small alkanes become available with increasing natural gas production from unconventional reserves. Catalytic oxidative dehydrogenation and oxo-functionalization are highly promising options for the valorization of those alkane feedstocks.

This chapter introduces the state of art production technologies for light olefins, focusing on the production of ethene. Catalyst systems for the oxidative dehydrogenation of ethane are introduced and special focus is put on the crystalline M1 phase of Mo-V mixed metal oxides.

1.1 Industrial practice of dehydrogenation and selective oxidation of small alkanes

The availability of the light alkanes has significantly increased over the past decade with a rise in exploitation of unconventional gas resources. This surge is mainly focused on the U.S. (Figure 1) and Canada, but limited production rise is also observed for example in Argentina, China or New Zealand [2]. The gas from unconventional sources, often also termed "shale gas", contains a large fraction of liquid gas components (i.e. light alkanes ethane, propane and butanes), in some cases accounting for up to 20 vol.-% [3].

The corresponding $C_2 - C_4$ light olefins are the most wide-spread intermediates in chemical industry with ethene and propene being worldwide the number one and two (by tonnage) petrochemical products produced [4-6]. Ethene and propene are the raw materials for synthesis of polyethylene and polypropylene plastics, accounting for 60 % [7] and 66 % [8] of their annual use. But they also serve as precursors in the production of numerous bulk chemicals, such as ethylene oxide, acrylic acid or acrylonitrile, and further commodities [4,6].
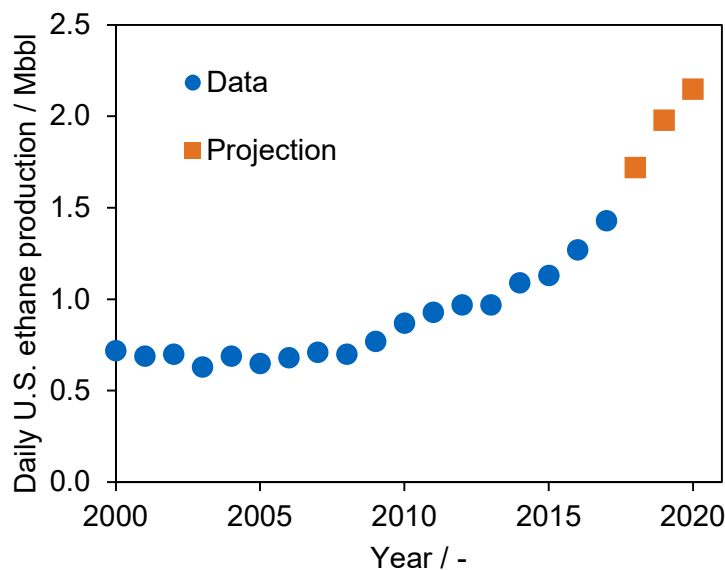
Figure 1: Daily U.S. ethane production [9].

The current main production route for those olefins, in particular ethene, is thermal (steam) cracking of hydrocarbons, i.e. their thermal pyrolysis. While traditionally larger hydrocarbon feedstocks were used (naphta cracking), the current fashion turns to cracking of abundant ethane (gas cracking). This route yields almost exclusively ethene with minimal by-production of other hydrocarbons, carbon oxides and cocking [10,11].

Typical gas cracker units consist of two sections: The pyrolysis section with the reactors for the thermal reaction and the recovery section for product separation and purification. In the process, the preheated hydrocarbon feed is mixed with hot steam and lead through gas fired tube bundles. The cracking reaction takes place at about 750 – 875 °C with a residence time of about 0.1 – 0.5 seconds [6,12]. The high reaction temperature is necessary due to the endothermicity of alkane dehydrogenation (Equation (1)).

$$C_2H_6 \rightarrow C_2H_4 + H_2 \qquad\qquad \Delta H_R^0 = 136 \text{ kJ mol}^{-1} \qquad (1)$$

The chemical reaction itself follows a radical mechanism in which the primary reaction is initiated by thermal scission of the alkane C-C bonds. This radical reaction mechanism requires the gas stream to be rapidly quenched to temperatures below 650 °C after the reactor exit to avoid product degradation by further secondary reactions. Quenching is performed by heat exchange with pressurized water and the heat can in part be recuperated in the form of high-pressure superheated steam [6].

Despite the huge investment costs (typically more than $2 bn [13]) and high energy demand due to high reaction temperatures requiring to work at large plant capacities (economy of scale) within highly integrated petrochemical complexes, the worldwide steam cracking capacity is rising [14]. The strong localization of steam cracking facilities within chemical complexes often near costal lines however conflicts with the locally dispersed availability of small shale gas reserves in remote areas (Figure 2).
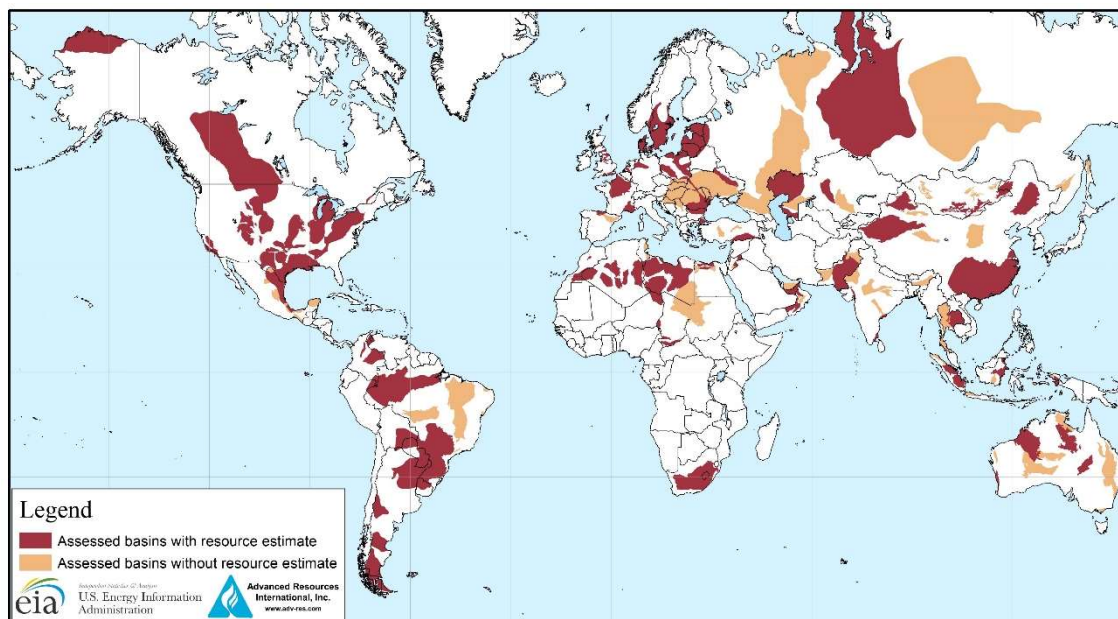
Figure 2: Geographical location of proven shale gas resources as of 2015 according to U.S. Energy Information Administration (U.S. EIA) [15]. Red color indicates areas with resource volume estimate, orange such areas without resource volume estimate.

While the commercially established steam (gas) cracking is the single benchmark technology any alternative olefin production process needs to compete with, these conflicts and the disadvantages of steam cracking have spiked interest in alternative olefin production processes. One of such alternatives is the catalytic oxidative dehydrogenation (ODH) of alkanes, especially of ethane (ODH-E, equation (2)).

$$C_2H_6 + \frac{1}{2}O_2 \rightarrow C_2H_4 + H_2O \qquad \Delta H_R^0 = -105 \text{ kJ mol}^{-1} \qquad (2)$$

ODH-E has some significant conceptual advantages over steam cracking (and the direct catalytic dehydrogenation over noble metal catalysts, which discussion is beyond the scope of this thesis). The formal oxidation of the byproduct hydrogen makes the process overall exothermic. This allows to recover energy from the process and -at the

prerequisite of a suitable catalyst- to work at significantly lower temperatures of 300 – 600 °C [10,16]. The lower energy input required may allow construction of ODH plants with much lower capacity compared to steam crackers, hence reducing the investment cost and enabling plant construction independent from larger chemical complexes near the ethane production site [17,18].

On the downside, thermodynamics drive the exothermic ODH reaction towards full combustion of ethane, i.e. unwanted CO_x formation. Heat management and process control are therefore of vital importance to make the process feasible. Different reactor concepts have been discussed in this context, ranging from conventional fluidized bed [19,20] and tubular reactors [20,21], possibly with zoned catalyst beds [22], over staged feed concepts [17,23] to more advanced systems like membrane reactors [24,25]. Also, replacement of oxygen with milder oxidants like CO_2 has been discussed [17,26-28], yet seems further away from industrial applicability.

The feasibility of ODH-E processes largely results from a lowered energy input required in comparison to the established steam cracking. This requires on the one hand highly active catalysts to achieve high single pass yields at moderate temperatures and on the other hand high olefin selectivity to maximize carbon efficiency. There are several different promising catalyst systems discussed in scientific and patent literature for application in ODH-E. Three of those groups will be presented in the following:

- Supported and unsupported transition metal oxides
- M1-type mixed metal oxides,
- Alternative systems (alkali oxides and chlorides and boron catalysts)

1.2 Supported and unsupported transition metal oxides

The most prominent ODH catalysts are transition metal oxides, either supported or as bulk materials. Among those, Ni, Mo and V single or mixed metal oxides are the most frequently reported. ODH reaction on this type of (mixed) metal oxide catalysts is commonly described as a redox process following a Mars-van-Krevelen mechanism [29-31]. This is that lattice oxygen from the oxide (or respective other heteroatoms in case of e.g. sulfide or nitride catalysts) is incorporated into the reaction product and the resulting vacancy is replenished by gas phase oxygen.

Catalyst properties affecting partial oxidation product selectivity over transition metal oxide catalysts were laid out by Grasselli as "the seven pillars of oxidation catalysis" [32].

Suitable redox properties of isolated sites must meet with proper bond strength of lattice and adsorbed oxygen species to realize high selectivity. The nature of oxygen species involved in partial and total oxidation of hydrocarbons was also discussed to great detail by Bielański and Haber [33,34]. Oxygen surface species can be divided into two groups: Nucleophilic "selective oxidation" sites catalyzing hydrogen abstraction and oxygen addition on the one hand and electrophilic sites catalyzing oxygen insertion into electron-rich hydrocarbon bonds, thus facilitating total oxidation. The former group of electron-rich species comprises O^{2-} ions such as terminal and bridging lattice oxygen. On the other hand, the latter group includes electron-poor species such as per-oxo radical O_2^{2-} or mono-oxygen radical O^-. The concept of electrophilic and nucleophilic oxygen can be described in other terms as interaction between Lewis basic oxygen and Lewis acidic metal cations. Ratio of oxygen basicity and metal cation acidity is reflected in the metal-oxygen bond strength and thus lability and readiness of oxygen to undergo surface reactions.

Catalytic dehydrogenation activity of redox active catalysts is commonly attributed to O^- radical species [35]. Their exact nature, activity, stability and formation route however depends on the metal oxide composition. Generally speaking, O^- radicals result from electron transfer from lattice oxygen to holes (Equation (3)). Those holes may be caused by cationic vacancies in *p*-type semiconducting materials or deficiency of lattice O^{2-} anions in *n*-type semiconductors.

$$O^{2-} + h^+ \rightarrow O^- \tag{3}$$

Supported [36] or pure bulk NiO [37-39] exhibits reasonable catalytic activity in the conversion of ethane reaction. However, especially bulk NiO shows poor selectivity towards ethene ($S_{C2H4} \approx 20\%$ at $X_{C2H6} \approx 10\%$) [37,38]. Both activity and selectivity for ethene production can be enhanced by the addition of high valence promoter metals. Among a series of possible promoter metals with different valence (Li, Mg, Al, Ga, Ti, Ta, Nb), Nb was identified as the best candidate, increasing ethene selectivity to more than 90 % at otherwise identical conditions [37,38]. Nb replaces Ni positions in the NiO framework forming solid Ni-Nb mixed metal oxide solutions. Nb acts in those mixed metal oxide systems as electron donor and thus reducing the availability of electrophilic oxygen species catalyzing the total oxidation of the alkane [37,38,40].

Similar to Ni, Mo and V single or mixed metal oxides are well known oxidation catalysts [22,41-43] and they also catalyze the oxidative dehydrogenation of alkanes [44-59]. Promotion

of VO_x/Al_2O_3 catalysts with separate MoO_x moieties without formation of mixed metal oxide phases results in higher propane ODH activity compared to the pure VO_x/Al_2O_3 system due to enhanced alkane adsorption [55,60]. Isotopic labelling studies by the Iglesia group show that propane ODH proceeds along the same pathways over alumina supported Mo and V oxide catalysts [48,50]: 1) The alkane adsorbs non-dissociatively on a lattice oxygen atom, 2) C-H bond cleavage occurs through H abstraction by a neighboring lattice oxygen forming a first hydroxyl group, 3) β-hydride elimination forms a second hydroxyl group and the olefin desorbs, 4) recombination of two hydroxyl groups releases H_2O and forms a reduced metal center, 5) the spent (reduced) metal center is re-oxidized by dissociative adsorption of gas phase oxygen. Equivalent reactions were proposed also for ODH of ethane [45]. Figure 3 illustrates these pathways using ethane as example of the alkane and terminal oxygen as example of lattice oxygen sites.
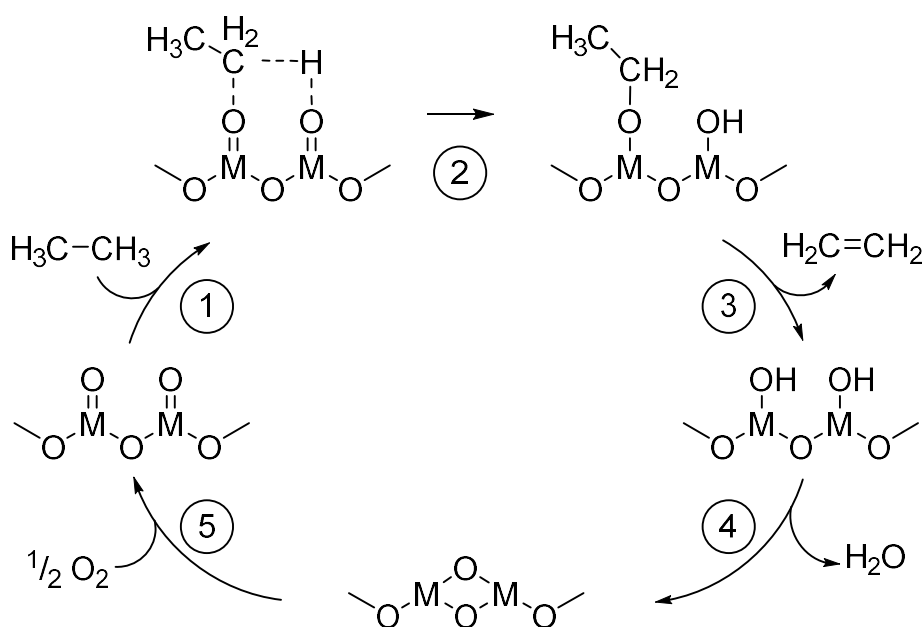
Figure 3: Catalytic cycle of alkane ODH as proposed by the Iglesia [45,48,50]. M indicates V or Mo metal centers.

Kinetic isotope effect studies comparing the reactivity of protonated and deuterated ethane and propane indicate that the first C-H rupture is the rate determining step and that this bond scission is irreversible for both alkanes. The transition state of the C-H cleavage step includes an electron transfer from the oxygen to a metal center and alkane conversion. [45,48,50]. Also, mixed isotope molecular oxygen was not observed when feeding $^{18}O_2$, indicating irreversible oxygen dissociation [48,50]. Alkane conversion activity

was found to correlate with the reducibility of the vanadium oxide [46,61]: Higher reducibility coincides with higher reactivity of the oxide.

1.3   M1 phase Molybdenum-Vanadium mixed metal oxides

While transition metal oxides dispersed on a support material serve as excellent models in studying reaction mechanism and the influence of physico-chemical surface properties on the reactivity of light alkane oxidation, bulk mixed metal oxides show superior activity [62]. Thorsteinson *et al.* were the first authors in 1978 to report the use of bulk Mo-V-M (M = Ti, Cr, Mn, Fe, Co, Ni, Nb, Ta, or Ce) mixed metal oxides for the oxidative dehydrogenation of ethane [63]. Making use of an aqueous phase evaporation method, they obtained bronze-like materials characterized by a 4.00 Å layering. The most efficient unsupported catalyst was $MoV_{0.25}Nb_{0.12}O_x$ with an onset of ethane conversion observed at 215 °C and reaching 10 % hydrocarbon conversion without formation of side products at 286 °C. A linear correlation between catalytic activity and intensity of the 4.00 Å diffraction, i.e. phase content of bronze-like mixed metal oxide phase, was found.

The next step in development of Mo-V mixed metal oxides doped with other transition metals as catalysts for ODH-E was taken in 1993 by Mitsubishi chemicals [64]. $MoVTeNbO_x$ mixed metal oxides, previously applied for propane-to-acrylic acid oxidation [65] and propane-to-acrylonitirile ammoxidation [66], showed also high catalytic activity for the dehydrogenation of ethane. These Mo-V-Te-Nb mixed metal oxides were shown to contain mostly two crystalline phases: Orthorhombic M1 phase and pseudo-hexagonal M2 phase [67].

The M1 crystal phase (ICSD pattern no. 55097) of mixed Mo-V oxides has been recognized as the most active and selective catalyst system for ODH-E of all (mixed) transition metal oxide catalysts [62,68-71]. Since the pioneering works of Thorsteinson [63] and Mitsubishi Chemicals [64] , it has attracted a lot of attention and initiated further research by academia and industry. This section focuses on the current understanding of the crystal chemistry and synthesis, the structure-activity correlations and mechanism of the ODH reaction on this catalyst.

1.3.1 Crystal structure of M1 and related phases

M1 phase exhibits an orthorhombic crystal structure with *Pba2* symmetry and lattice parameters $a = 21.134(1)$ Å, $b = 26.647$ Å and $c = 4.0140(2)$ Å [72]. The basal {001} (i.e., the *a-b*) plane (Figure 4) consists of edge and corner sharing distorted metal-oxygen octahedra [73]. Crystallographic sites S1 to S11 (framework sites) are occupied by Mo and/or V. Both elements are present in both their highest and partially reduced oxidation state. Distortion of Mo and V octahedra was shown to directly correlate with their respective oxidation state [73]. In Ta and Nb containing variants, those elements occupy the pentagonal crystal site S9 [74-76]. Connection of pentagonal units (S5, S6, S8 – S11, orange circles) by S1 octahedra and pentameric S2-S4-S7 ensembles results in six- and seven-membered rings. Those rings (sites S12 and S13) are (partially) occupied by TeO or SbO entities in the respective variants [77]. Originally, the phase stoichiometry was postulated as $Mo_{7.8}V_{1.2}NbTe_{0.937}O_{28.9} = MoV_{0.15}Te_{0.12}Nb_{0.13}O_{3.71}$ [78], but it was shown that chemical flexibility of the systems allows for other mixed site occupancies [72,78-80]. Repetitive stacking of the unit cell structure in direction of the crystal *c*-axis results in hexagonal and heptagonal channels parallel to this direction. M1 crystals typically show elongation along their *c*-axis direction.
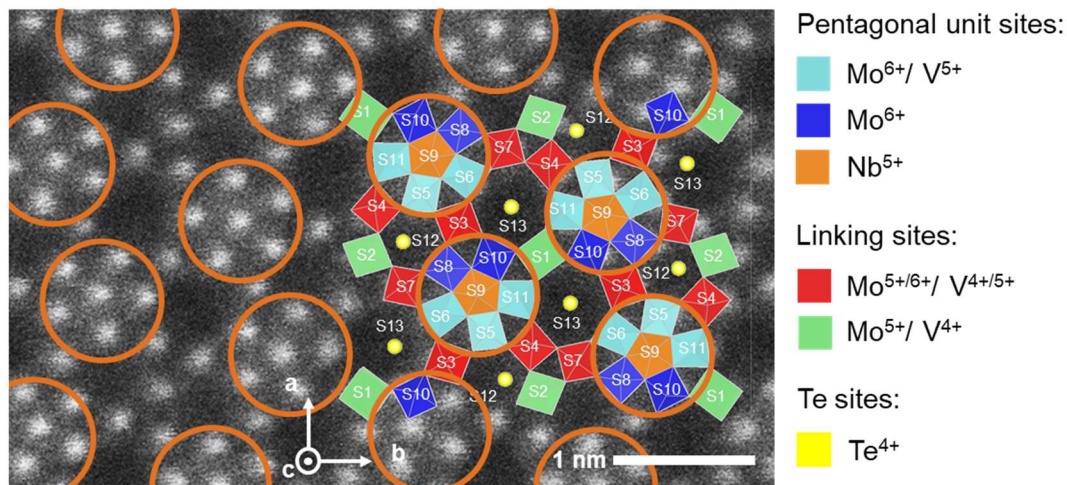
Figure 4: Projection of 2x2 unit cells representation of M1-MoVTeNbO$_x$ crystal phase viewed along the *c*-axis on a HAADF-STEM image of M1 *a-b* plane. Different colors of crystallographic sites indicate occupancy by different metals and oxidation states. Orange circles highlight pentagonal building blocks. Adapted and reproduced from reference [81] under Creative Commons Attribution 4.0 International License with kind permission of Nature Publishing Group.

M1-MoVTeNbO$_x$ crystalline phase is frequently accompanied by other mixed metal oxide phases, and especially the chemically and structurally closely related M2 (ICSD no. 55098) and M$_5$O$_{14}$ (M = Mo, V, Nb; ICSD no. 27202) phases (Figure 5). M2 phase is characterized as an "orthorhombically distorted hexagonal tungsten bronze"[82] with *Pmm2* space group and lattice parameters *a* = 12.6294(6) Å, *b* = 7.29156(30) Å and *c* = 4.02010(7) Å [78]. Its nominally stoichiometry is Mo$_{4.31}$V$_{1.36}$Te$_{1.81}$Nb$_{0.33}$O$_{19.81}$ [78]. In accordance, the content of Te is usually considerably higher compared to M1 phase [78]. In contrast to M1 phase, only six membered rings are formed within the {001} plane by exclusively corner sharing metal octahedra. As in M1 phase, repetitive stacking of unit cell layers along the *c*-axis results in a channel structure. These channels are partially occupied by Te.

M$_5$O$_{14}$ is a partially V and Nb substituted variant of Mo$_5$O$_{14}$ with triclinic *P4/mbm* space group and lattice parameters *a* = *b* = 22.995 Å and *c* = 3.937 Å [83]. It shares the pentagonal M$_6$O$_{21}$ unit with M1 phase (orange circles in Figure 4) and the bronze-typical layered structure along its *c*-axis. However, it does not form a channel structure like M1 or M2.
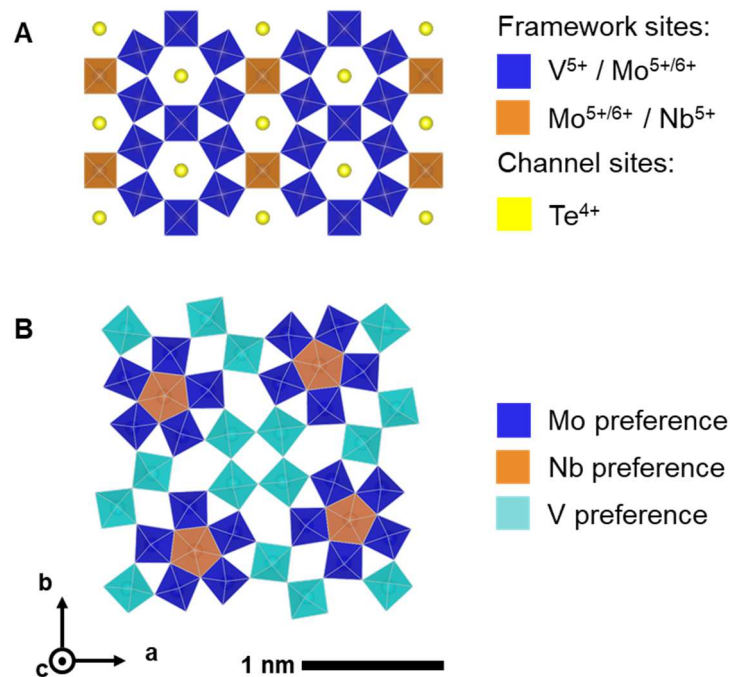
Figure 5: 2x2 unit cells representation of M2-MoVTeNbO$_x$ (A) and single unit cell of (Mo,V,Nb)$_5$O$_{14}$ (B) crystal phases viewed along their *c*-axis. Different colors of crystallographic sites indicate occupancy by different metals and oxidation states.

1.3.2 Synthesis of M1 phase

There are multiple possible synthesis methods for M1 phase and numerous elemental variants reported, ranging from bimetallic Mo-V [84-86], over ternary Mo-V-Te [87,88] and Mo-V-Nb [89] to quaternary Mo-V-(Te,Sb)-(Nb,Ta) [74,76,90,91]. Quaternary systems are the most active and selective variants, making their synthesis the most widely studied. The original synthesis of Mitsubishi was an evaporation method starting from aqueous solutions of ammonium heptamolybdate $(NH_4)_6Mo_7O_{24}$, ammonium metavanadate $NH_4V_3O_4$, telluric acid $Te(OH)_6$ and other transition metal salts [64]. Other synthetic approaches are spray drying of aqueous metal salt solutions [92,93] and, by now the most frequently reported option, hydrothermal synthesis [94]. All synthesis methods have in common that the initial mixing and ageing (evaporation, drying, hydrothermal synthesis) step yields an X-ray amorphous mixed metal oxide ("precursor"). Crystallization occurs only upon thermal treatment in oxidizing and/or inert atmosphere at temperatures up to 650 °C [1,95-100]. Different methods for post-synthetic treatment were investigated to increase catalytic performance of M1-type Mo-V mixed metal oxides. Catalytically inactive M2 and amorphous phases can be selectively removed by steaming, washing with oxalic acid or hydrogen peroxide [91,97,101-103]

Typically, during the hydrothermal synthesis step of MoVTeNbO$_x$, an aqueous mixture of the metal salts is allowed to react for at least 24 h at temperatures between 110 °C and 175 °C [1]. The resulting precursor oxide is filtered from the slurry, washed and dried. During the hydrothermal synthesis step, metals are not fully incorporated in the precipitate and a certain amount of them remains solvated in the liquid phase. Phase composition of the final product depends delicately on the synthesis duration [104], pH value of initial synthesis mixture [105-107] and conditions during the annealing step [1,96]. M1 phase content was found to increase with longer synthesis durations. At short synthesis durations Mo_5O_{14}-type phase prevails [104]. The sensitivity of M1 formation and its precursors is good in agreement with the strong dependency of molybdate speciation to temperature, concentration and pH [108].

Chemical processes during hydrothermal synthesis of M1 phases have been investigated by the groups of Ueda [105-107,109,110] and Schlögl [1,104,111]. By probing of the synthesis slurries using *in-situ* Raman [104] and UV-vis spectroscopy [106] {Mo$_{72}$V$_{30}$}-type Keplerates were found in Mo and V containing solutions. These ball-shaped polyoxometallates contain 12 M_6O_{21} units (M = Mo and possibly Nb) which are structurally identical to the pentagonal building block of M1 phase (orange circles in Figure 4). These M_6O_{21} units are connected by reduced {V} centers. Addition of Te leads

to decomposition of the Keplerates and formation of various heteropolyanions [112]. During heating and isothermal stage, the decomposed heteropolyanions are believed to precipitate and re-condensate to the nano-structured precursor material. [104]. In case of pure Mo-V M1 phase, no reaction intermediates other than $\{Mo_{72}V_{30}\}$ were identified [106]. Pre-formed $\{Mo_{72}V_{30}\}$ [109] or structurally similar $\{Mo_{132}\}$ Keplerates [112], in which single linking octahedra positions are replaced by dimeric linkers [113,114], were also successfully used in the synthesis of M1-MoVSbO$_x$ and M1-MoVTeO$_x$. M_6O_{21} building blocks preferentially attach to the basal {001} plane of M1 crystals, explaining their anisotropic growth along the *c*-axis [115].

1.3.3 Catalytic functionality of M1 phase for alkane oxidation

M1 phase is known as an excellent catalyst for selective oxidation and ammoxidation reactions of ethane [88,97,116-118], propane [67,119-126] and butanes [89,127-129]. Oxidation of higher hydrocarbons and oxygenates [92,130-132] was also investigated.

The mechanism of (amm)oxidation reactions over Mo-V mixed metal oxides, including M1 and M2 phases, remains not fully understood to the present date. Phase cooperation effects between M1 and M2 phase were proposed for the mechanistically more complicated ammoxidation reactions of propane [91,133], but will not be further discussed here to keep the focus on ODH of lower alkanes. Further complication is added by the complex crystal structures. Owing to this, the location and exact nature of the active site has not been resolved so far.

It is generally agreed that M1 phase is the only crystalline structure being able to activate alkanes by initial abstraction of the first hydrogen atom [134]. Its catalytic activity was found to linearly correlate with the V^{5+} surface content [135]. This led to the generally accepted conclusion, that similar to other vanadium oxidation catalyst, vanadyl $\{V^{5+}=O \leftrightarrow V^{4+}\text{-}O\cdot\}$ surface species are responsible for the hydrogen abstraction step [136,137]. Doping of M1 phase with Bi or CeO_2 was proposed to increase ODH activity by increasing the V^{5+}/V^{4+} ratio [138,139].

Initial proposals located the active site on the basal {001} plane of M1 [136]. Later, it was found that also lateral surfaces contribute to catalysis [140]. Sites on the lateral surface did not show different selectivity from those on the basal plane. Schlögl [141] and Grasselli [142] suggested that the active center is located in the pentameric crystallographic ensemble of S2-S4-S7 sites and it interacts with Te in surrounding channel sites S12 and S13 of M1-MoVTeNbO$_x$ phase (Figure 4).

There have been also alternative active sites been proposed in literature: Ueda *et al.* proposed sites within the heptagonal channel as location of catalytic reaction [86,117,143,144], where catalytic activity benefits from constraint effects [145]. Goddard *et al.* proposed application of their reduction-coupled oxo-activation (ROA) mechanism [146,147] to selective oxidation of alkanes. They suggest that Te=O species located in position S12 abstracts the allylic hydrogen from the alkane.

In a recent study, it was found that ODH-E performance directly correlates with crystal particle termination [148]. Only crystallographic planes exposing the full pentameric ensemble of S2-S4-S7 sites or parts of it are active in ethane dehydrogenation. Such planes include basal {001} plane, but also lateral planes such as {120} or {210}. In contrast, planes exclusively formed of $Nb(Mo,V)_5O_{21}$ units linked single octahedra S1 (such as {010}) were proven catalytically inactive (Figure 6). Additional activity can result from surface defects in the idealized facets. Relative abundance of planes, and hence contribution to overall activity, was found to depend on the morphology of M1 crystals. Crystals with rod-like shape (Figure 7B) were found to contain a higher fraction of active surfaces and hence being more active compared to flattened particles (Figure 7A). These findings agree therefore best with the active centers proposed by Schlögl [141] and Grasselli [142].
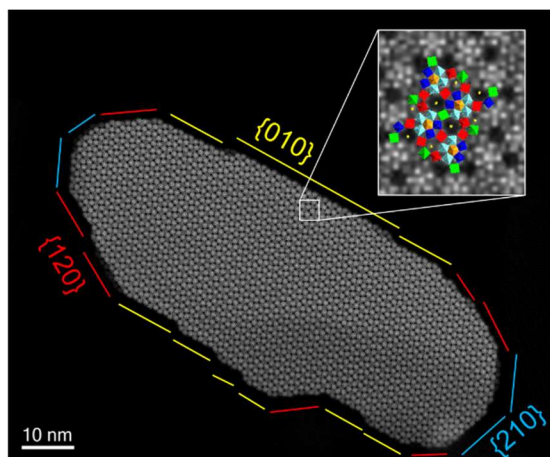
Figure 6: Illustration of terminating planes found on lateral surface of M1 crystals. Different colors indicate different families of crystallographic planes according to color code given in the Figure. Reproduced from reference [148] with kind permission of Wiley-VCH, Weinheim.
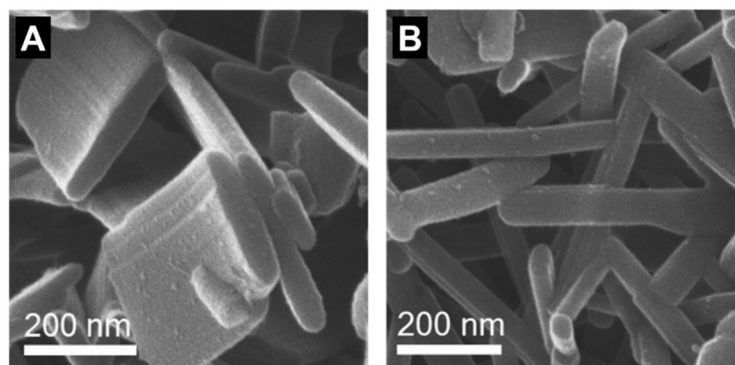
Figure 7: He ion microscopy images of particles with flattened (A) and rod-like (B) morphology. Reproduced from reference [148] with kind permission of Wiley-VCH, Weinheim.

It is generally agreed that alkane selective oxidation follows a Mars-van-Krevelen-type (MvK) mechanism on vanadium based catalysts [22,42,149]. This type of mechanism has also been proposed for M1 phase. As would be expected for the MvK mechanism, reaction orders of alkane oxidation are usually reported to be close to unity in the hydrocarbon and roughly zero in oxygen [150-152]. This points to hydrogen abstraction being the rate determining step in ODH and fast re-oxidation of M1. Several reaction networks for the oxidation of ethane and propane have been postulated [119,153,154], including direct pathways from the alkane to the corresponding olefin and CO_x, deep oxidation pathways from the olefin to CO_x and secondary oxidation of the olefin to oxygenates (mostly acids). Figure 8 shows an exemplary network from reference [153].
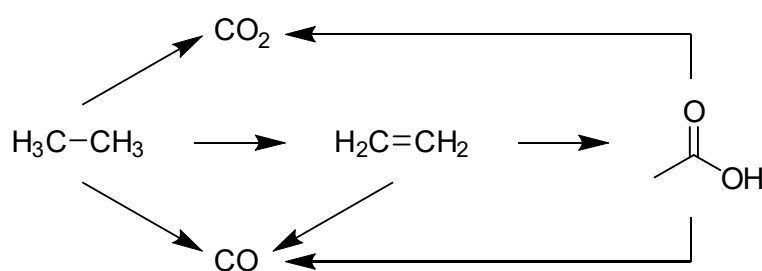
Figure 8: Reaction network of ethane oxidation over M1-MoVTeNbO$_x$ according to reference [153].

M1 mixed oxides are semiconductors with their type depending on the metal stoichiometry [155-157]. MoVTeNbO$_x$ is a *p*-type semiconductor, while MoVO$_x$ is *n*-type. Electronic properties were shown to dynamically respond to gas phase composition and thereby inducing shifts in product distribution. NAP-XPS showed that addition of steam to an propane/oxygen feed leads to an increase in V^{5+} and Te^{4+} content on the surface of M1-MoVTeNbO$_x$, reduced conductivity and surface polarity as well as parallel increase in conversion and acrylic acid selectivity [158]. The work function (i.e. surface polarity) and conductivity were also found to depend on the hydrocarbon chain length, with conductivity being higher and work function lower for the longer alkane [157].

1.4 Other solid catalyst systems

Supported alkali oxides are active in the ODH of ethane. The most studied system of this class is Li$_2$O supported on MgO [159-161]. [Li$^+$O$^-$] pairs are suggested as the site being active in the initial abstraction of hydrogen from the alkane [160,162]. Whether the alkane activation occurs via homolytic or heterolytic C-H scission has not been unequivocally established. Also, the exact location of the active sites -if in Li$_2$O domains or at the metal-support interface- is not fully clear, as Li$^+$ incorporated into the MgO bulk is also known to be active and selective [163]. [Li$^+$O$^-$] pairs catalyze the ODH reaction via a non-redox pathway [160,164], thereby acting as a radical initiator to a gas phase radical chain mechanism similar to the one occurring in steam cracking [159,160].

Addition of an alkali chloride [165-167] or bromide [168] overlay to Li$_2$O/MgO catalysts or its total replacement by alkali halogenides increases the selectivity of those materials. It needs to be noted that alkali chlorides form a melt at typical reaction temperature (ca. 600 °C). Ethene selectivity shows an inverse relationship with melting temperature of the alkali chloride, thus resulting in enhanced selectivity over eutectic systems like Li-K-Cl, Li-Na-Cl, Li-Sr-Cl and Li-Ba-Cl supported on Dy$_2$O$_3$ doped MgO [169]. Gas phase O$_2$ dissolved in the alkali chloride melt and oxidized on the melt/alkali oxide interface is hypothesized to form ODH active OCl$^-$ hypochlorite anions [170]. OCl$^-$ accordingly breaks the C-H bond via a redox process with the exact mechanism still being debated [171].

The most recently discovered ODH catalysts are boron containing systems. The initial serendipitous finding [172,173] by the Hermans group spiking research into this direction was the activity of boron nitrides (hexagonal phase and nanotubes) at temperatures below 500 °C. Using those catalysts in ODH of propane, combined olefin selectivity of propene and ethene exceeded 90 % at 14 % propane conversion level [173]. The only observed

side product was CO_x. Boron nitride was also found active in the dehydrogenation of ethane [174] and butanes [175]. ODH activity is also observed over other boron compounds (B_4C, TiB_2, NiB, WB, HfB) and elemental boron itself [176]. Surfaces of boron compounds are highly enriched in B [176] and readily oxidized under reaction conditions [173,177]. Density functional theory (DFT) calculations suggest high activity of boron edge sites in oxygen dissociation [178].

1.5   Scope of this thesis

The research project presented in this thesis aims to deepen the understanding of structure-activity correlations on ODH-E over M1 phase Mo-V mixed metal oxides. In order to achieve this, a synthesis method must be developed to enable a controlled incorporation of metals into the mixed oxide and thus allowing to deliberately tune metal stoichiometry over a broad range of concentrations. The access to different variants of M1 compositions together with kinetic tests, microscopic and physico-chemical and surface analyses is envisioned as a tool to gain further insight into the mechanism of oxidative dehydrogenation of ethane.

The results of the project are compiled in three chapters:

The first chapter introduces a new hydrothermal synthesis method making use of abundant metal oxide reactants and hydrocarbon synthesis additives. The effects of changing metal stoichiometry and post-synthetic treatments on the activity and stability of the obtained materials will be discussed.

The second chapter investigates the chemical processes occurring during crystallization of M1 phase under hydrothermal conditions using the new method. The effects of crystallization temperature on the material properties and on the catalytic activity will be addressed.

The third chapter deals with the influence of metal oxide composition on the product distribution, activity and selectivity in oxidative dehydrogenation of ethane. Detailed kinetic tests of ethane and ethene oxidation are combined with bulk and surface physico-chemical analyses of $MoV(TeNb)O_x$ to correlate elemental composition to selective and unselective reaction pathways.

2 A new synthesis method for M1 phase of MoV(Te,Nb) mixed metal oxides

In this chapter, a novel hydrothermal synthesis method for MoV(Te,Nb) mixed metal oxides is presented. It makes use of abundant metal oxide reactants and oxo-functionalized hydrocarbon synthesis additives.

Screening through a set of synthesis conditions (temperature, duration, additive concentration, crystallization temperature) showed that M1 phase can be obtained in a relatively broad range of conditions, if a thermal treatment is performed on the hydrothermally prepared solid. Under certain synthesis conditions, M1 phase was found to directly crystallize under hydrothermal conditions.

Increasing the concentration of V (with respect to Mo) in the mixed oxide results in higher ethane ODH rates due to larger number of active sites present on the catalyst surface. At fixed V content, activity was observed to benefit from small amounts of Te, while Nb does not affect conversion rates.

2.1   Motivation

Conventional synthesis methods for M1-type mixed metal oxide catalysts typically make use of metal salt reactants. [70,105,107,179]. Either hydrothermal, evaporation or spray drying methods result in unordered mixed metal oxides. [94,180] This intermediate needs then to be annealed in inert atmosphere at temperatures above 500 °C to crystallize and to become active in selective (amm)oxidation reactions [96]. Typically, phase mixtures of single metal oxides to quaternary (mixed) metal oxide phases (including M1 and M2 phases) are formed during this process. Formation of catalytically inactive phases thereby lowers the activity per gram of the catalyst. Also, transition metal salt reactants are relatively scarce and expensive compared to their respective oxide counterparts. Thus, to make industrial scale application of M1-MoV(Te,Nb)O$_x$ feasible, synthesis from more abundant metal sources is desirable.

To overcome the disadvantages of hydrothermal syntheses of MoV(Te;Nb)O$_x$ reported in literature, we designed a synthesis protocol aiming for a better control over metal ion activity during hydrothermal synthesis. Hence, the abundant, but poorly soluble, metal oxides molybdenum(VI) oxide MoO$_3$, vanadium(V) oxide V$_2$O$_5$, tellurium(IV) oxide TeO$_2$

and niobium(V) oxide hydrate $Nb_2O_5 \cdot 1.5H_2O$ were chosen as metal precursors. Solvation of metal ions is enhanced by organic chelating agents (citric acid, oxalic acid and monoethylene glycol, Figure 9). This procedure is partially based on the syntheses reported by Mestl et al. [181-183], in which MoO_3 and V_2O_5 were used, and extended to complete replacement of soluble metal precursors and stoichiometries optimized for oxidative dehydrogenation of ethane.
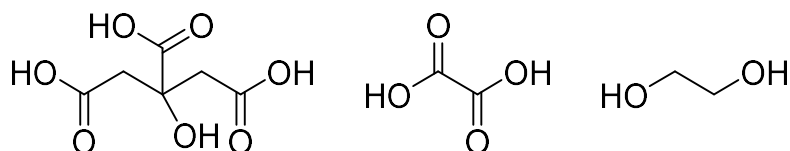

Figure 9: Structural formulae of citric acid (left), oxalic acid (middle) and monoethylene glycol (right).

2.2   Synthesis and thermal treatment

Prior research on replacing scarce and expensive metal salt reactants with more abundant and cheaper metal oxide reactants for $MoVTeNbO_x$ synthesis resulted in the use of MoO_3 and V_2O_5 as sources of Mo and V, respectively [182,183]. However, similar to most other previously reported methods, telluric acid $Te(OH)_6$ and ammonium niobiate oxalate hydrate $(NH)_4NbO(C_2O_4)_2 \cdot xH_2O$ were used as sources of Te and Nb in this syntheses. Hydrocarbon additives such as alcohols, ethers or carboxylic acids, preferably citric acid, oxalic acid and monoethylene glycol, had to be used for synthesis of phase pure M1-MoVTeNb and full crystallinity was achieved by heat treatment in inert atmosphere [182,183]. Results of combinatorial screening experiments by Mestl *et al.* showed that catalyst metal stoichiometry can be varied in a broad range and thus be adjusted to its desired application [181]. Previously, also the use of TeO_2 in hydrothermal synthesis of M1 phase $MoVTeO_x$ and $MoVTeNbO_x$ -using otherwise a standard hydrothermal synthesis protocol including soluble metal reactants and subsequent heat treatment - was reported [87], demonstrating the potential to also replace $Te(OH)_6$ by TeO_2 in a new synthesis approach.

In a first attempt to screen for possible synthesis conditions of M1-$MoVTeNbO_x$ from metal oxide reactants, MoO_3, V_2O_5, TeO_2 and $Nb_2O_5 \cdot 1.5H_2O$ were mixed with the organic synthesis additives and ultra-pure water in a "one-pot-synthesis" approach. The nominal metal stoichiometry was fixed at Mo:V:Te:Nb = 1:0.22:0.18:0.18 and a Mo concentration of 0.5 mol L^{-1} was used. This stoichiometry was chosen for comparison with the synthesis

published in reference [111]. The amounts of citric acid (CA) and monoethylene glycol (EG) with respect to Mo were adjusted to Mo:CA:EG = 1:0.075:0.075 based on the amounts given in the patent literature [182,183]. In order to tune the redox-potential and concentration of chelating agents in the mixture, the amount of oxalic acid (OA) relative to Nb was varied in the range of OA:Nb = 1 – 3. The hydrothermal synthesis temperature was investigated in the range of 175 – 200 °C and synthesis duration from 24 h to 72 h. This screening experiment resulted in 21 mixed metal oxide samples.

The general synthesis procedure was as follows: the aqueous suspension of the metal oxides and synthesis additives in their respective amounts was transferred to a Teflon lined steel autoclave, placed in a rotary furnace and subjected to the desired hydrothermal conditions. Filtration and washing of the crude precipitates gave a blue solid and dark blue filtrate. Final crystallization was performed by a two-step heat treatment in flow of synthetic air at 200 °C and nitrogen at 650 °C. For further details on the experimental procedure the reader is referred to Chapter 7.

XRD analysis of the dried precipitate showed only few and broad reflexes, indicating only short-range ordering in the precipitate. Specially, no indication of fully crystalline, long-range ordered M1 or other MoVTeNb (mixed) oxide crystalline phases (see also Figure 12) was found. MoVTeNbO$_x$-M1 phase was formed in all cases next to varying amounts of other crystalline by-product phases upon the thermal treatment. The by-products were typically M2-MoVTeNbO$_x$ phase or Mo$_5$O$_{14}$-type phases. Figure 10 shows the M1 phase content with respect to the amount of crystalline material found in all samples.

It was found that for all synthesis conditions (except for combination of lowest temperature 175°C together with low OA:Nb ratio of 1 or at short synthesis durations of 24 h), relative M1 phase content was above 70 wt.-%. No clear trends regarding the influence of synthesis parameters on the M1 phase content were identified beyond this analysis. Nevertheless, it was demonstrated that formation of M1 phase from metal oxide reactants is possible with the new synthesis approach.
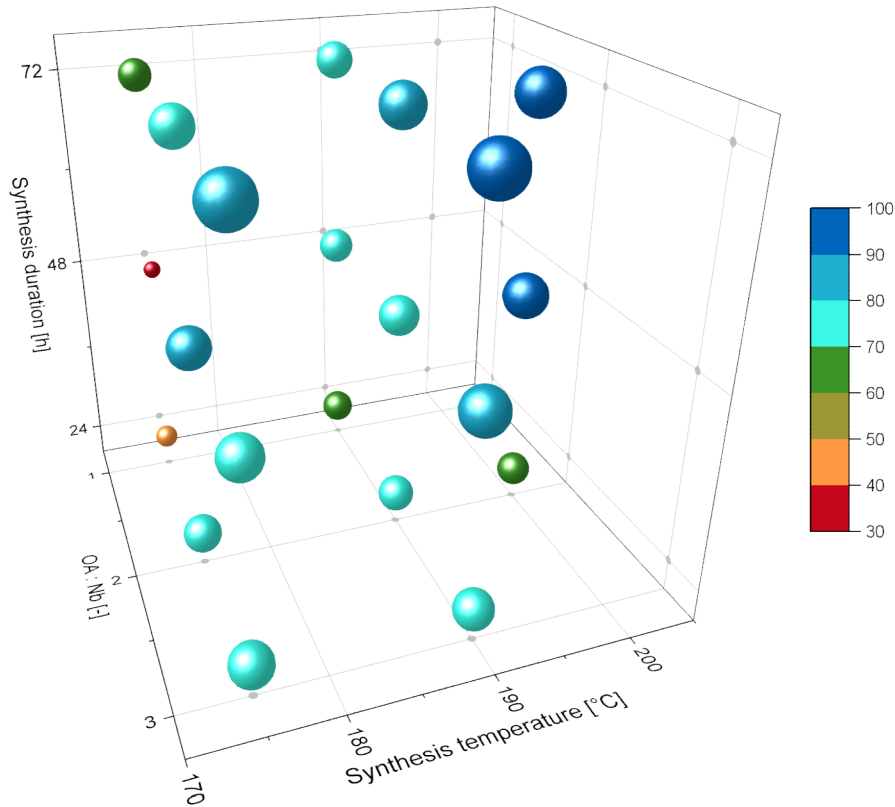
Figure 10: Impact of synthesis temperature, synthesis duration and oxalic acid/Nb ratio on M1 phase purity of $MoV_{0.22}Te_{0.18}Nb_{0.18}O_x$ samples activated at 650 °C. Size of symbols and color code reflect content of M1 phase relative to crystalline content.

Crystalline MoVTeNb-M1 phase is a thermodynamically meta-stable product prone to phase transformations under high temperature [184,185]. M1 phase is crystallized from a largely unordered precursor oxide upon thermal treatment. During this thermal treatment the mixed oxide is undergoing auto-redox processes [96]. These auto-redox processes can yield additional mixed metal oxide phases, thereby adding another variable to the resulting phase distribution. In order to investigate the effect of the final temperature of the thermal treatment step on the mixed oxides' phase composition, nine precursor oxides from the screening experiments were heat treated in flow of synthetic air at 200 °C and nitrogen at 600 °C. The phase composition was compared to the same materials but treated at a final temperature of 650 °C. Figure 11 shows the comparison of phase distribution between the two sets of samples. It can be noted that in general M1 phase formation is preferred and the number of by-products is reduced at the higher activation temperature.

Combining the findings of synthesis screening and effects of activation temperature variation, it could be shown that high M1 phase purity can be obtained over a broad range of conditions. This demonstrates the feasibility and stability of the here developed synthesis protocol. As a minimum requirement for M1 phase content exceeding 70 wt.-% with respect to all crystalline material, temperature should be at least 190 °C, with a minimum OA:Nb ratio of 1 and synthesis duration not shorter than 48 h.
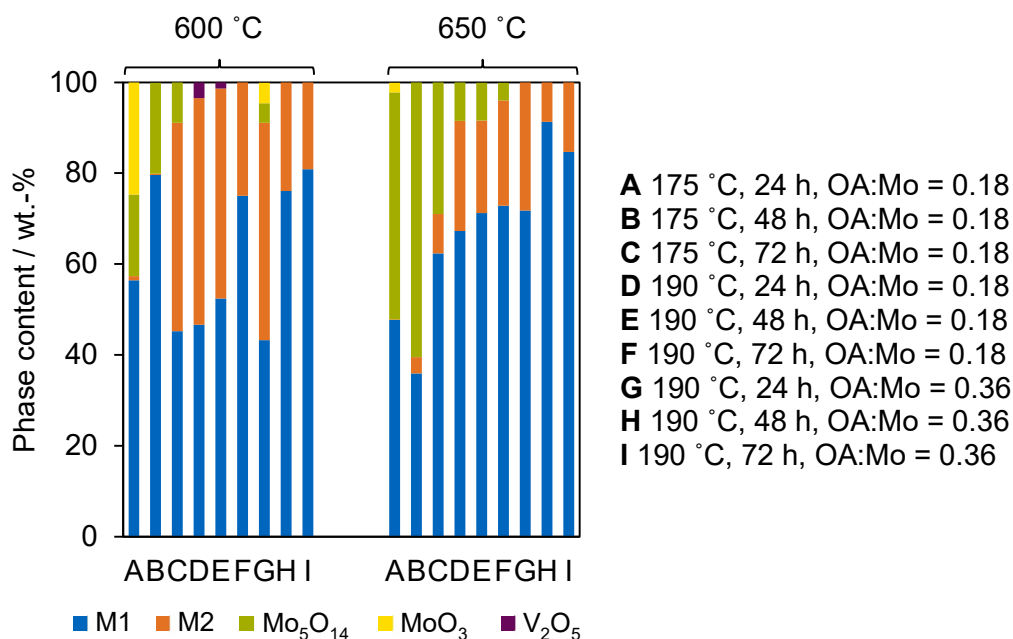
Figure 11: Impact of activation temperature (600 °C, left and 650 °C, right) on crystalline phase distribution in various $MoV_{0.22}Te_{0.18}Nb_{0.18}O_x$ samples after thermal treatment.

After having established a stable synthesis method yielding MoVTeNb mixed metal oxides with high M1 phase content, next, the effects of metal stoichiometry on phase composition, catalytic activity and catalytic stability were investigated.

2.3 Effect of metal stoichiometry variation on phase composition and catalytic activity

The concentration of surface vanadyl sites was previously reported to affect ODH-E activity of MoVTeNbOx catalysts [75,135,141,142]. It is therefore expected that increasing the amount of V incorporated in the M1 structure enhances its catalytic activity. To test this

hypothesis, a series of samples with constant Te and Nb content (Te/Mo = Nb/Mo = 0.18) and different V/Mo (0.22 – 0.30) ratios was prepared using the established method (190°C, 48 h, Mo:EG:CA:OA = 1:0.075:0.075:0.18) described in the previous section. The starting nominal composition was chosen to allow a direct comparison with the M1 synthesis published elsewhere [111]. Similarly to the syntheses described in section 2.2, it was found that, for the whole range of V/Mo ratios tested, only some short-range ordering of the mixed metal oxide took place under hydrothermal conditions. The XRD diffractograms show again some broad reflections characteristic of only short range ordered M1 phase (see Figure 12). Such nanocrystallinity and presence of unordered domains in M1 crystals have frequently been reported in literature. [186-189] Here, contributions from such non well-defined crystal structures in XRD analysis are summarized under the term "amorphous" without further distinguishing their exact nature.
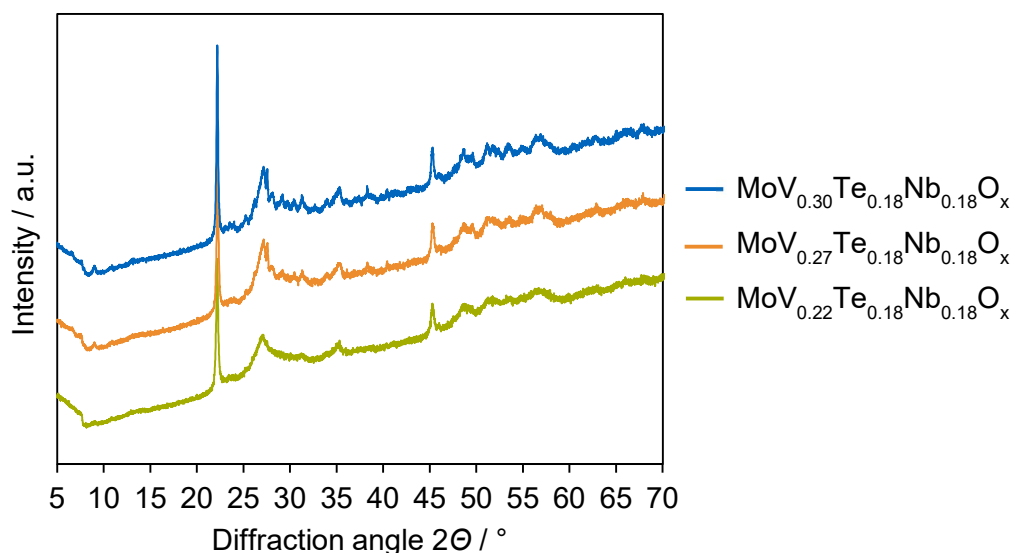
Figure 12: Diffractograms of as-synthesized $MoV_{0.22-0.30}Te_{0.18}Nb_{0.18}O_x$. Diffractograms were stacked for purpose of better comparison.

The ordering in the mixed oxides increases with higher V content in the samples. However, a two-step thermal post-treatment of the precipitated solids in flow of air at 200 °C and nitrogen flow at 650 °C is necessary to fully crystallize the M1 phase (Figure 13). We used the presence and intensity of reflections at $2\Theta = 6.6°$, $7.8°$ and $9.0°$ corresponding to {020}, {120} and {210} M1 crystal planes to distinguish between short-

and long-range ordering in the samples. The characterization results of the thermally treated samples are shown in Table 1.
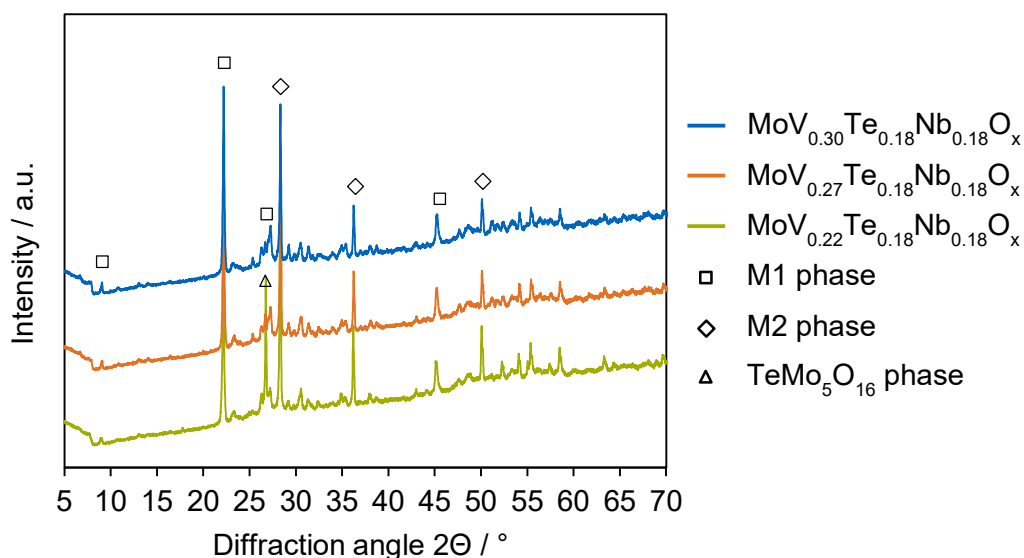
Figure 13: Diffractograms of $MoV_{0.22-0.30}Te_{0.18}Nb_{0.18}O_x$ catalysts after 650 °C thermal post-treatment.

Table 1: Physico-chemical properties of $MoV_{0.22-0.30}Te_{0.18}Nb_{0.18}O_x$ catalysts after 650 °C heat treatment.

ICP-OES (in brackets: nominal) formula	BET / $m^2 g^{-1}$	M1 content / wt.-%	Amorphous content / wt.-%	Other phases
$MoV_{0.21}Te_{0.08}Nb_{0.17}O_x$ ($MoV_{0.22}Te_{0.18}Nb_{0.18}O_x$)	11	61	0	M2
$MoV_{0.25}Te_{0.07}Nb_{0.16}O_x$ ($MoV_{0.27}Te_{0.18}Nb_{0.18}O_x$)	22	64	0	M2
$MoV_{0.29}Te_{0.11}Nb_{0.18}O_x$ ($MoV_{0.30}Te_{0.18}Nb_{0.18}O_x$)	30	58	9	$TeMo_5O_{16}$, M2

The M1 samples shown in Table 1 were tested for their catalytic performance in the oxidative dehydrogenation of ethane and results are shown as Arrhenius type plots in Figure 14. Standard deviation between repeated measurements of ethene formation rates at a given temperature was below 3% in all experiments performed for this thesis. Corresponding error bars are smaller than the symbols shown in the logarithmic

Arrhenius type plots and hence omitted. The parallel lines in the Arrhenius type plot indicate virtually identical energy of activation ($E_A \approx 85 \pm 2$ kJ mol^{-1}). Thus, differences in activity normalized per gram of M1 phase among the different samples are only due to the pre-exponential factor. This can be attributed to differences in the concentration of the same type of active sites. Furthermore, it can be seen from Figure 14 that for a constant Te and Nb content, the activity increases with increasing V/Mo ratio. This is not unexpected, given that the catalytic activity of M1 is associated to surface V^{5+}=O species [75,135,141,142], and confirms our initial hypothesis.
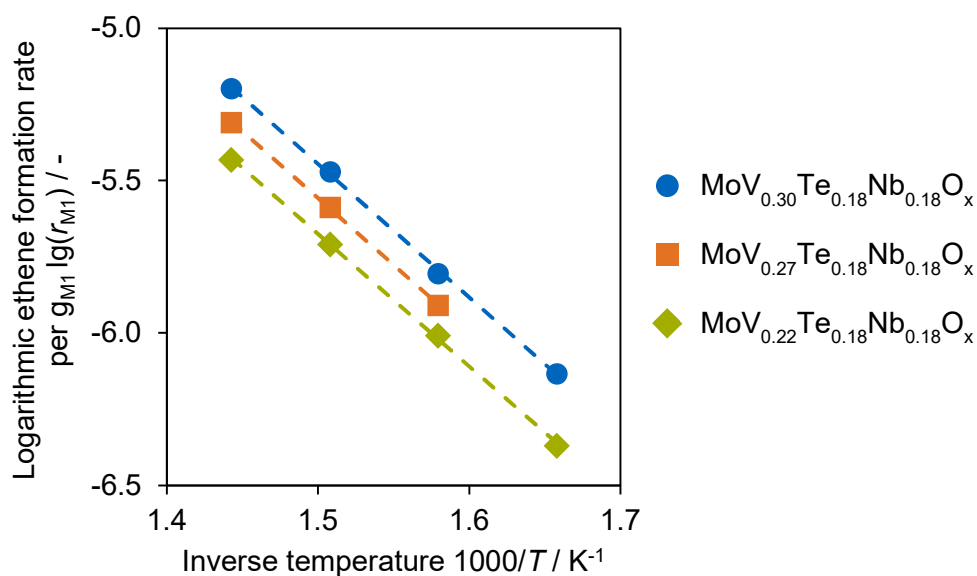
Figure 14: Arrhenius type plot of samples containing different amounts of vanadium and fixed Te/Mo = Nb/Mo = 0.18 after thermal treatment at 650 °C. Activity normalized to M1 phase content. T = 330 – 420 °C, p = 1 bar(a), WHSV = 17.6 h^{-1}.

Next, to further investigate the role of Te and Nb stoichiometry on the new synthesis of the MoVTeNbO$_x$ and its catalytic activity, another series of catalysts was prepared. A fixed V/Mo ratio of 0.30 was kept and the amount of Te and Nb was varied. In the composition range tested, samples synthesized with a nominal V/Mo ratio of 0.30 and Te/Mo and Nb/Mo ratio equal or lower than 0.10 directly precipitate as crystalline M1 phase under hydrothermal conditions at 190 °C (see Table 2 and Figure 15). Other crystalline byproducts were only obtained in minor amounts by this method. A direct precipitation of crystalline MoVTeNb-M1 phase during hydrothermal synthesis has not been reported before. It also needs to be noted that using a lower V/Mo ratio of 0.22 together with low Nb/Mo and Te/Mo ratios (Nb,Te/Mo = 0.05) did only lead to formation

of an oxide without long-range order during hydrothermal synthesis (see Table 2 and Figure 15). Similar to the XRD patterns of precipitates shown in Figure 12, the pattern of $MoV_{0.22}Te_{0.05}Nb_{0.05}O_x$ only weakly resembles the M1 structure. However, this short-range ordered material can be crystallized as M1 phase by applying thermal treatment in inert atmosphere at 650°C (Figure 16).
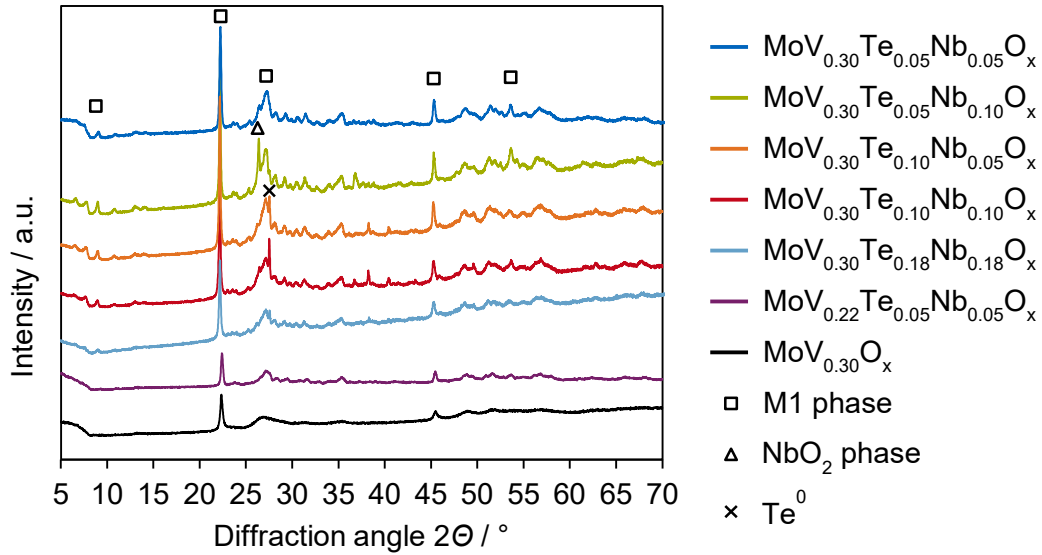

Figure 15: Diffractograms of various as-prepared $MoVTeNbO_x$ formulations synthesized via the new method. Labels indicate main constituent crystalline phases.
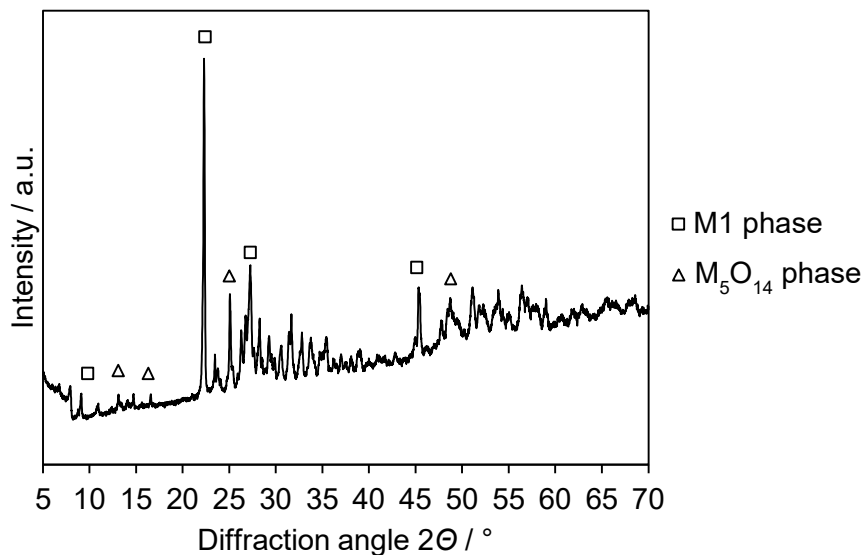
Figure 16: Diffractogram of $MoV_{0.22}Te_{0.05}Nb_{0.05}O_x$ after thermal treatment at 650°C. Labels indicate main constituent crystalline phases.

Table 2: Physico-chemical properties of as-prepared MoVTeNbOx, synthesized via the new method.

ICP-OES (in brackets: nominal) formula	BET / m² g⁻¹	Internal area / m² g⁻¹	Pore volume / cm³ g⁻¹	M1 / wt.-%	Amorphous / wt.-%	Other phases
$MoV_{0.30}O_x$ ($MoV_{0.30}O_x$)	97	53	0.16	n.d. [a]	n.d. [a]	n.d. [a]
$MoV_{0.30}Te_{0.05}Nb_{0.05}O_x$ ($MoV_{0.30}Te_{0.05}Nb_{0.05}O_x$)	59	30	0.11	77	22	none
$MoV_{0.31}Te_{0.05}Nb_{0.10}O_x$ ($MoV_{0.30}Te_{0.05}Nb_{0.10}O_x$)	71	93	0.16	58	40	NbO_2
$MoV_{0.30}Te_{0.10}Nb_{0.09}O_x$ ($MoV_{0.30}Te_{0.10}Nb_{0.10}O_x$)	87	49	0.19	59	40	Te^0
$MoV_{0.31}Te_{0.12}Nb_{0.08}O_x$ ($MoV_{0.30}Te_{0.10}Nb_{0.05}O_x$)	74	9	0.03	52	47	Te^0
$MoV_{0.29}Te_{0.14}Nb_{0.17}O_x$ ($MoV_{0.30}Te_{0.18}Nb_{0.18}O_x$)	111	77	0.27	n.d. [a]	n.d. [a]	n.d. [a]
$MoV_{0.22}Te_{0.01}Nb_{0.03}O_x$ ($MoV_{0.22}Te_{0.05}Nb_{0.05}O_x$)	48	33	0.09	n.d. [a]	n.d. [a]	n.d. [a]

a) Diffractograms (Figure 15) resemble poorly crystallized M1. Rietveld refinement of the diffractogram was hence not possible due to missing long range order in the sample.

Regarding to the role of Nb and Te in the activity of $MoVTeNbO_x$ samples with optimized V/Mo of 0.30, comparison of activity is done based on ODH rates normalized per gram of M1 crystalline phase. It can be seen in Figure 17 that the Nb content within this range (Nb/Mo of 0.05 to 0.10) does not affect ODH rates. Conversely, Te/Mo ratios have an impact on catalytic activity of $M1$-$MoVTeNbO_x$ and better performance is observed for samples containing only small amounts of Te (Te/Mo = 0.05). This better performance might be linked to additional radical oxygen sites formed by the partial reduction of TeO_x units and subsequent release of Te^0 from the M1 framework under ODH-E reaction conditions [190].

Figure 17: Arrhenius type plot of $MoVTeNbO_x$ with different metal composition regarding Nb and Te content and fixed V/Mo = 0.30. Activity was normalized to M1 phase content of the samples (M1 phase content of $MoV_{0.30}Ox$ sample was assumed to be 100 wt.-%). T = 330 – 420 °C, p = 1 bar(a), WHSV = 14.3 h^{-1}.

A similar trend in activity regarding Te and Nb content is also observed if rates are normalized per mass of catalyst (Figure 18). Again, based on the observed parallel trends in the Arrhenius type plots, these differences in activity are attributable to differences in the number of active sites and not in their chemical nature.
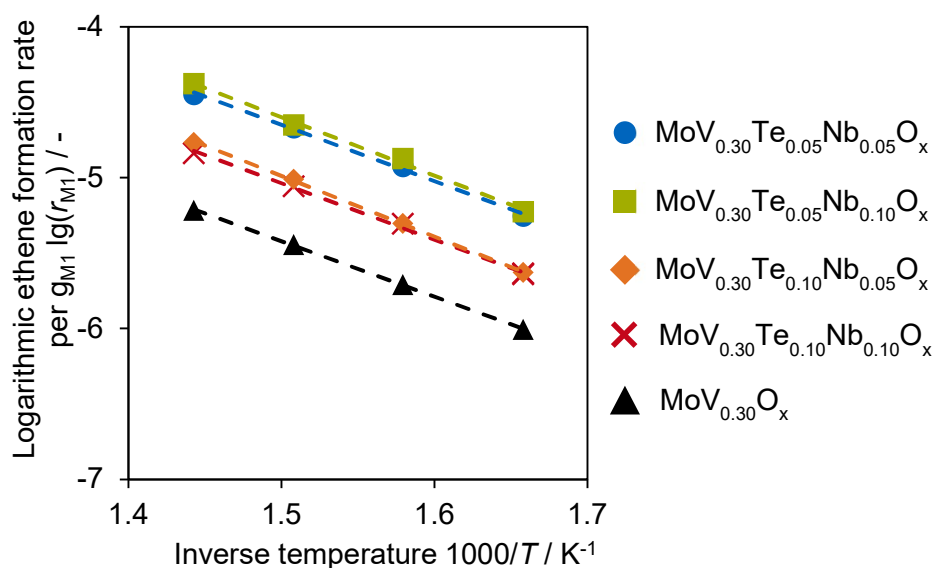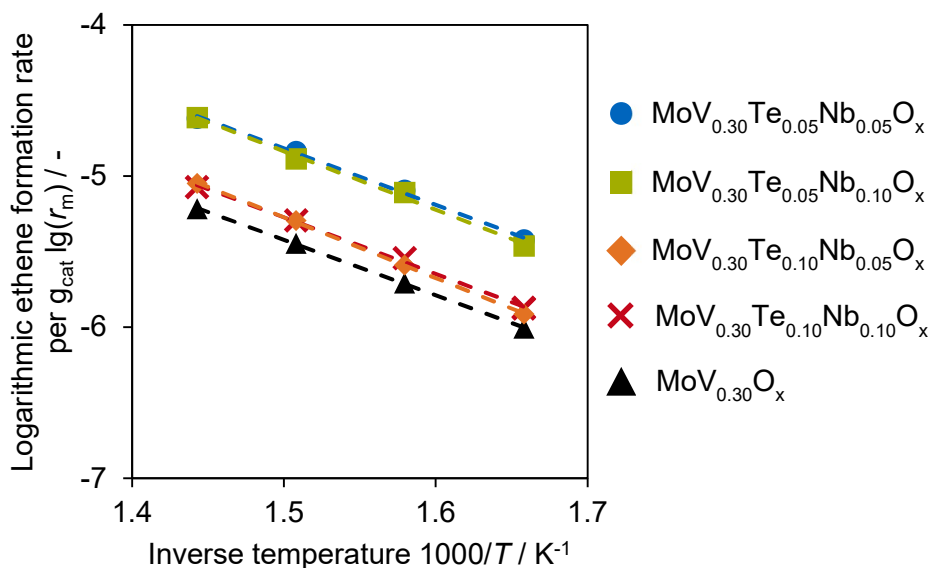
Figure 18: Arrhenius type plot of MoVTeNbO$_x$ with different metal composition regarding Nb and Te content and fixed V/Mo = 0.30. Activity was normalized to the mass of the samples. T = 330 – 420 °C, p = 1 bar(a), WHSV = 14.3 h^{-1}.

Given the relevant amount of crystalline M1 found in the as-prepared solids obtained by our new method (Table 2), we performed catalytic tests of samples of various elemental compositions without any high temperature thermal pretreatment of the solid. The material was solely preconditioned to the reaction temperature by a treatment in flowing nitrogen at 400 °C for 2 h. As a reference, we also tested one sample from Table 1 after treatment at 650 °C. A comparison of the activity per gram of catalyst (Figure 19) shows that, even though ca. 50 % of the solid is still amorphous in the series of catalysts shown in Table 2, the activity per gram is significantly higher than for catalysts prepared with the stoichiometries shown in Table 1.
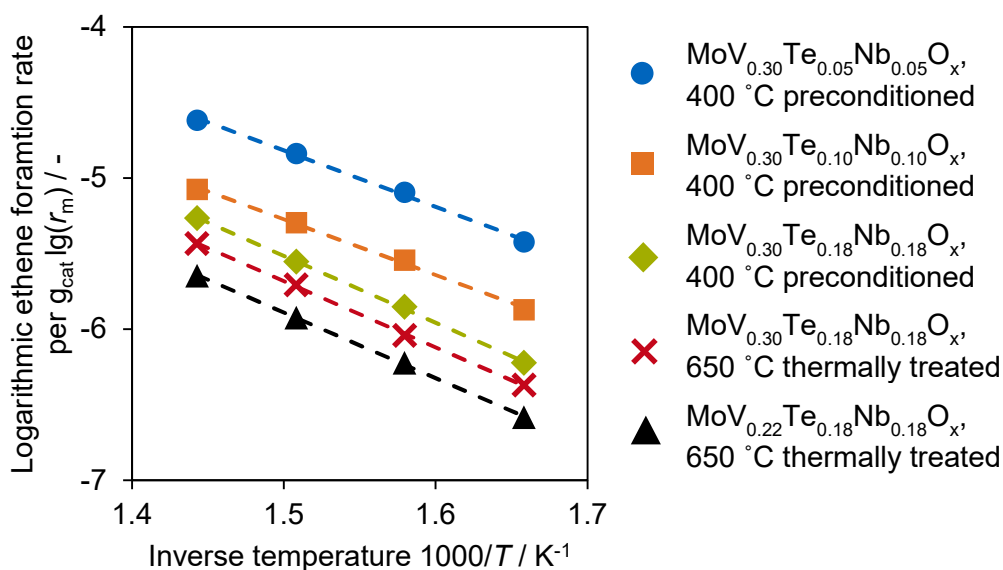
Figure 19: Arrhenius type plot of different MoVTeNbO$_x$ samples. Activity was normalized to catalyst mass. T = 330 – 420 °C, p = 1 bar(a), WHSV = 14.3 - 17.6 h^{-1}.

2.4   Effect of metal stoichiometry variation on catalytic stability

The effect of the elemental composition of the catalysts and their thermal treatment (pure preconditioning or high temperature crystallization) will be assessed in this section. For this purpose, ethane ODH reaction was carried out at constant temperature and gas flow using the catalysts shown in Figure 19 and MoV$_{0.30}$O$_x$. Somewhat harsher conditions compared to Arrhenius type experiments were applied using a temperature of 400 °C and total pressure of 4 bar(a) (ethane and oxygen partial pressure being 360 mbar(a), each). Ethane weight hourly space velocity was adjusted for all catalysts to reach similar initial hydrocarbon conversions in the range of 25 – 35 %. Figure 20 shows the ethene formation rate plotted as function of time on stream (TOS).

Figure 20: Ethene formation rate as function of time on stream for catalysts with various stoichiometry and thermal treatment. Activity was normalized to catalyst mass. Dashed box in A highlights plotted space in B. T = 400 °C, p = 4 bar(a), WHSV = 1.3 – 22.3 h^{-1}.

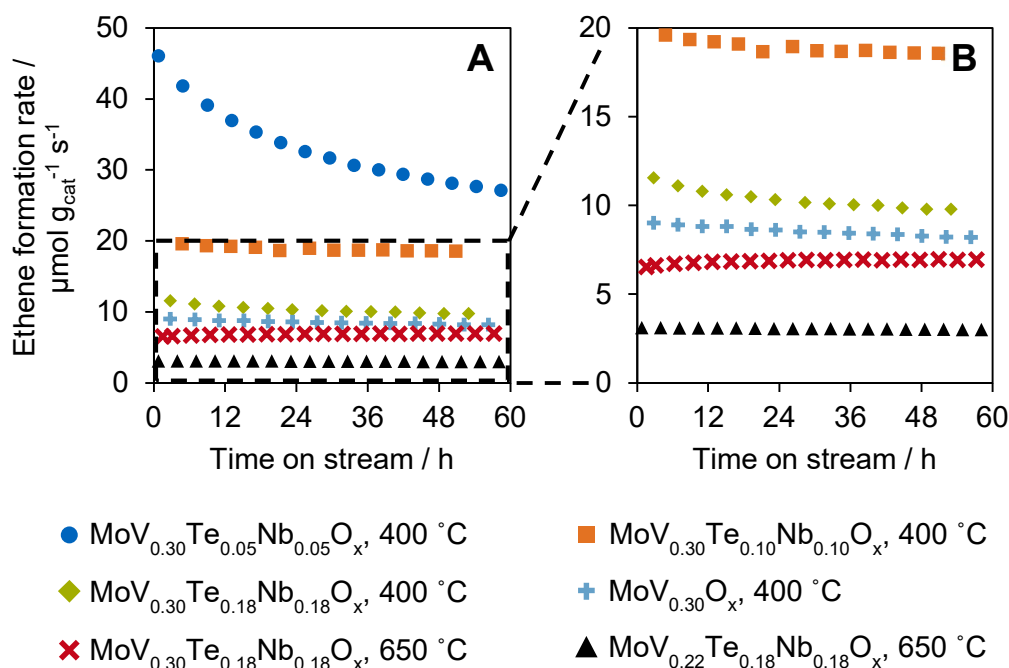It becomes apparent that samples containing a relatively large fraction of Te and Nb (Te/Mo = Nb/Mo = 0.18) and having been exposed to 650 °C show stable ($MoV_{0.22}Te_{O.18}Nb_{0.18}O_x$, black triangles) or even slightly increasing ($MoV_{0.30}Te_{O.18}Nb_{0.18}O_x$, red crosses) activity over TOS irrespective of their V content. It needs to be noted that the catalyst activation temperature of 650 °C by far exceeds the reaction temperature (400 °C). We attribute this behavior to stabilization of active sites by Nb, as suggested by Grasselli [136]. Also, (over)compensation of initial deactivation by formation of additional oxygen radical sites, induced by reduction of a certain fraction of TeO entities, may play a role in the TOS behavior [190]. This holds especially true for the observed *in-situ* activation of $MoV_{0.30}Te_{0.18}Nb_{0.18}O_x$. Replacing the two-step thermal treatment up to 650 °C of $MoV_{0.30}Te_{0.18}Nb_{0.18}O_x$ by a pure pre-conditioning to reaction temperature in flowing nitrogen at 400 °C (green triangles) results in an increase in initial activity (see also Figure 19). However, this increment in activity is accompanied by some initial deactivation. Stable activity is obtained after approximately one day of time on stream and is still higher compared to the material treated at 650 °C. Similar deactivation trends are observed for other tested catalysts containing low fractions of Te and Nb (Te/Mo, Nb/Mo ≤ 0.10). This deactivation is likely caused by slow accommodation and

surface restructuring effects under reaction conditions, i.e. the surface of the mixed metal oxides adapting its thermodynamically most stable configuration. Such reconfiguration of crystal termination facets was qualitatively assessed in $MoV_{0.30}Te_{0.05}Nb_{0.05}O_x$ using electron microscopy (SEM and ADF-STEM). Figure 21A and B shows typical lateral terminations in as-prepared state and after 40 h of time-on-stream under typical ODH reaction conditions (T = 420 °C, C_2H_6:O_2:He = 9:9:82, p = 1 bar(a)). In the as-prepared state the particles exhibit markedly corrugated surfaces, i.e. a large fraction of high index-planes with high surface energy. After prolonged exposure to reaction conditions surfaces appear to smoothen, and thereby reducing the fraction of high-index planes and hence their free surface energy. At the same time the overall morphology of the needle-like M1 particles remains unaffected (Figure 21C and D). Effects of crystallization temperature on the surface of M1 crystals and their intrinsic activity will be discussed in greater detail in Chapter 3. The most visible deactivation is occurring over the otherwise most active catalyst $MoV_{0.30}Te_{0.05}Nb_{0.05}O_x$, which loses about a third of its initial activity within the first 48 h of time on stream. Yet, extrapolating its activity loss to longer durations, assuming simple exponential decay, shows stabilization of the ethene formation rate after ca. 100 h. Its productivity at this point of TOS is projected to still be 50 % higher than the second most active catalyst $MoV_{0.30}Te_{0.10}Nb_{0.10}O_x$. Therefore, the productivity expressed as integral space time yield over time on stream is highest for all catalysts tested over $MoV_{0.30}Te_{0.05}Nb_{0.05}O_x$, despite its strong initial deactivation.
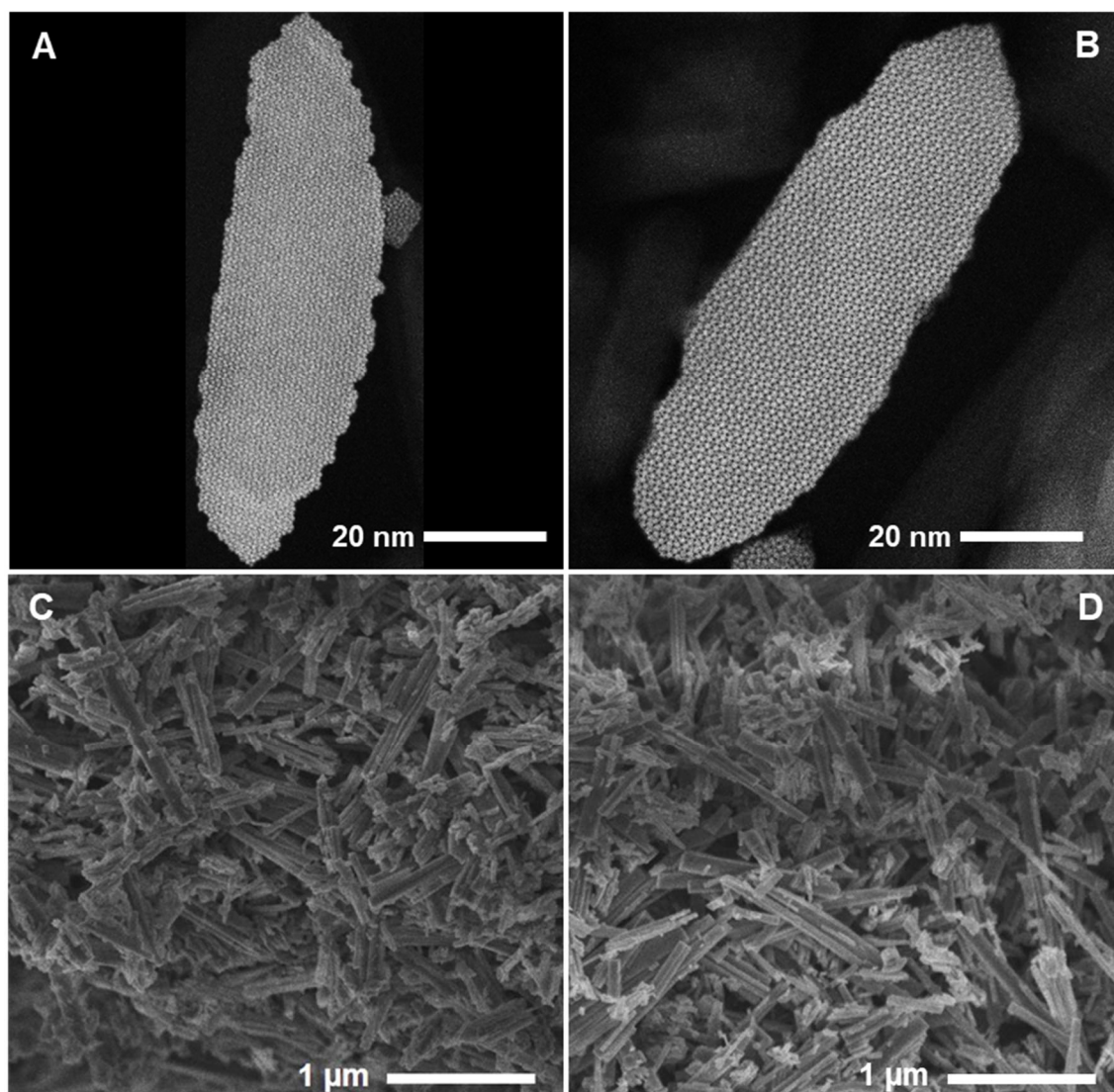
Figure 21: ADF-STEM (top row) images of {001} plane and SEM images (bottom row) of M1-MoV$_{0.30}$Te$_{0.05}$Nb$_{0.05}$O$_x$ synthesized by the new method in as prepared state (A,C) and after 40 h of time on stream in ODH-E reaction at 420 °C (B,D).

2.5 Conclusions

A new hydrothermal synthesis method for M1-MoV(Te,Nb) mixed metal oxides starting from abundant metal oxide reactants was developed. It was shown that by tuning the redox potential by addition of organic synthesis additives M1 crystal phase can be obtained over a broad range of temperatures and synthesis durations with variable stoichiometries. This new method allows to directly precipitate crystalline M1 phase under hydrothermal conditions with certain stoichiometries ($MoV_{0.30}Te_{0-0.10}Nb_{0-0.10}O_x$) and hence at temperatures more than 400 °C lower than in conventional syntheses. Metal stoichiometry was also found to strongly affect catalytic activity in ODH-E. Ethene formation rates increase with V content, attributed to increased availability of hydrogen abstracting surface vanadyl sites. Dehydrogenation activity can further be increased by addition of small amounts of Te, while catalytic stability appears to benefit from addition Nb. Highest space time yields were obtained over catalysts crystallized under hydrothermal conditions and solely having been preconditioned to reaction temperature. However, accommodation of the catalysts to ODH-E reaction conditions leads to slight initial deactivation of such catalysts.

2.6 Associated content and contributions

Part of the content of this chapter is based on the publication *Design and synthesis of highly active MoVTeNb-oxides for ethane oxidative dehydrogenation* published in Nature Communications (reference [81]). The structure and content of this chapter differs from the publication. The synthesis protocol was patented (see Chapter 13 of this work and references [191-193]).

Daniel Melzer performed the synthesis, XRD analysis and kinetic tests of the mixed metal oxide catalysts and wrote the manuscript. Dr. Gerhard Mestl and Dr. Klaus Wanninger advised the research and contributed to writing of the publication. Dr. Maricruz Sanchez-Sanchez is the project leader and Prof. Dr. Johannes A. Lercher is the principal investigator of this project. They both supervised the research and discussed results and conclusions.

3 Synthesis of M1 crystals with highly active surfaces by low-temperature crystallization

Based on the new hydrothermal synthesis protocol presented in the previous chapter, the chemical processes in the direct precipitation of crystalline M1 phase under hydrothermal conditions at temperatures ca. 400 °C lower than in standard synthesis of M1 catalysts, are investigated. This chapter studies the speciation of crystalline M1 phase and solvated polyoxometalate cluster intermediates for both novel and standard synthesis approaches using XRD, UV-vis and STEM. The findings of the physico-chemical characterization correlate to the catalytic activity in oxidative dehydrogenation of ethane.

Comparison of catalytic activities normalized per M1 phase and surface area revealed that catalysts prepared by the low temperature synthesis method have a higher intrinsic activity in ethane oxidative dehydrogenation compared to standard M1 phase catalysts. This higher activity is in part due to a higher surface area of the produced mixed oxide and in part to the corrugated lateral termination of M1 crystals, which leads to a high surface concentration of catalytically active sites. The formation of partially crystalline M1 under hydrothermal conditions by the new synthesis method is attributed to a controlled precipitation of polyoxometalate building blocks.

A new hydrothermal synthesis method for MoVTeNb mixed metal oxides was introduced in the previous chapter. It was found that using a certain stoichiometry of poorly soluble metal oxides as reactants together with organic synthesis additives allows for direct precipitation of the crystalline M1 phase under hydrothermal conditions. Materials with a $MoV_{0.30}Te_{0.05}Nb_{0.05}O_x$ metal stoichiometry have shown the highest activity in conversion of ethane to ethene. The speciation of this highly active mixed metal oxide will be studied in the following chapter. The crystallization process will be compared to a mixed metal oxide of similar stoichiometry but synthesized according to the conventional hydrothermal synthesis protocol requiring high temperature for crystallization [1]. The differences between both methods will be pointed out and their consequences for catalytic activity discussed.

3.1 Effect of crystallization temperature on crystal phase distribution and crystal termination

Table 3 shows a summary of the physico-chemical characterization of the as prepared $MoV_{0.30}Te_{0.05}Nb_{0.05}O_x$ mixed metal oxide and the same material after being preconditioned to the reaction temperatures for ethane ODH (400 °C). For the sake of comparison, the properties of another M1 catalyst with similar metal stoichiometry but prepared by a standard hydrothermal synthesis similar to the one described in reference [1] are also shown in Table 3.

Preconditioning of the $MoVTeNbO_x$ sample prepared by the new method to typical reaction temperatures of 400 °C in N_2 flow resulted in a small loss of BET surface area and pore volume (Table 3), and a slight increase in overall crystallinity and M1 phase content. The specific surface area of the preconditioned mixed metal oxide is 50 m^2 g^{-1}, which is a remarkably high value for a metal oxide bulk catalyst and, as far as we know, considerably larger than any surface areas reported until date for M1 crystalline phase Mo-V based catalysts [87,98,134,194]. It is also four times larger than the specific surface area of the reference sample synthesized according to the standard method.

Table 3: Comparison of physico-chemical properties of a MoVTeNbO$_x$ material prepared according to the hydrothermal method described here ("New") with properties of MoVTeNbO$_x$ materials prepared by the standard hydrothermal synthesis method in reference [1] ("Standard").

ICP-OES (in brackets: nominal) formula	Synthesis method	Thermal treatment	BET / m² g⁻¹	Internal area / m² g⁻¹	Pore volume / cm³ g⁻¹	M1 phase content / wt.-%	Crystallinity / wt.-%
MoV$_{0.30}$Te$_{0.05}$Nb$_{0.05}$O$_x$ (MoV$_{0.30}$Te$_{0.05}$Nb$_{0.05}$O$_x$)	New	none	59	30	0.11	77	78
MoV$_{0.30}$Te$_{0.05}$Nb$_{0.05}$O$_x$ (MoV$_{0.30}$Te$_{0.05}$Nb$_{0.05}$O$_x$)	New	400 °C, N$_2$	50	25	0.09	79	82
MoV$_{0.31}$Te$_{0.20}$Nb$_{0.17}$O$_x$ (MoV$_{0.40}$Te$_{0.10}$Nb$_{0.10}$O$_x$)	Standard	none	61	93	0.12	n.d. [a]	n.d. [a]
MoV$_{0.30}$Te$_{0.06}$Nb$_{0.08}$O$_x$ (MoV$_{0.40}$Te$_{0.10}$Nb$_{0.10}$O$_x$)	Standard	650 °C, N$_2$	13	9	0.03	97	100

a) Diffractogram shows only a single broad reflection around $2\Theta = 21.4°$ matching the {001}-plane reflections of e.g. M1, M2 and M$_5$O$_{14}$ phases. Rietveld refinement of the diffractogram was not possible due to missing long range order in the sample.

In Figure 22, the catalytic activity of the M1 sample prepared by our new synthesis method is compared to a M1 catalyst prepared with similar metal stoichiometry but following the hydrothermal synthesis method reported in literature [1]. It can be seen that the new synthesis method yields a catalyst with mass-normalized activity almost one order of magnitude higher than the activity of the material crystallized at high temperature, despite having a lower content of M1 phase per gram (Table 3). Energy of activation for ethene formation was 75 kJ mol^{-1} for the low temperature crystallized catalyst and 88 kJ mol^{-1} for the catalyst prepared by the standard method. This difference of energies of activation, although larger than the error bar (± 2 kJ mol^{-1}), is assumed being not significant enough to be attributed to a change in the mechanism of ethene formation. Thus, for catalysts with a similar metal stoichiometry, it can be concluded that the M1 phase preparation route does not affect the main reaction pathways of ethane oxidation over this type of catalyst.
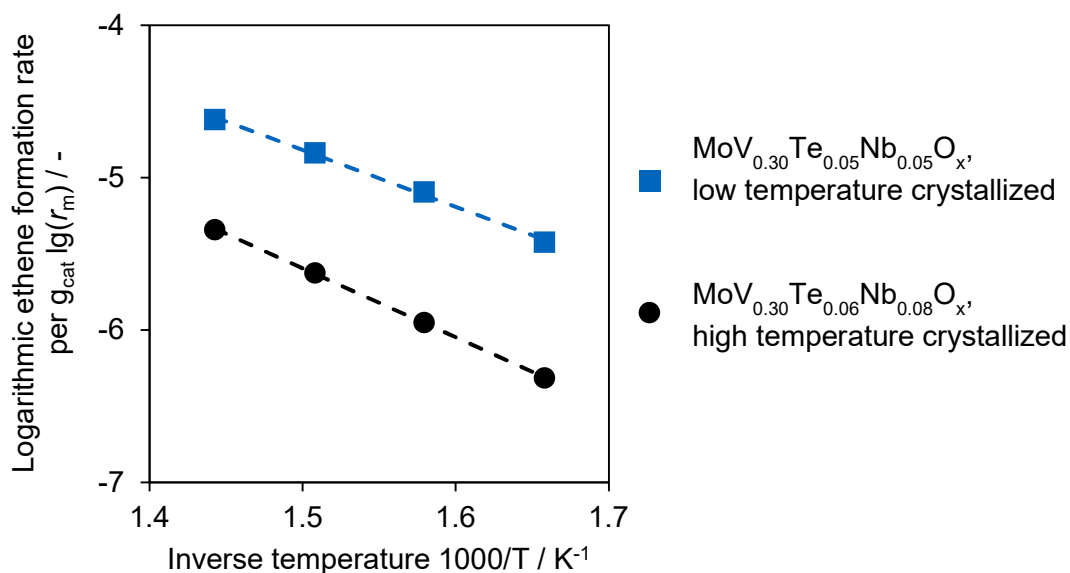

Figure 22: Arrhenius type plot of the ODH activity of catalyst $MoV_{0.30}Te_{0.05}Nb_{0.05}O_x$ crystallized at low temperature and catalyst $MoV_{0.30}Te_{0.06}Nb_{0.08}O_x$ crystallized at high temperature catalysts. Reaction conditions applied: T = 330 – 420 °C, p = 1 bar(a), WHSV = 6.8 h^{-1} (high temperature crystallized), 14.5 h^{-1} (low temperature crystallized).

Further comparison of the two MoVTeNbO$_x$ catalysts shown in Figure 22 is provided in Figure 23. Given that the only active phase in ethane oxidation is M1 [122], the ethene formation rates are normalized to the weight percentage of M1 phase (as calculated by Rietveld analysis) in each catalyst. It can be seen from the corresponding Arrhenius plot

(Figure 23A) that the M1 phase normalized activity of the catalyst crystallized at low temperature is also almost one order of magnitude higher than the activity of the catalyst crystallized at high temperature. Next, the activity is normalized per specific surface area as obtained from the BET method (Figure 23B). Also in this case a slightly higher activity for the low temperature crystallized catalyst is observed. Finally, as it can be seen in Figure 23C, normalization of activity to both M1 phase content and specific surface area shows that M1 phase prepared by the new method has a higher intrinsic activity than M1 phase prepared by the standard synthetic procedure. In other words, the low temperature crystallized sample must have a higher density of active sites on the surface of M1 particles.
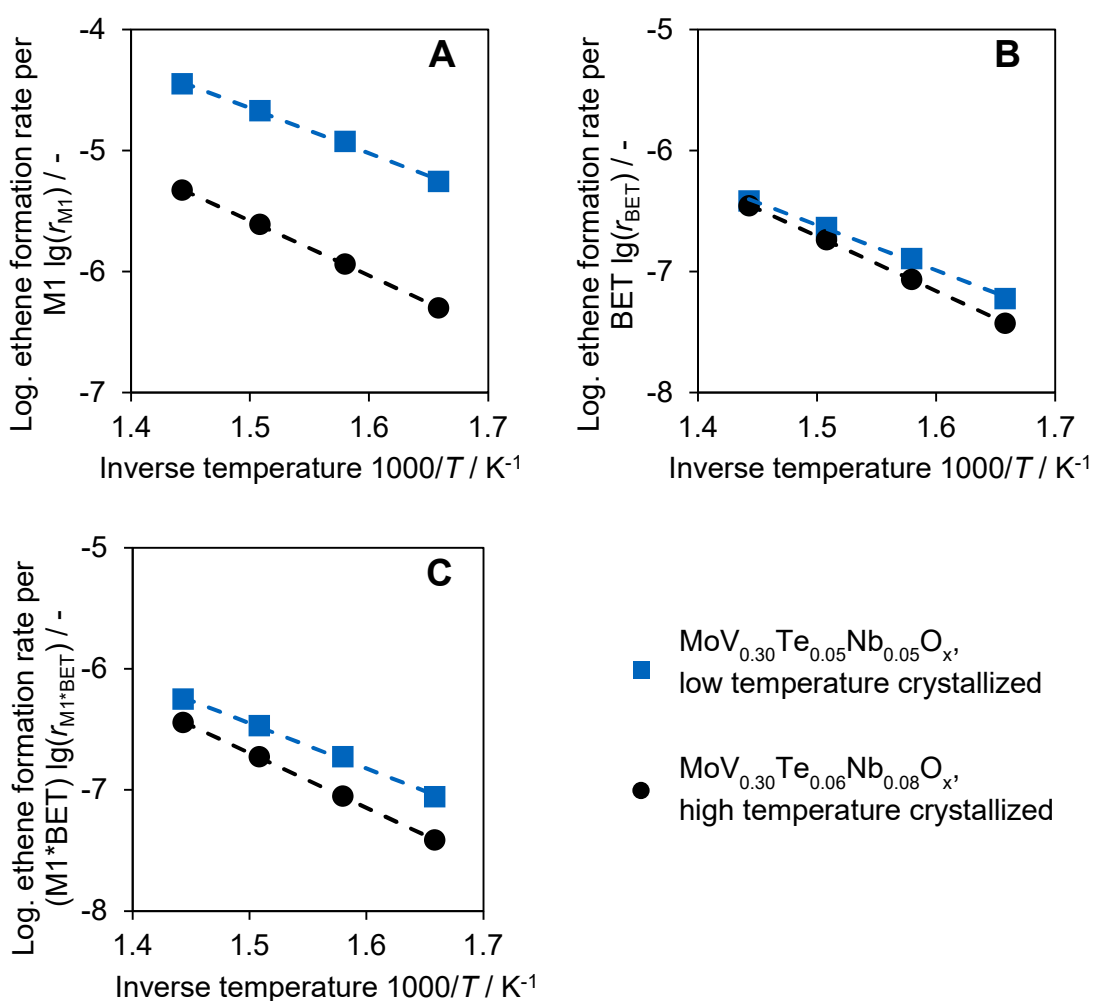

Figure 23: Arrhenius type plot of low (blue squares) and high (black circles) temperature crystallized MoVTeNbO$_x$. Ethene formation rates normalized to M1 content (A), specific surface area (B) and combination of both properties (C).

From the results in Figure 23 it has been concluded that M1 phase crystallized at low temperature under hydrothermal conditions is intrinsically more active than M1 phase crystallized from an amorphous precursor via high-temperature treatment. In order to understand this higher intrinsic activity, annular dark field scanning transmission electron microscopy (ADF-STEM) was used to study the crystal termination of M1 particles in both catalysts (Figure 24). It was found that the particles synthesized by the new method have an irregular and jagged lateral surface (Figure 24A). In contrast, M1 crystals formed via high temperature crystallization showed smooth surfaces (Figure 24B). Analysis of the particles with atomic resolution HAADF-STEM allowed identifying such smooth surfaces as densely packed chains of M_6O_{21} building blocks connected by single MO_6 octahedra, which is a termination with low surface concentration of active sites [148].
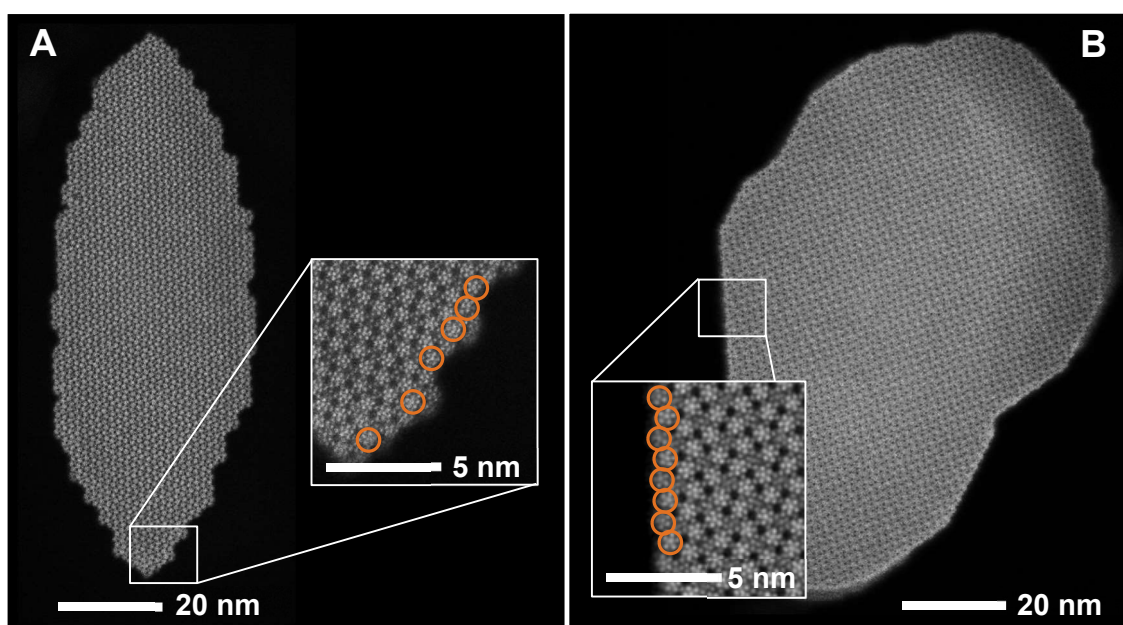

Figure 24: ADF-STEM images of {001} plane of MoVTeNbO$_x$ synthesized by the new method (A) and by the method in reference [1] (B). Insets show representative lateral surface termination. Circles highlight pentagonal M_6O_{21} units.

Previous studies in our group have shown that differences in crystal morphology affect the activity of MoVTeNbO$_x$ catalysts [148]. MoVTeNbO$_x$ materials comprising of a majority of crystal particles with lateral terminations preferentially exhibiting {120} and {210} facets were found to be highly active in the ODH-E reaction. Conversely, materials with a lateral termination predominantly formed by {010} facets yielded low intrinsic activities. These {010} facets are terminated by a zig-zag pattern of pentagonal M_6O_{21} units (sites S5, S6, S8-S11 in Figure 4) that are connected by a single MO_6 octahedron (S3). This

termination does neither expose the active center proposed by Schlögl [141] nor Grasselli [136]. In contrast, the {120} and {210} facets exhibit at least parts of the five-octahedra motif formed by crystallographic sites S2-S4-S7 (see Figure 4), which are statistically occupied by the active V^{5+}=O species [136]. Indeed, it has been shown that samples with morphologies that favor {120} and {210} facets in the crystal termination are intrinsically more active than those with a predominant {010} termination [148].

We have found that in M1 particles formed by the new synthetic method shown here (Figure 24A) crystal termination consisting of regular zig-zag chain of M_6O_{21} units is less frequent than in samples prepared by the standard method (Figure 24B). This implies that particles are terminated by a larger diversity of structural motifs, which frequently includes parts of the S2-S4-S7 ensemble linked to the ODH-E activity of M1-MoVTeNbO$_x$ [136,141]. Stabilization of ODH-E transition states on S4-O-S7 bridging oxygen species via van-der-Waals forces induced by steric constraints in heptagonal channels was recently proposed as the reason for high dehydrogenation activity and selectivity of M1-MoVTeNb [145]. However, diffusion of ethane into pores with a diameter near its kinetic diameter and partially occupied by Te cations is prone to severe mass transport limitation. We therefore believe that the reported differences in activity between M1 and non-porous ODH catalysts can more likely be attributed to dehydrogenation reactions occurring on the pore-mouth of the heptagonal channel. Yet, it should not be ruled out that similar steric constraints can also be imposed by open half-channel motifs formed on jagged lateral surfaces of M1 crystal. Such open half-channel features on jagged crystal surfaces would allow for fast mass transport and hence add additional intrinsic activity compared to smooth surfaces similar to those observed in Figure 24B.

A statistical analysis of the atomic lateral termination of the MoVTeNbO$_x$ particles synthesized by our new method is beyond the scope of this thesis. However, the STEM images shown in Figure 24A strongly suggest that a larger number of metal sites with the potential to host active centers is available on the surface of M1 particles formed at low temperatures, compared to particles crystallized at high temperature (Figure 24B).

The irregular lateral termination of low temperature crystallized M1 particles is hypothesized to result from incomplete saturation of growth sites on the crystal surface. In other words, M1 particles crystallized at low temperatures have not achieved their thermodynamically most favored crystal termination. Thermodynamically unstable surfaces containing a large number of defects are known to grow faster and this way transform into surfaces with a lower free surface energy, which eventually dominate the crystal surface. [195] The most densely packed lateral facet {010}, with its zig-zag chain of

robust M_6O_{21} building blocks, is likely to be the thermodynamically most stable configuration. This assumption is consistent with the predominance of such lateral termination in catalysts crystallized at high temperatures. We therefore conclude that mild crystallization conditions facilitate the formation of facets other than {010} and, as a consequence, the intrinsic catalytic activity of M1 catalysts is dramatically increased.

3.2 Assembly of M_6O_{21} building blocks under hydrothermal conditions

As the growth of different particle facets is a kinetically controlled process, not only the size but also the termination and morphology (related to the surface energy) of M1 particles can be tuned in our method by variation of the hydrothermal synthesis parameters. Therefore, understanding the processes involved in crystallization of M1 is necessary in order to design synthesis protocols that lead to crystalline particles with a high concentration of active sites on the surface. Such synthesis protocols should aim at forming M1 particles exposing highly corrugated crystal surfaces at the expenses of precipitating certain amounts of amorphous solid without a functionality.

A series of samples with nominal stoichiometry $MoV_{0.30}Te_{0.05}Nb_{0.05}O_x$ was prepared following the new synthesis protocol but at different hydrothermal synthesis durations (ranging from 3.5 to 48 h). XRD analysis of the solids obtained from hydrothermal synthesis showed that M1 phase is the majority crystalline component already after 3.5 h of synthesis (Figure 25). It should be noted that 19 – 38 % of amorphous material is present in all the samples. Chemical analysis of the solid fractions was performed by ICP-OES and metal stoichiometry is independent of the synthesis duration and close to the nominal stoichiometry.

The intrinsic activity of M1 phase generated in each sample of Figure 25 is compared. Therefore, ethene formation rates at 330 °C -normalized to the M1 content- are shown in Figure 26. The highest rate, and hence highest intrinsic activity, was found for the catalyst obtained after only 4.5 h of hydrothermal synthesis.
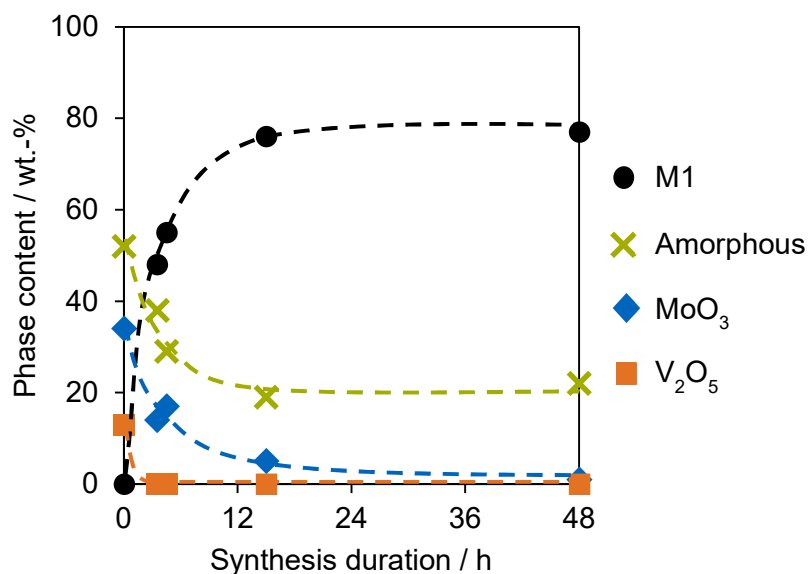
Figure 25: Evolution of M1, MoO_3, V_2O_5 and amorphous phase content in $MoV_{0.30}Te_{0.05}Nb_{0.05}O_x$ samples synthesized according to new method for different hydrothermal synthesis times. Initial mixture ($t = 0$ h) contains 1 wt.-% of crystalline TeO_2 (data point was omitted for sake of clarity).
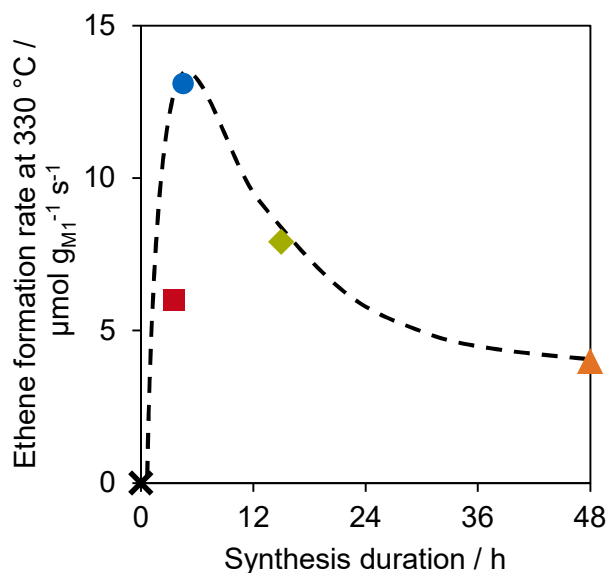

Figure 26: Ethene formation rate at 330°C obtained over $MoV_{0.30}Te_{0.05}Nb_{0.05}Ox$ synthesized at 190 °C and 17.5 bar(a) for various durations. T = 330 °C, p = 1 bar(a), WHSV = 7.0 – 13.8 h^{-1}.

Identical trends are observed in Figure 27 where rates are normalized to the mass of catalysts used, m² of M1 phase and combination of M1 and amorphous phase content (accounting for potential influences of nanocrystalline M1 phase).
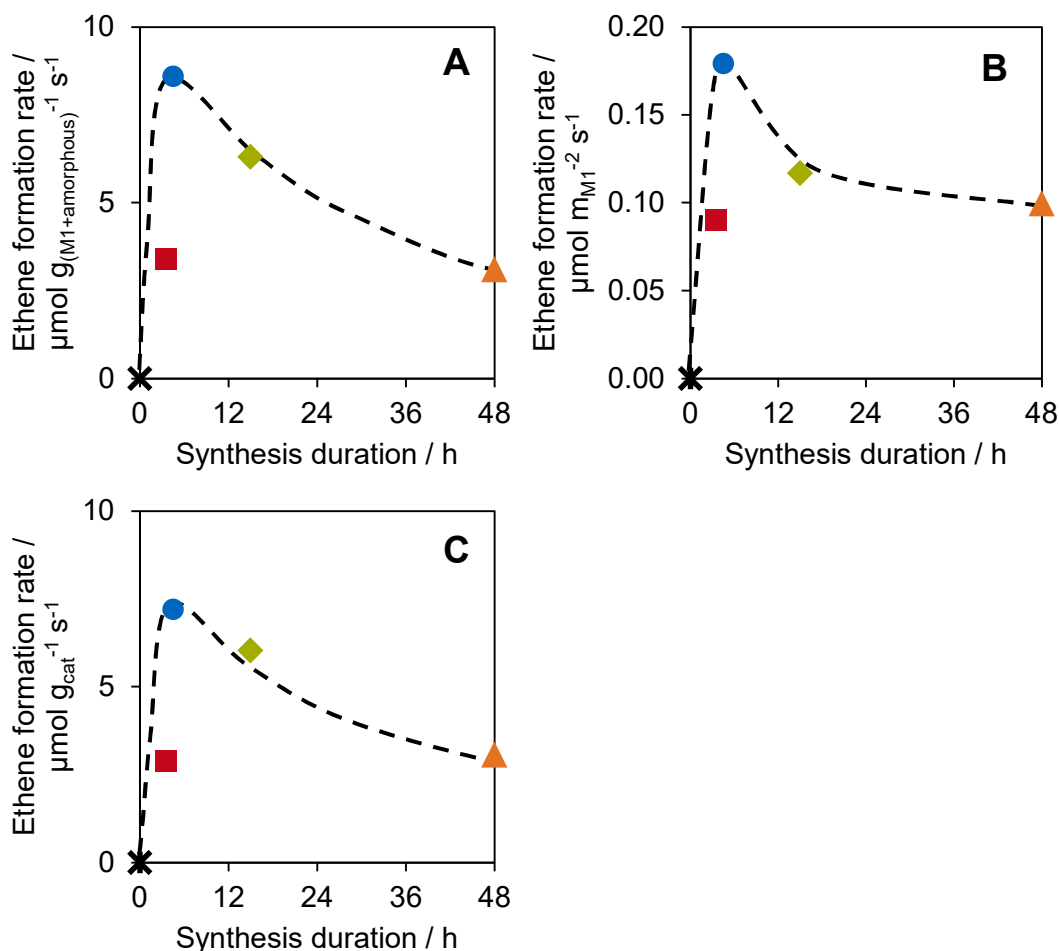

Figure 27: Ethene formation rate at 330 °C obtained over $MoV_{0.30}Te_{0.05}Nb_{0.05}O_x$ synthesized at 190 °C and 17.5 bar(a) for various durations. T = 330 °C, p = 1 bar(a), $WHSV$ = 7.0 – 13.8 h^{-1}. Rates normalized to sum of M1 and amorphous phase content (A), surface of M1 phase (B) and mass of catalyst used (C).

Comparable energies of activation (73 ± 1 kJ mol^{-1}) and comparable selectivities as function of conversion for all tested samples (Figure 28) indicate identical reaction mechanism for the formation of ethene on all tested M1-MoVTeNbO$_x$ catalysts.
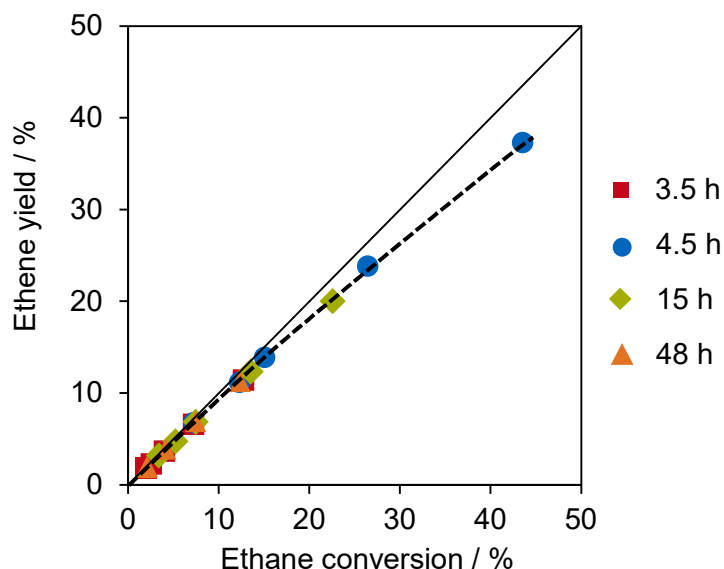
Figure 28: Ethane conversion-ethene yield plot of MoVTeNbO$_x$ catalysts synthesized for various durations. T = 330 - 420 °C, p = 1 bar(a), WHSV = 7.0 – 13.8 h^{-1}.

Therefore, we attribute the high activity of the sample obtained after 4.5 h of hydrothermal synthesis to a higher surface concentration of active sites. As seen in the previous section, a higher concentration of active sites can be achieved by synthesis of M1 particles with a lateral termination abundant in less thermodynamically favored facets such as {120} and {210} [148]. Accordingly, we speculate that nucleation and primary crystal growth of M1 phase are dominant processes during the first 4.5 h of hydrothermal synthesis, leading to the formation of M1 particles with corrugated surfaces which contain a high concentration of active sites.

Figure 29 shows SEM images of M1 particles obtained at the selected synthesis durations (3.5 h, 4.5 h, 15 h and 48 h). Figure 30 shows the corresponding particle size distribution measured along the {001} axis and obtained by statistical analysis of more than 300 particles per sample. While the crystalline phase distribution of the mixed metal oxide precipitate changes considerably during the first 15 h of hydrothermal synthesis (Figure 25), the particle size distribution of M1 particles is affected only in early stages of hydrothermal synthesis. Significant growth of M1 particles along the c-axis is only observed up to 4.5 h of synthesis. After this point, particle length distribution remains virtually constant. Due to the agglomeration and the much smaller dimensions in directions perpendicular to {001} axis of the elongated M1 particles, it is not possible to obtain the corresponding size distribution of the particles thickness.

The decrease of intrinsic catalytic activity observed in Figure 26 for syntheses longer than 4.5 h must, however, be linked to crystal growth processes occurring at later stages of the hydrothermal treatment. Likely, at synthesis times longer than 4.5 h the dominant process in the crystallization is deposition and reorganization of M1-building blocks on high-energy facets of existing crystals, leading to thermodynamically more stable surfaces (i.e., preferentially the {010} facet). As already discussed in the previous section, such changes in the atomic configuration of the lateral termination have a major impact in the activity of the mixed oxide.
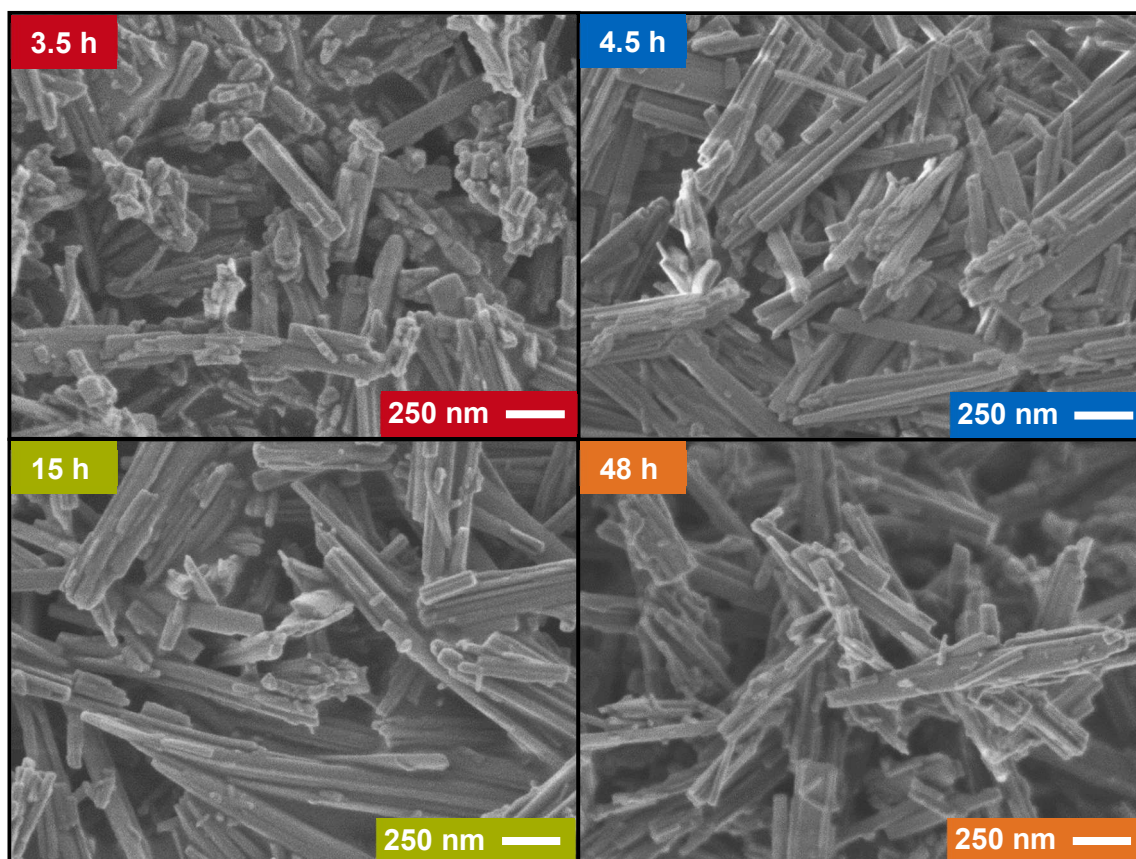

Figure 29: SEM images of $MoV_{0.30}Te_{0.05}Nb_{0.05}O_x$ synthesized at 190 °C and 17.5 bar(a) for various durations
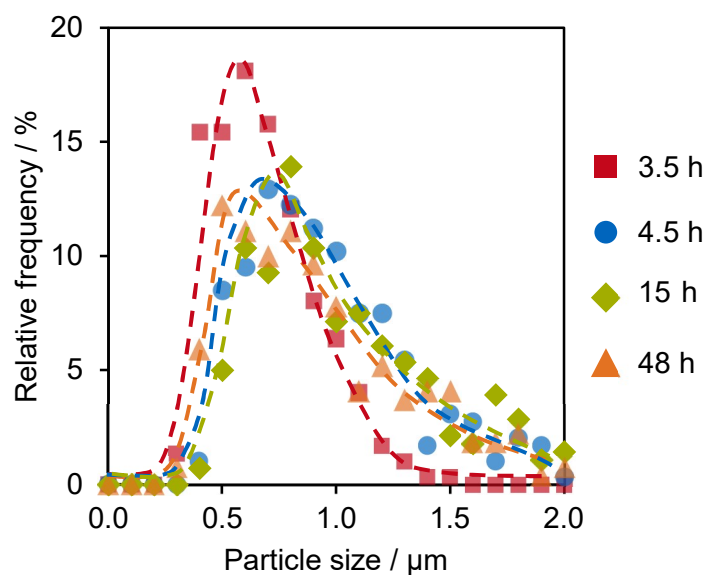
Figure 30: Particle length distributions of $MoV_{0.30}Te_{0.05}Nb_{0.05}O_x$ synthesized at 190 °C and 17.5 bar(a) for various durations.

The effects of hydrothermal synthesis duration on M1 crystal termination and particle morphology were once again assessed using HAADF-STEM imaging (Figure 31). M1 samples synthesized at short times (below 4.5 h) frequently show aggregates of small M1 particles including unordered domains and highly corrugated surfaces. Such unordered domains are likely the cause for the comparatively high content of X-ray amorphous material detected by XRD analysis. In contrast, it appears that at extended synthesis duration, aggregates of small particles become less frequent and larger particles are formed by aggregation and intergrowth of smaller needles.
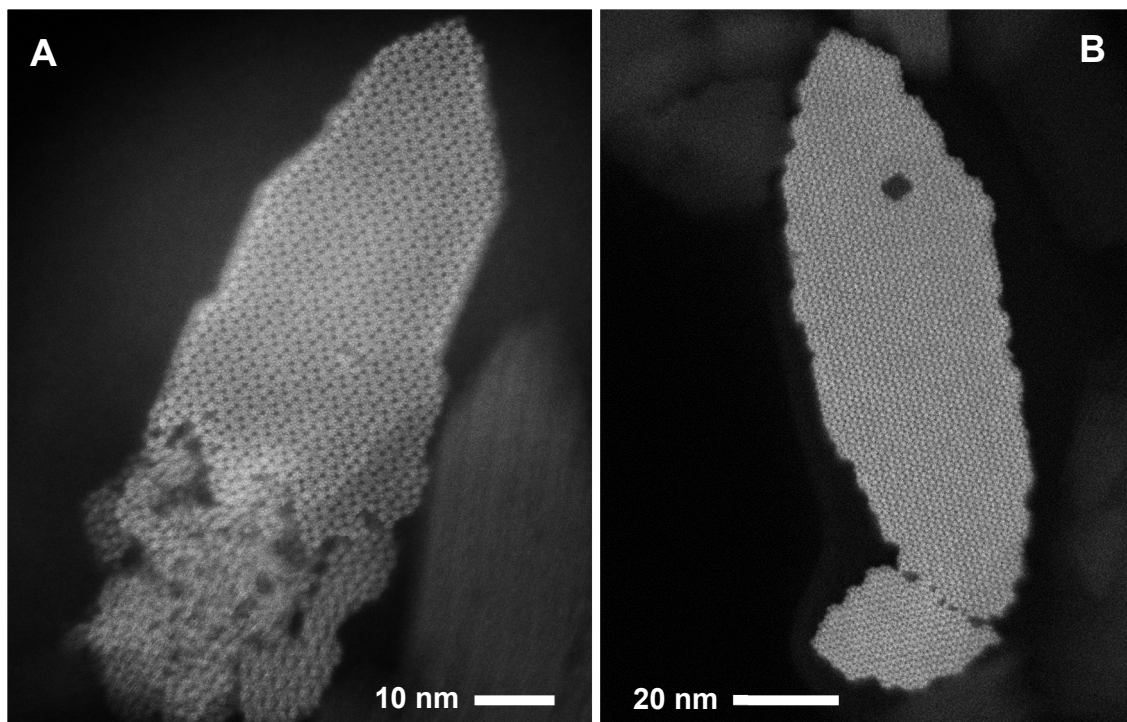
Figure 31: HAADF-STEM images of $MoV_{0.30}Te_{0.05}Nb_{0.05}O_x$ M1 crystals synthesized for 3.5 h (A) and 48 h (B) according to the new method.

In order to obtain a better resolution of the synthesis reactions taking place during hydrothermal synthesis, aliquots of the reacting slurry were periodically extracted from the autoclave over the course of the heating ramp and at final hydrothermal synthesis conditions at 190 °C and 17.5 bar(a). X-ray diffraction analyses of the solid fractions was performed (selected diffractograms can be seen in Figure 32B) and the results of the phase analysis and Rietveld refinement are shown in Figure 33. As a reference, diffractograms of the reactants MoO_3, V_2O_5, $Nb_2O_5 \cdot 1.5H_2O$ and TeO_2 are included in Figure 32A. Also, it should be noted that the small amount of solid collected from extracted aliquots does not allow a quantification of the amorphous content as in Figure 25. Therefore, percentages shown in Figure 33 are with respect to the crystalline part of the samples.

XRD and Rietveld analyses of the individual metal oxide reactants have shown that V_2O_5 is fully crystalline and $Nb_2O_5 \cdot 1.5H_2O$ reactant is fully amorphous. MoO_3 contains an amorphous content of 59 wt.-% and TeO_2 contains 68 wt.-% of amorphous material. In Figure 25 and Figure 33, the data point at 0 h corresponds to the composition of the solid metal oxide fraction used in the initial synthesis mixture. Rietveld analysis gives in this

case a 34 wt.-% content of crystalline MoO_3, 13 wt.-% V_2O_5, 1 wt.-% of crystalline TeO_2 and 52 % of amorphous material, which is consistent with the expected crystalline composition for the physical mixture according to their individual degree of crystallinity. The amorphous solid complies the totality of $Nb_2O_5 \cdot 1.5H_2O$ reactant and the proportional amounts of amorphous MoO_3 and TeO_2. Analyses of the crystalline fraction of solid aliquots show that the only reactant found as crystalline species in the slurry after 2.5 h under hydrothermal conditions is MoO_3. $MoVTeNbO_x$-M1 phase was first detected in the solid after 3.5 h and Rietveld analysis shows that it is already the most abundant crystalline phase at this point of the hydrothermal synthesis. Virtually all crystalline MoO_3 has been solvated and/or incorporated in M1-$MoVTeNbO_x$ after 15 h of hydrothermal synthesis. In good agreement, the quantification of crystalline and amorphous content in catalysts prepared at different durations (Figure 25) shows that the crystalline composition of the material did not change further for hydrothermal synthesis longer than 15 h.
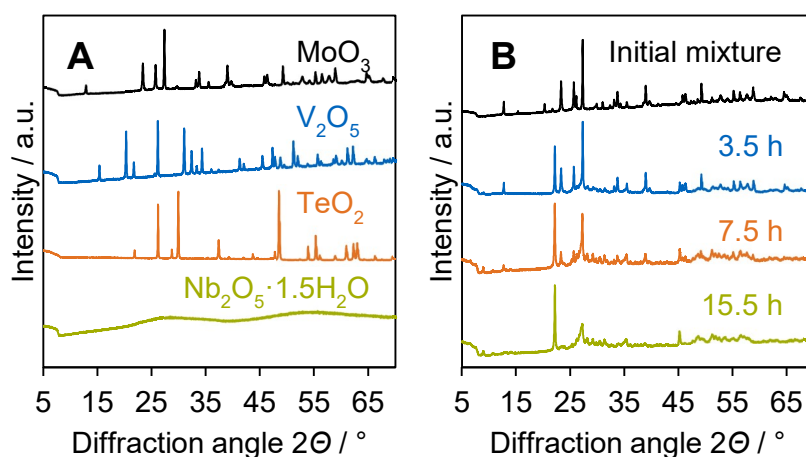

Figure 32: X-ray diffractograms of reactants (A) and selected aliquots (B) obtained during hydrothermal synthesis (190 °C, 17.5 bar(a)) of $MoV_{0.30}Te_{0.05}Nb_{0.05}O_x$ according to new method.
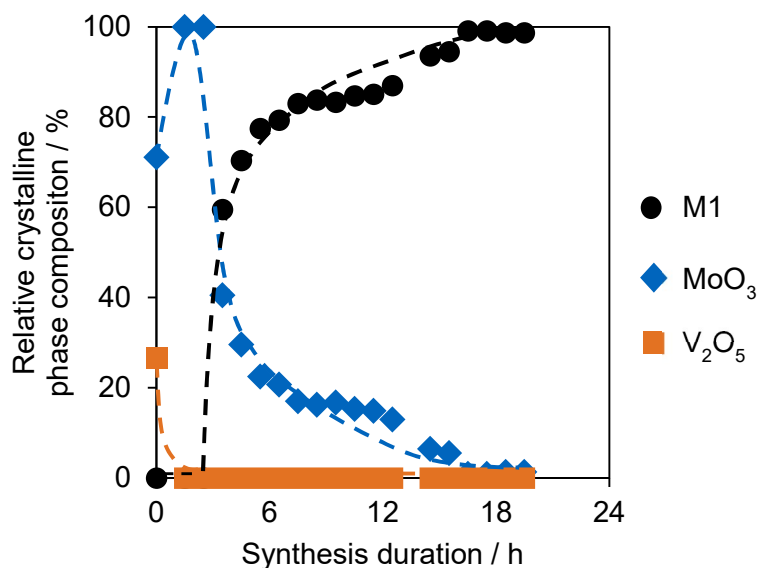
Figure 33: Results of Rietveld refinement of initial mixture and dried aliquots. Values are normalized to the totality of crystalline material. Initial mixture (t = 0 h) contains 4 % of crystalline TeO_2 (data point was omitted for the sake of clarity).

Because the most pronounced changes in terms of crystal growth and crystal phase composition occur within the first 4.5 h of the new synthesis method, we next studied the metal ion (cluster) speciation in solution in this time range. For this purpose, we measured the metal concentrations in solution, pH value and UV-vis spectra of periodically extracted filtrate aliquots. As reference experiments, we also extracted and analyzed aliquots during a synthesis via the new method but in absence of additives, and during a synthesis via the method described in reference [1].

Filtrates from both syntheses leading to M1 (procedures presented in this work using additives and in reference [1]) show similar UV-vis absorption spectra (Figure 34A and Figure 34C, respectively). Absorption bands at ca. 300 nm and ca. 570 nm (with shoulders at ca. 670 nm and 800 nm) are observed in both cases. The absorptions at 570 nm, 670 nm and 800 nm are attributed to a $\{M_{102}\}$ ($\{Mo_{72}V_{30}\}$-type) Keplerate metal cluster (Figure 35). This polymolybdate cluster contains 12 pentagonal M_6O_{21} structural motifs connected by partially reduced single-metal-octahedra linking units [106,196,197]. The same M_6O_{21} motif is also found in M1, as can be seen in Figure 4 (sites S5, S6 and S8 - S11). The bands at ca. 570 nm and 800 nm are attributed to $Mo^{6+} \leftarrow V^{4+}$ and $Mo^{6+} \leftarrow Mo^{5+}$ intervalence charge transfers, respectively. This indicates the presence of mixed $Mo^{5+/6+}$ centers typical for the Mo_6O_{21} building block in presence of V^{4+} species [198]. Strong

50

absorbance in the UV range below 400 nm was also observed in spectra of $\{Mo_{72}V_{30}\}$ reported by the groups of Ueda [106] and Hill [197].

In the case of the synthesis starting from metal oxide reactants (Figure 34A), initial filtrate does not present UV-vis absorption bands. As the synthesis advances, first the band at 800 nm, assigned to the M_6O_{21} building block, develops. At 1.5 h, the typical absorption bands of $\{M_{102}\}$ can be observed. This indicates slow solubilization of Mo and V species under hydrothermal conditions and subsequent connection of building blocks to form the polymolybdate cluster in solution. Conversely, for the recipe starting from metal salts (Figure 34C), the first UV-vis spectrum after mixing the reactants already shows the presence of $\{M_{102}\}$ clusters in solution and the intensity of the bands assigned to this species decreases over synthesis duration. After 2.5 h under hydrothermal conditions, only the band at 800 nm can be observed, indicating full decomposition or precipitation of $\{M_{102}\}$ clusters over time, leaving only M_6O_{21} building blocks in solution.

In contrast, spectra of the reference synthesis in absence of additives (Figure 34B) show only a single absorption band in the range of 400 - 500 nm, which is tentatively attributed to reduced $\{V_6\}$ species [199]. The absorption bands attributable to Keplerate clusters could not be found in any filtrate taken for 15 h under hydrothermal conditions. This highlights once again that the presence of additives is necessary for the formation of M1 phase from a reacting mixture based on the metal oxides.
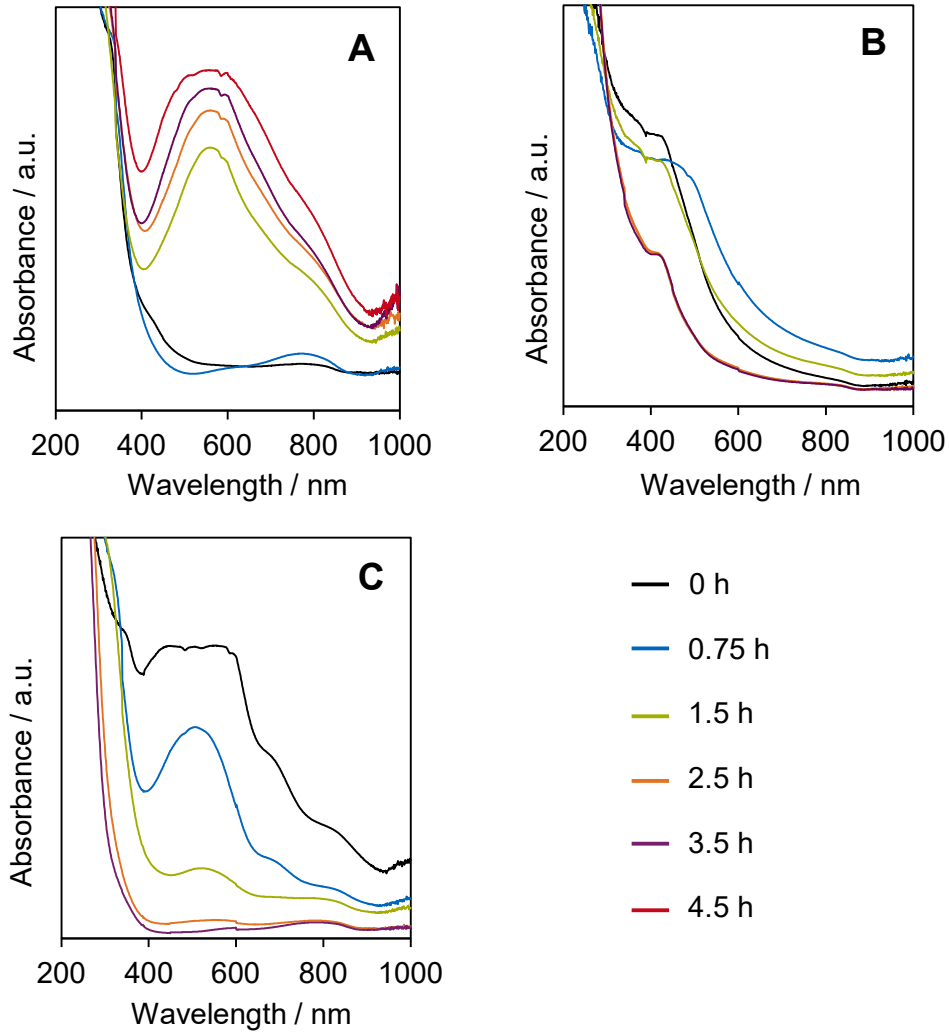
Figure 34: UV-Vis spectra of filtrates extracted from MoVTeNb slurries at various times during hydrothermal synthesis. Synthesis according to procedure presented in this work in presence of additives (A); reference synthesis as in (A), but without additives (B); synthesis according to procedure presented in reference [1] (C).
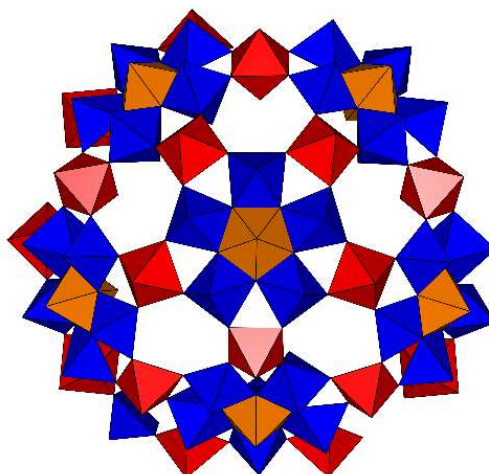
Figure 35: {M_{102}} type Keplerate cluster. Pentavalent M_6O_{21} centers (orange and blue) are connected by partially reduced Mo/V sites (red) [106,196,197].

A number of synthesis mechanisms for M1-MoVTeNb mixed metal oxide [1,111] and iso-structural orthorhombic MoV [106] and MoVSb [109] mixed metal oxides have been proposed in the literature. Based on spectroscopy performed during hydrothermal synthesis, {M_{102}} type Keplerate has been suggested as a donor of the M_6O_{21} building blocks in the synthesis of M1-type mixed metal oxides [1,106,109]. It is believed that the orthorhombic M1 mixed metal oxide phase is formed by attachment of the typical structure motif M_6O_{21} onto primary particles of the M1 phase [106,109,115]. The crystal growth would take place by further attachment of M_6O_{21} clusters preferentially onto the {001} basal plane of the M1 crystal. This is based in the fact that M1 particles preferably grow in the [001] direction [93], as seemed to be indicated by the higher M1 yields reported when seed particles with high basal surface area were added to a typical synthesis mixture [115].

pH has previously been reported as a governing factor in synthesis of different Mo-V mixed metal oxide phases [106,200,201]. Conversion of {$Mo_{72}V_{30}$} to orthorhombic M1-MoV phase was reported to occur only within a pH range of ca. 2.5 to 3.5, while hexagonal and trigonal mixed metal oxides were reported to form at lower pH and no solids precipitated at pH above 3.5 [106]. In our experiments, suspending the metal oxide reactants in water without addition of the additives resulted in a pH of 2.7 and did not change considerably during hydrothermal treatment (Table 4). Addition of the synthesis additives leads to initially lower pH values (ca. 1.8) but increased within 1.5 h (same point in time at which {M_{102}} is detected for the first time) to 2.5. It should be noted that there was not any conversion either to Keplerates or to any of the crystalline MoVTeNbO$_x$ phases in absence of additives, even though pH of the mixture falls into the range

feasible for formation of M1. Hence, we believe that the role of additives ethylene glycol, citric acid and oxalic acid is primarily to act as chelating and reducing agents. This is consistent with previous reports which found formation of structurally similar $\{M_{132}\}$ Keplerates takes place only if partially reduced $\{Mo_2\}$ centers are available [113,114,202].

Table 4: pH values in filtrate aliquots extracted from the hydrothermal synthesis of $MoV_{0.30}Te_{0.05}Nb_{0.05}O_x$ at various durations.

Synthesis duration / h	Oxide reactants with additives	Oxide reactants without additives	Soluble reactants
0	1.8	2.7	1.6
0.75	1.7	2.6	1.6
1.5	2.5	2.7	1.8
2.5	2.6	2.6	2.0
3.5	2.4	2.4	1.9
4.5	2.4	2.4	1.9

The chemical composition of filtrates collected at different synthesis times was also analyzed and the concentration profiles are depicted in Figure 36. Mo and V were the most abundant species in all three experiments, which is expected given the stoichiometry of the reaction mixtures (Mo:V:Te:Nb = 1:0.30:0.05:0.05 and Mo:V:Te:Nb = 1:0.40:0.10:0.10). Metal oxides only poorly dissolve in absence of synthesis additives. Solubility is only slightly enhanced when hydrothermal conditions are reached (Figure 36B). Addition of the hydrocarbon additives increases the metal concentrations by half (Mo, Te) to one (V, Nb) order of magnitude (Figure 36A). Under hydrothermal conditions, the metal concentrations in solution also increase with time. When using metal salt reactants (Figure 36C), initial concentrations found in solution are about two orders of magnitude larger compared to the reference synthesis from metal oxide reactants without additives. Although the synthesis starting from metal salts uses an identical nominal molar concentration of Mo (0.5 mol L^{-1}) and similar amounts of V, Te and Nb compared to the new method, the higher solubility of metal salts obviously affect the initial composition of the liquid phase. In this case, a strong decrease of metal concentrations is observed with synthesis duration. The sharp decrease of solvated metal ions is in good agreement with the decreasing band intensity of $\{Mo_{102}\}$ observed in UV-vis (Figure 34C).
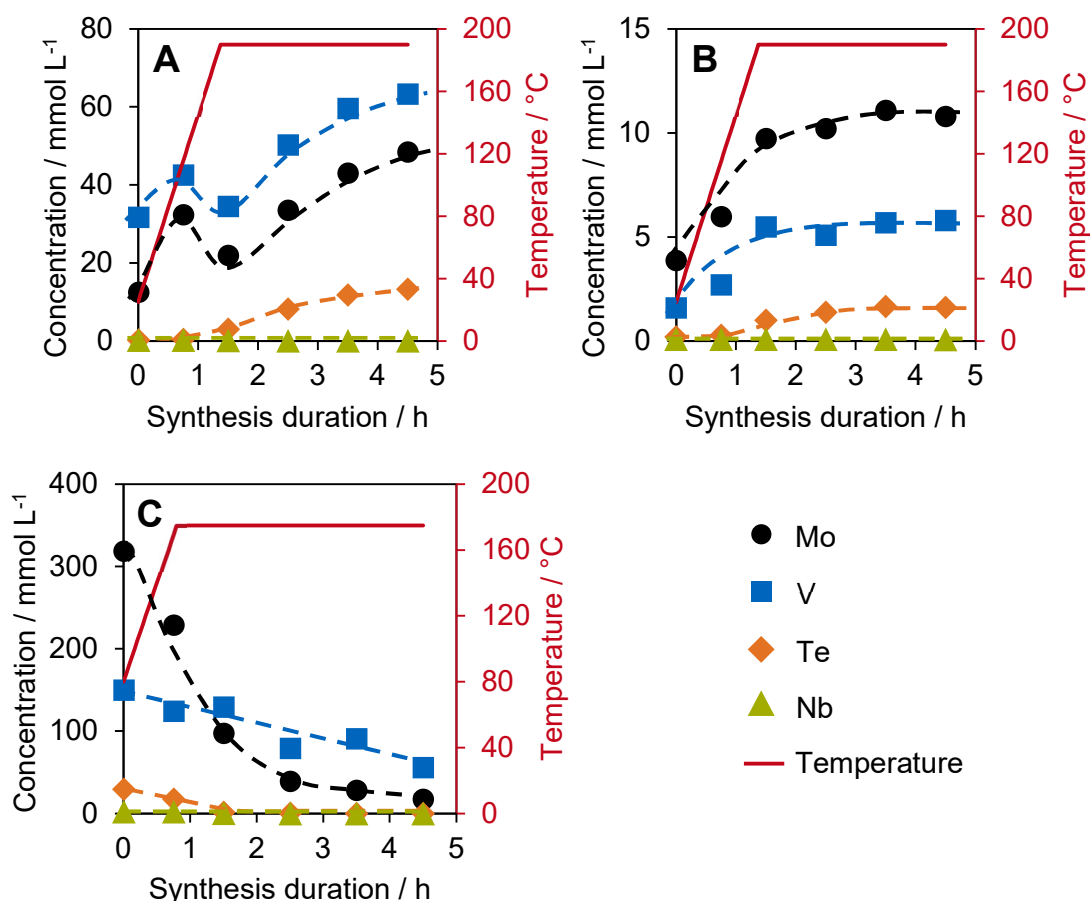
Figure 36: Concentration profiles of metals in the filtrates obtained from MoVTeNb synthesis slurries at various times during hydrothermal synthesis. Synthesis according to procedure presented in this work in presence of additives (A); reference synthesis as in (A), but without additives (B); synthesis according to procedure presented in reference [1] (C).

Based on the results of elemental analysis, pH analysis and UV-vis spectroscopy, we conclude that, in the synthesis of M1-MoVTeNbO$_x$ using our new method, {M$_{102}$} clusters are formed under acidified and reducing hydrothermal conditions. These clusters contain the pentagonal structural motif M$_6$O$_{21}$ common with the orthorhombic M1 phase. The use of acidic and reducing additives to the synthesis mixture is strictly necessary for the formation of these M1 building block donor clusters. We further hypothesize that the low concentration of metal cluster intermediates in solution, and hence limited availability of M$_6$O$_{21}$ building blocks, allow for a slow precipitation of the solid mixed oxide and the formation of a long range ordered material. As it can be seen from XRD analysis (Figure 25 and Figure 33), SEM (Figure 29 and Figure 30) and STEM images (Figure 24), during the first 4.5 h of synthesis, mainly nucleation and growth of M1 particles with jagged

surfaces are taking place. This process is driven by the kinetically limited addition of M_6O_{21} building blocks to crystal growth sites of primary M1 particles. When hydrothermal conditions are sustained for longer than 4.5 h, a decrease in the activity per gram of M1 is observed (Figure 26), which is attributed to further growth of M1 particles towards a more thermodynamically stabilized surface termination, where a lower concentration of active sites is exposed.

3.3 Conclusions

This chapter describes the chemical processes occurring in direct crystallization of M1-MoVTeNbO$_x$ under hydrothermal conditions and compares them to a standard synthesis protocol. Identical M_6O_{21} building block donating Keplerate clusters where observed for both synthesis approaches. However, concentration of Keplerates is initially significantly lower in case of the synthesis making use of poorly soluble metal oxide reactants. The mixed metal oxides prepared by the new synthesis protocol exhibit an unusually high intrinsic activity (normalized per square meter of M1 phase). This superior performance is attributed to the fact that the synthesis conditions used in this new method allow for the formation of M1 crystals with an irregular termination. Such crystal termination has been observed to expose a larger concentration of centers active in ethane ODH. This thermodynamically instable crystal termination is the result of low metal concentrations in solution allowing for slow precipitation of building blocks. When tuning the synthesis duration of M1-MoVTeNbO$_x$, a maximum of intrinsic activity in ethane oxidative dehydrogenation can be observed for intermediate durations. When hydrothermal conditions are sustained passed that optimal duration, high surface-energy facets in M1, rich in active sites, are converted to thermodynamically more stable - yet catalytically inactive - crystal terminations.

These findings show that identification of catalytically active structures in the crystal termination of complex mixed metal oxide structures and understanding of crystallization kinetics can be used to design synthesis protocols that yield highly active metal oxide catalysts.

3.4   Associated content and contributions

Part of the content of this chapter is based on the publication *Design and synthesis of highly active MoVTeNb-oxides for ethane oxidative dehydrogenation* published in Nature Communications (reference [81]). The structure and content of this chapter differs from the publication. The synthesis protocol was patented (see Chapter 13 of this work and references [191-193]).

Daniel Melzer performed the synthesis, XRD analysis and kinetic tests of the mixed metal oxide catalysts and wrote the manuscript. Dr. Gerhard Mestl and Dr. Klaus Wanninger advised the research and contributed to writing of the publication. Dr. Maricruz Sanchez-Sanchez is the project leader and Prof. Dr. Johannes A. Lercher is the principal investigator of this project. They both supervised the research and discussed results and conclusions.

4 Impact of Te and Nb on ODH reaction pathways over MoVTeNbO$_x$ catalysts

This chapter is devoted to the investigation of metal stoichiometry effects on the pathways of ethane partial and total oxidation and the resulting product distribution. For this purpose, kinetic experiments are combined with results from bulk and surface sensitive physico-chemical characterization of different M1-MoV(TeNb)O$_x$ variants. Phase-pure M1-MoVO$_x$ and M1-MoVTeNbO$_x$ catalysts were tested in the selective oxidation of ethane and ethene. MoVO$_x$ shows lower ethane dehydrogenation activity and higher tendency to total oxidation of the desired intermediate ethene resulting in overall poorer ODH performance. At least three different types of reaction pathways can be distinguished. Higher total oxidation activity of MoVO$_x$ is linked to higher concentration of unselective oxygen species.

4.1 Motivation

In the previous chapters, the role of the vanadium concentration and the effects of crystal termination on the activity of M1-type catalysts were discussed. Catalytic performance increases with an increase in vanadium content (see Chapter 2). This behavior is attributed to a higher density of V^{5+}=O species located in the presumed active ensemble of crystallographic sites S2-S4-S7 [75,135,141,142]. It was also already mentioned in passing in Chapter 2 that Te and Nb content do have an effect on catalysis. The role of Te and Nb (and also other promoting elements such as Sb) is not fully understood. Only recently systematic studies comparing MoVO$_x$ and MoVTeNbO$_x$ in terms of crystal structure, reactivity and electronic properties were published [155,203]. We aim to further shed light on the impact of metal stoichiometry on the kinetics of hydrocarbon oxidation over M1-type catalysts. Using our new synthesis method it is possible to prepare a series of phase pure M1-MoVTeNbO$_x$ mixed metal oxides (chapter 2). This set of four quaternary catalysts, together with ternary MoVTeO$_x$ and MoVNbO$_x$ and binary MoVOx references, with constant V/Mo ratio allows the investigation of the effect of Te and Nb content on ethane oxidation catalysis.

4.2 Effects of Te and Nb stoichiometry on ODH activity and selectivity of M1-MoV(TeNb)O_x

In chapter 2, a set of five M1-phase containing catalysts (nominal composition $MoV_{0.30}Te_{0.05-0.10}Nb_{00.05-0.10}O_x$ and $MoV_{0.30}O_x$) was introduced and investigated in terms of crystalline composition and ethene productivity. Here, we aim to further investigate the influence of metal stoichiometry on the production of side products CO_x and acetic acid. For the sake of comparison also ternary $MoV_{0.30}Te_{0.05}O_x$ and $MoV_{0.30}Nb_{0.05}O_x$ mixed metal oxides were prepared.

Table 5 shows the physico-chemical properties of the seven catalysts as prepared. As already shown in chapter 2, the binary and quaternary samples contain a majority amount of M1 phase, with the rest of the mixed oxide being predominantly amorphous material. Only trace amounts of secondary crystalline phases ($\leq$ 2 wt.-% NbO_2 or metallic Te) were found in three of the samples with the other two containing only crystalline M1 and amorphous solid. The syntheses of the ternary combinations of M1 phase ($MoV_{0.30}Te_{0.05}O_x$ and $MoV_{0.30}Nb_{0.05}O_x$) were not successful with the present synthesis method, in the sense that unidentifiable secondary crystalline phases were found in significant concentrations in the materials or M1 phase partly decomposed upon exposure to reaction temperatures (Figure 37). Because it is difficult to rule out a contribution of the additional phases to catalysis of secondary reactions – and thus to the selectivity to products – the ternary $MoVTeO_x$ and $MoVNbO_x$ materials were not included in the further study.

Table 5: Physico-chemical properties of as-prepared $MoV_{0.30}Te_{0-0.10}Nb_{0-0.10}O_x$.

ICP-OES (in brackets: nominal) formula	BET / $m^2\,g^{-1}$	Internal area / $m^2\,g^{-1}$	Pore volume / $cm^3\,g^{-1}$	M1 / wt.-%	Amorphous / wt.-%	Other phases
$MoV_{0.30}O_x$ ($MoV_{0.30}O_x$)	97	53	0.16	n.d. [a]	n.d. [a]	n.d. [a]
$MoV_{0.30}Te_{0.05}Nb_{0.05}O_x$ ($MoV_{0.30}Te_{0.05}Nb_{0.05}O_x$)	59	30	0.11	77	22	none
$MoV_{0.31}Te_{0.05}Nb_{0.10}O_x$ ($MoV_{0.30}Te_{0.05}Nb_{0.10}O_x$)	71	93	0.16	58	40	NbO_2
$MoV_{0.31}Te_{0.12}Nb_{0.08}O_x$ ($MoV_{0.30}Te_{0.10}Nb_{0.05}O_x$)	74	9	0.03	52	47	Te^0
$MoV_{0.30}Te_{0.10}Nb_{0.09}O_x$ ($MoV_{0.30}Te_{0.10}Nb_{0.10}O_x$)	87	49	0.19	59	40	Te^0
n.d. ($MoV_{0.30}Te_{0.05}O_x$)	28 [b]	18 [b]	0.07 [b]	n.d. [c]	n.d. [c]	n.d. [c]
n.d. ($MoV_{0.30}Nb_{0.05}O_x$)	60 [b]	35 [b]	0.09 [b]	n.d. [c]	n.d. [c]	n.d. [c]

a) Diffractogram resembles poorly crystallized M1 phase. Rietveld refinement was hence not possible due to missing long range order.
b) Determined after pre-conditioning at 400 °C in flow of nitrogen.
c) Apparent phase mixture of M1 phase and other, non-identifiable, secondary crystalline phases
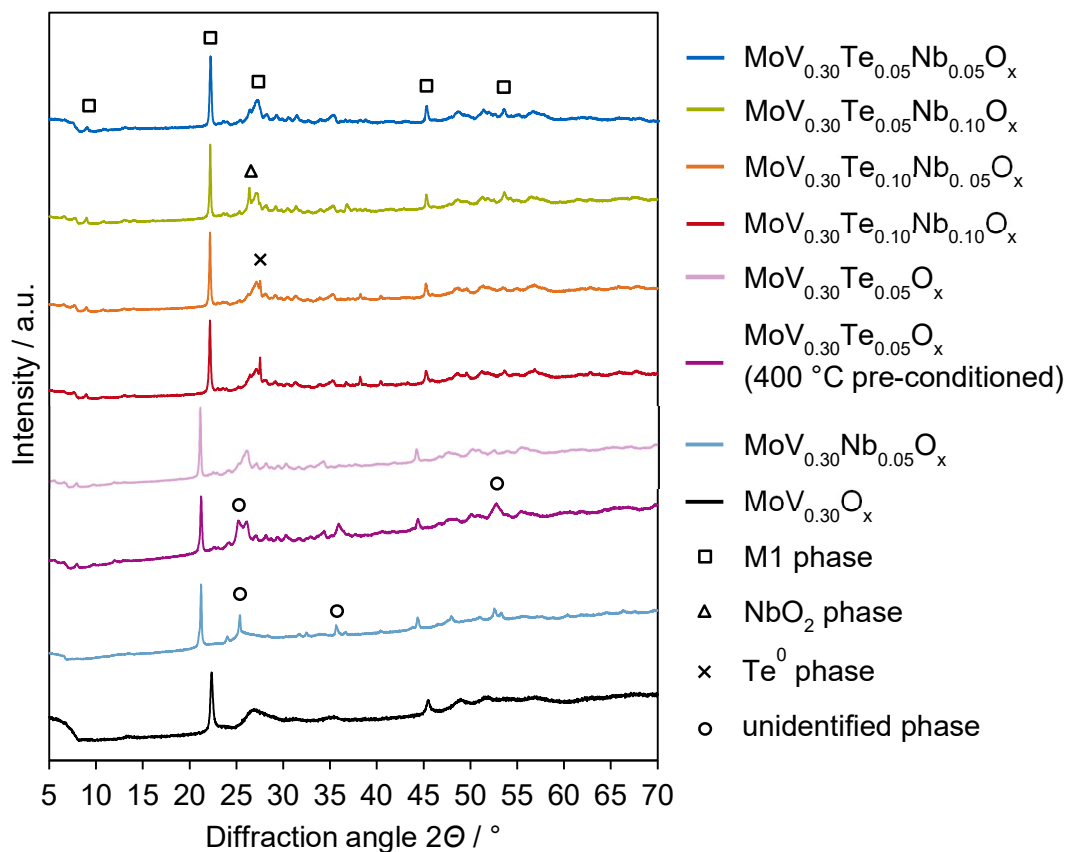
Figure 37: Diffractograms of as prepared $MoV_{0.30}Te_{0-0.10}Nb_{0-0.10}O_x$ mixed oxides. Labels indicate main constituent crystalline phases. Shift of diffraction angles to lower values in $MoV_{0.30}Te_{0.05}O_x$ and $MoV_{0.30}Nb_{0.05}O_x$ samples is likely due to subtle misalignment of XRD detector.

Catalytic activity was found to vary strongly within the investigated range of binary and quaternary metal compositions. Figure 38 shows the ethene production rates, normalized to M1 content, obtained over the five different catalysts. Already in chapter 2 it was shown that the presence of Te in intermediate amounts (Te/Mo = 0.05, blue symbols) results in the highest rates. Higher Te content (Te/Mo = 0.10, green) or absence of Te and Nb (black diamonds) results in lower ethene formation rates. The Nb/Mo ratio does not affect the rates within the tested range of stoichiometries (Nb/Mo = 0.05, circles and Nb/Mo = 0.10, triangles).
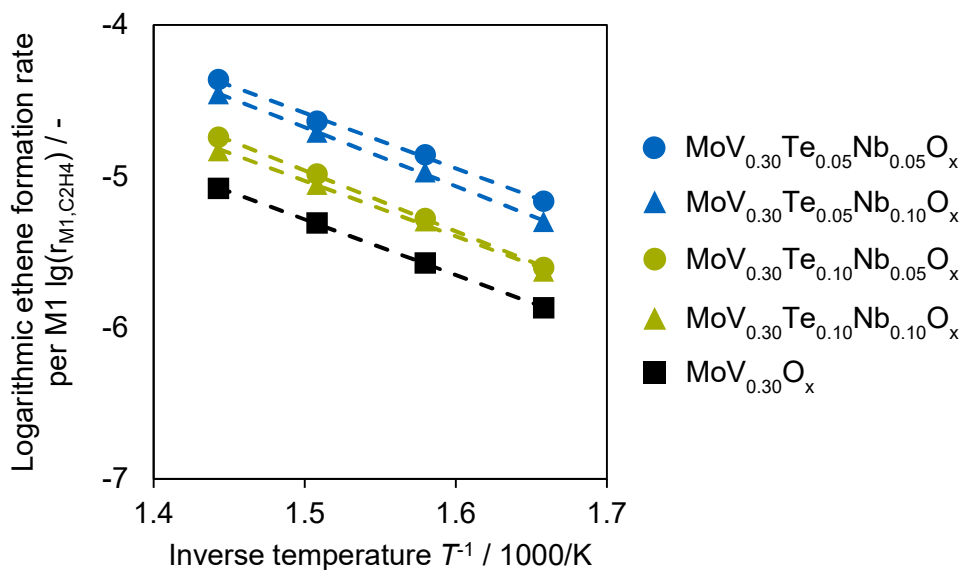
Figure 38: ODH-E activity of various MoV(TeNb)O_x formulations. Reactions conditions applied: T = 330 – 420 °C, C_2H_6:O_2:He = 9:9:82, p = 1 bar(a), $WHSV$ = 20 h^{-1}.

The energies of activation obtained for ethene production were identical for all tested catalysts, with a value of 76 ± 2.0 kJ mol^{-1}. Therefore, differences in ethene formation rates are only due to differences in pre-exponential factor. This shows that the reaction mechanism of ODH-E is not affected by the chemical composition within the tested range, but stoichiometry influences the concentration of active sites.

While the chemical composition does not to appear to affect the ethene formation mechanism, it indeed has an effect on selectivities and hence on the product distribution obtained over various catalysts. Figure 39 shows selectivities to ethene (A), CO (B) and CO_2 (C) as a function of ethane conversion obtained over the above five catalysts. Different catalytic behaviors can be distinguished. The catalysts in which Te/Mo is lower or equal to Nb/Mo (all shown in blue), showed the highest ethene selectivity up to conversion levels of about 50 %. In contrast, the catalyst in which Te/Mo is larger than Nb/Mo (green) and the one without any Te and Nb (black) show higher selectivities to CO and CO_2. Selectivity to CO_2 is identical over sample $MoV_{0.30}Te_{0.10}Nb_{0.05}O_x$ and sample $MoV_{0.30}O_x$, while $MoV_{0.30}O_x$ sample shows in general the highest CO selectivity.
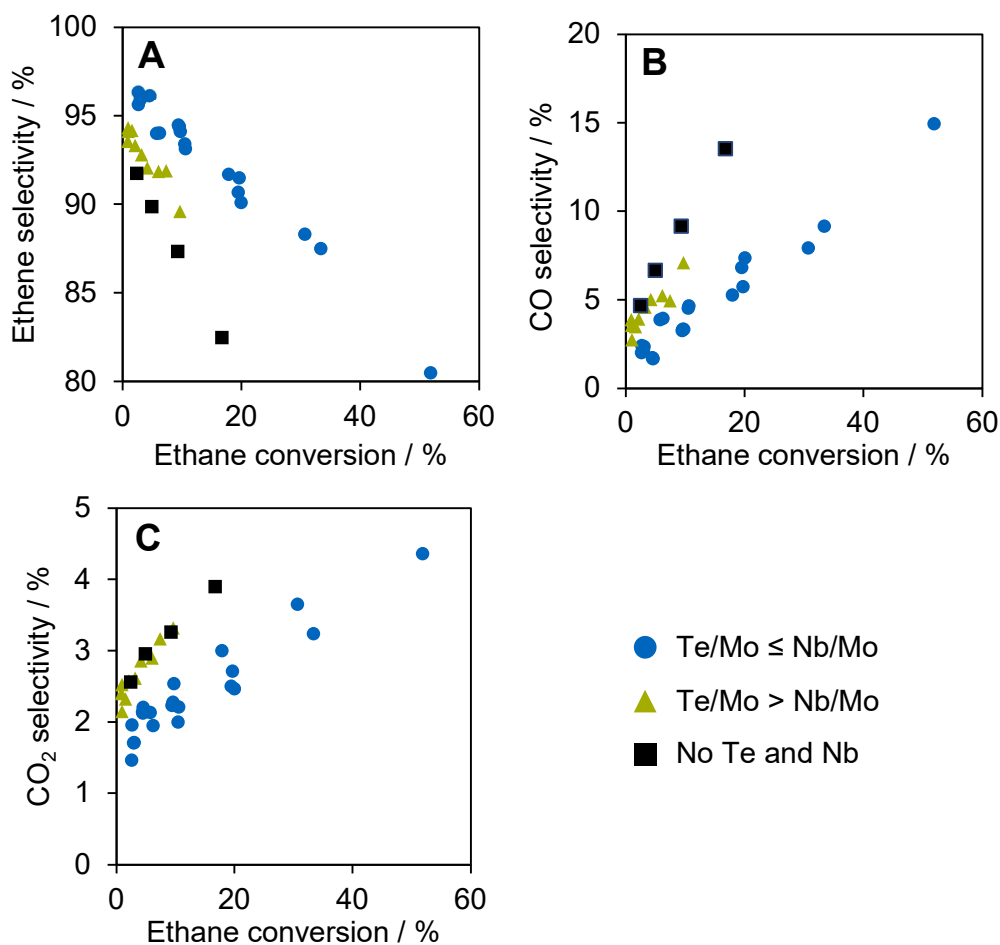
Figure 39: Ethene (A), CO (B) and CO_2 (C) selectivities for various $MoV(TeNb)O_x$ formulations in ODH-E. Reactions conditions applied: T = 290 – 370 °C, C_2H_6:O_2:He = 9:9:82, p = 1.0 bar(a) (B-M1), $WHSV$ = 3.6 – 17.4 h^{-1}.

It appears that the balance between the Te and Nb occupancies in the M1 lattice on one hand, and the Mo-V "backbone" on the other hand governs the selectivity of the catalyst. In order to study the origin of these observations, we selected two samples for further kinetic and physico-chemical characterization: quaternary $MoV_{0.30}Te_{0.05}Nb_{0.05}O_x$ ("Q-M1" in the following) showing both high activity and selectivity to ethene, and binary $MoV_{0.30}O_x$ ("B-M1" in the following) showing comparably poor activity and selectivity in ethane ODH.

4.3   Physico-chemical characterization

Figure 40 shows X-ray diffractograms and Table 6 summarizes physico-chemical properties of B-M1 and Q-M1 samples after preconditioning to 400 °C in flowing nitrogen, i.e. a temperature comparable to reaction conditions. As also discussed in Chapter 3, such pre-conditioning leads in both samples to a slight decrease in BET surface area and slight increase in M1 content and overall crystallinity compared to 80 °C drying overnight. This increase in crystallinity now allows to perform Rietveld analysis also on the B-M1 samples. The content of M1 phase determined by Rietveld analysis is similar for both samples (Q-M1: 79 wt.-%, B-M1: 73 wt.-%). Both samples contain additional amounts of X-ray amorphous material. In case of the B-M1 sample, broad and non-well-defined M1 reflections in the X-ray diffractogram indicate that the material mostly contains relatively short range ordered M1 domains. No other crystalline phases were found. Regarding the Q-M1 sample, in addition to crystalline M1 phase and amorphous material, traces of crystalline MoO_3 (< 3 wt.-%) were also detected.

The bulk elemental composition of both samples agrees well with their nominal composition (i.e. the ratio of metals used in hydrothermal synthesis).
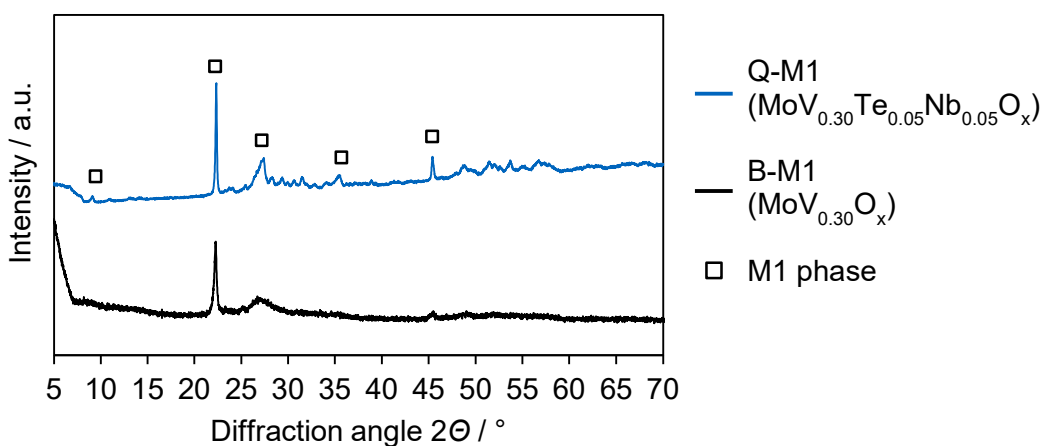
Figure 40: X-ray diffractograms of Q-M1 (blue) and B-M1 (black) samples after pre-conditioning to 400 °C in flowing nitrogen.

Table 6: Physico-chemical properties of Q-M1 and B-M1 samples after pre-conditioning to 400 °C in flowing nitrogen.

Sample	ICP-OES (in brackets: nominal) formula	BET / $m^2 g^{-1}$	M1 / wt.-%	Amorphous / wt.-%	Other phases
Q-M1	$MoV_{0.30}Te_{0.05}Nb_{0.05}O_x$ $(MoV_{0.30}Te_{0.05}Nb_{0.05}O_x)$	50	79	18	MoO_3
B-M1	$MoV_{0.30}O_x$ $(MoV_{0.30}O_x)$	63	73	27	none

Figure 41 shows typical scanning electron micrographs of both mixed metal oxides. Q-M1 crystallizes as well-defined rod-like particles, which is characteristic for anisotropic growth along the *c*-axis of M1 crystals [115]. On the other hand, B-M1 particles are smaller and have a lower aspect ratio, agreeing with the lower degree of crystal ordering observed in XRD.
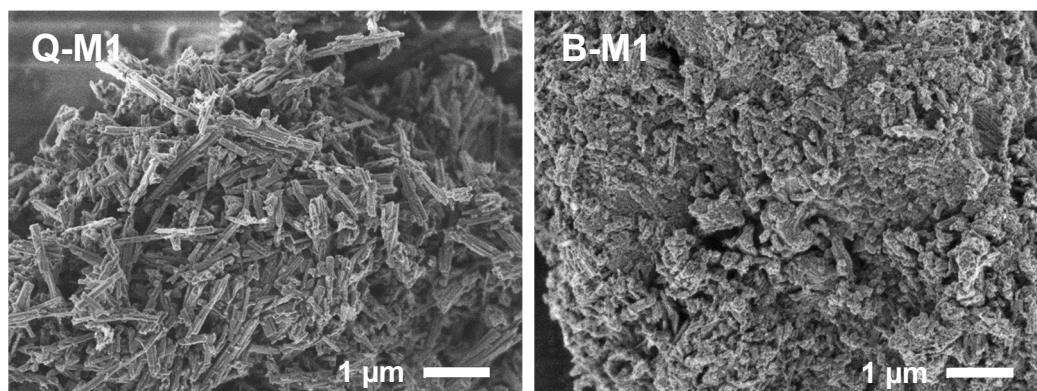
Figure 41: SEM images of Q-M1 ($MoV_{0.30}Te_{0.05}Nb_{0.05}O_x$, left) and B-M1 ($MoV_{0.30}O_x$, right) samples.

Chemical composition of surface layers as well as corresponding oxidation states of metal cations were derived from X-ray photoelectron spectra. The inelastic mean free path (IMFP), and hence information depth of escaping photoelectrons, was calculated using the algorithm by Penn *et al.* [204]. The IMFP is 1.8 nm (V) and 2.4 nm (Mo) using MoO_3 as model compound for M1, in accordance with Heine *et al.* [158]. To put these numbers into perspective, these lengths are equivalent to about one M1 unit cell measured along the *a* or *b* axes and five unit cells along the *c* axis. Experimental spectra and peak deconvolution are shown in Figure 42. Surface concentrations of metal species calculated from XPS intensities and their corresponding oxidation states are compiled in Table 7.
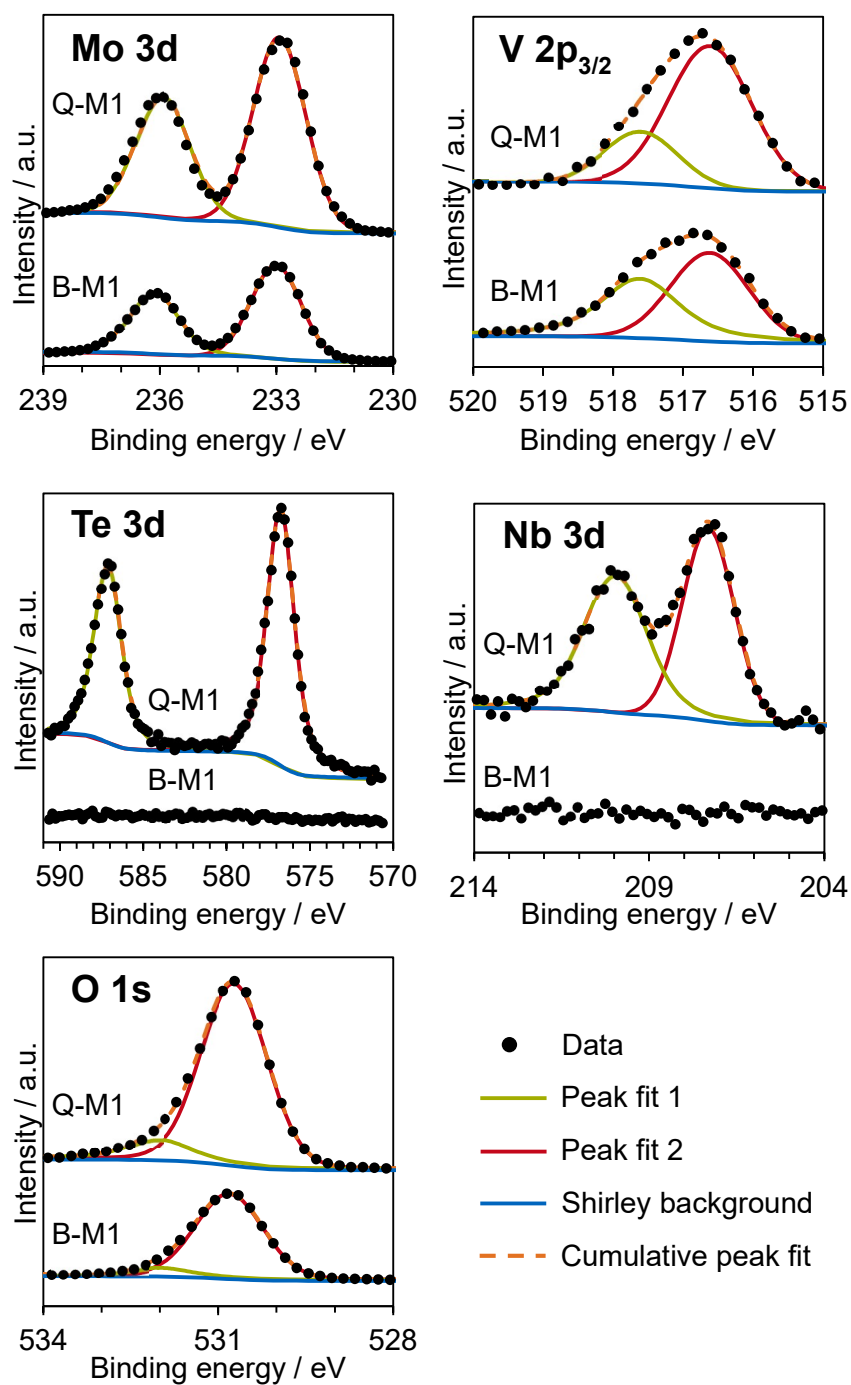
Figure 42: XPS core level spectra of Q-M1 (top) and B-M1 (bottom) samples.

Table 7: Near surface metal concentrations of $MoVTeNbO_x$ and $MoVO_x$ samples as determined by XPS.

Orbital	Binding energy / eV	Assignment	Q-M1 Concentration (brackets: rel. to Mo) / at.-%	B-M1 Concentration (brackets: rel. to Mo) / at.-%
Mo $3d_{5/2}$	232.9 (Q-M1) 233.0 (B-M1)	Mo^{6+}	23 (1.0)	24 (1.0)
V $2p_{3/2}$	517.6	V^{5+}	0.59 (0.02)	1.9 (0.08)
	516.6	V^{4+}	1.8 (0.08)	2.4 (0.09)
Te $3d_{5/2}$	576.7	Te^{4+}	1.0 (0.04)	0
Nb $3d_{5/2}$	207.3	Nb^{5+}	0.23 (0.01)	0
O 1s	530.8	$M-O_x$	64 (2.8)	66 (2.8)
	532.0	M-OH	8.2 (0.35)	6.6 (0.28)

Although there is a small shift to lower electron binding energies of Mo $3d_{5/2}$ electrons in the Q-M1 sample compared to B-M1, binding energies values of close to 233 eV in M1 [98,205] and molybdenum oxides [206,207] can solely be attributed to Mo^{6+} species. V $2p_{3/2}$ peaks show two contributions with binding energies at 516.6 eV and 517.6 eV, attributed to V^{4+} and V^{5+} species, respectively [121,205,208,209]. Presence of V in M1 phase with mixed oxidation state is commonly known [72,73,78]. Interestingly, the V^{5+}/V^{4+} ratio is close to unity in B-M1, while there is about four times more V^{4+} than V^{5+} in the surface layers of Q-M1, in good agreement with previous reports on M1 catalysts [210]. Binding energies of Te $3d_{5/2}$ (576.7 eV) and Nb $3d_{5/2}$ (207.3 eV) core levels in Q-M1 fit best to Te^{4+} [121,211] and Nb^{5+} [212,213] oxidation states. Peak deconvolution of O 1s core level spectra shows contributions from two species centered at 530.8 eV and 532.0 eV, corresponding to lattice O^{2-} and metal hydroxyl species, respectively [214].

While partial occupation of hexagonal channel sites (S12 in Figure 4 in Chapter 1) with Te in $M1-MoVTeNbO_x$ is well-known [77], recent STEM [203] and single crystal XRD [215] studies proposed that those sites in $M1-MoVO_x$ can be partially occupied by V^{5+} cations. Therefore, the higher V^{5+}/Mo ratio in surface found for sample B-M1 is tentatively attributed to the presence of V near the surface opening of hexagonal channels.

4.4 Kinetic investigations and reaction pathway analysis

Having established the crystalline phase composition and metal surface oxidation states, we now aim to gain further insight into the kinetics of ethane oxidation. Figure 43 shows the selectivities to ethene, carbon oxides and acetic acid as function of ethane conversion obtained over both catalysts.
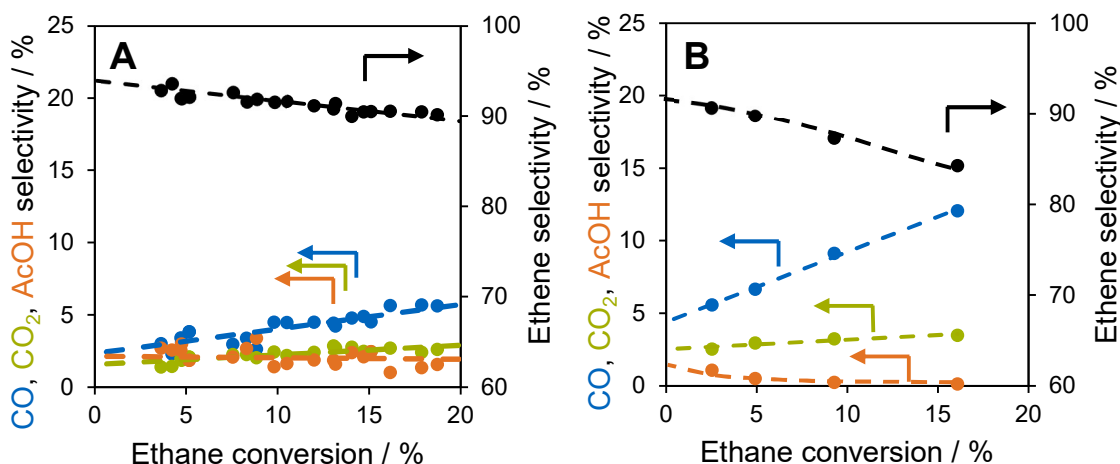

Figure 43: Ethane oxidation product selectivities obtained over Q-M1 (A) and B-M1 (B). Reactions conditions applied: T = 290 – 370 °C (Q-M1), 330 – 420 °C (B-M1), $C_2H_6:O_2:He$ = 3-9:3-9:82-94 (Q-M1), 9:9:82 (B-M1), p = 1.5 – 4.0 bar(a) (Q-M1), 1.0 bar(a) (B-M1), $WHSV$ = 4.8 – 19.0 h^{-1} (Q-M1), 4.8 h^{-1} (B-M1).

The zero-conversion level selectivities are similar for both catalysts, indicating that the initial activation of the ethane molecule follows the same reaction mechanism over both catalysts. At ethane conversion levels exceeding 5 %, selectivities begin to significantly diverge from each other. Ethene is the preferred reaction product over the whole conversion range tested, although selectivity is generally lower on B-M1 than Q-M1. The selectivity to CO in the 5-20 % conversion range is higher on B-M1 at the expense of ethene and acetic acid. The selectivity towards CO_2 is similar on both tested catalysts. We therefore hypothesize that ethene, CO, and acetic acid form via competing pathways directly from ethane. The ratio of rates of the competing reactions taking place, and hence the selectivity to products, depend on the M1 phase composition.

In order to support this hypothesis, next the rank of product formation, i.e. primary vs. higher rank products, was established by applying the Delplot analysis method [216,217]. Figure 44 shows first (A, C) and second (B, D) rank Delplots for both catalysts and all

reaction products. Finite axis intercepts in first rank Delplots (i.e. selectivity-conversion trajectories) and convex bending curves in second rank Delplots (S_i vs X^2_{C2H6}) for all products imply that ethene as well as carbon oxides and acetic acid are formed -at least in fractions- via direct pathways without the desorption of any gaseous intermediates. The fact that ethene, CO and acetic acid can form from ethane without de- and re-adsorption of gas phase intermediates agrees with our hypothesis of direct pathways from ethane to all three products.
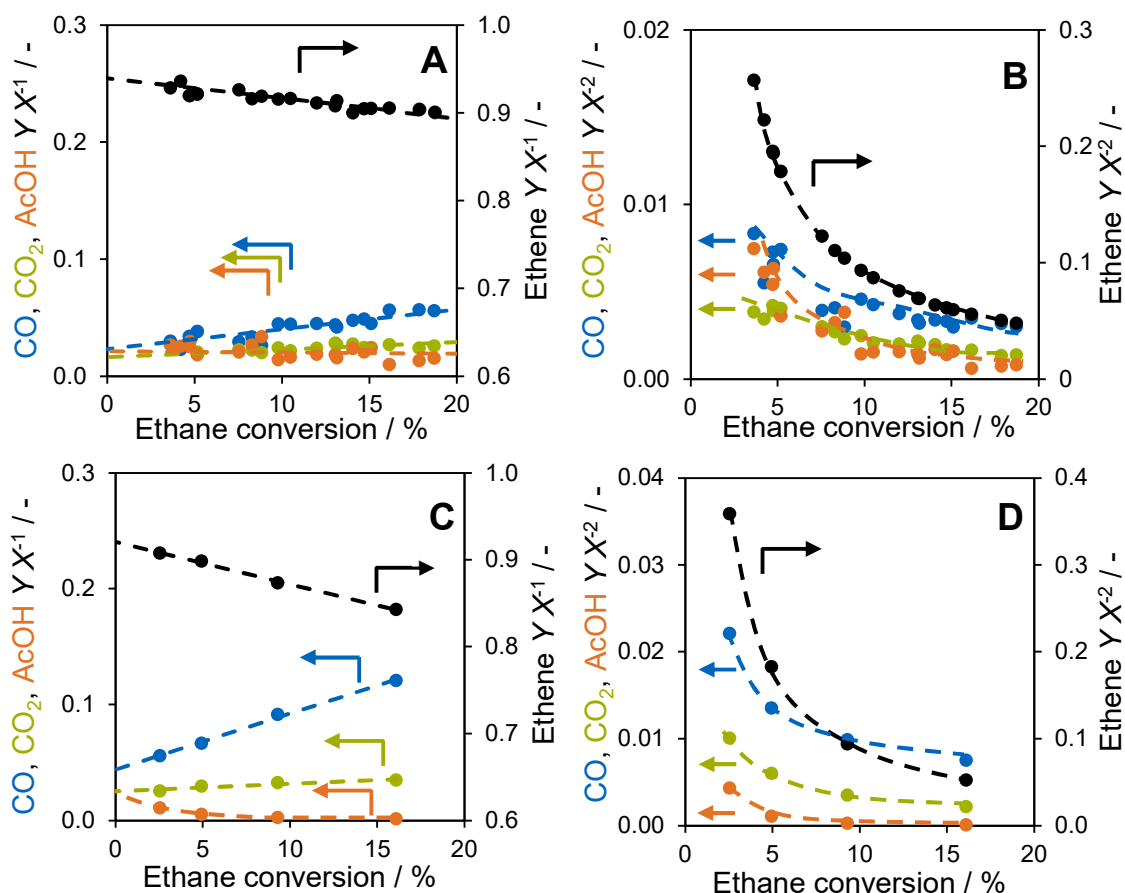
Figure 44: First (left) and second (right) rank Delplots for ethane oxidation over Q-M1 (A, B) and B-M1 (C, D) samples. Reactions conditions applied: T = 290 – 370 °C (Q-M1), 330 – 420 °C (B-M1), C_2H_6:O_2:He = 3-9:3-9:82-94 (Q-M1), 9:9:82 (B-M1), p = 1.5 – 4.0 bar(a) (Q-M1), 1.0 bar(a) (B-M1), $WHSV$ = 4.8 – 19.0 h^{-1} (Q-M1), 4.8 h^{-1} (B-M1).

Energies of activation for the different oxidation products of ethane were determined in the range of 330 – 420 °C and at differential conversion levels. Figure 45 shows Arrhenius type plots of the formation rates of ethene, CO_x and acetic acid.
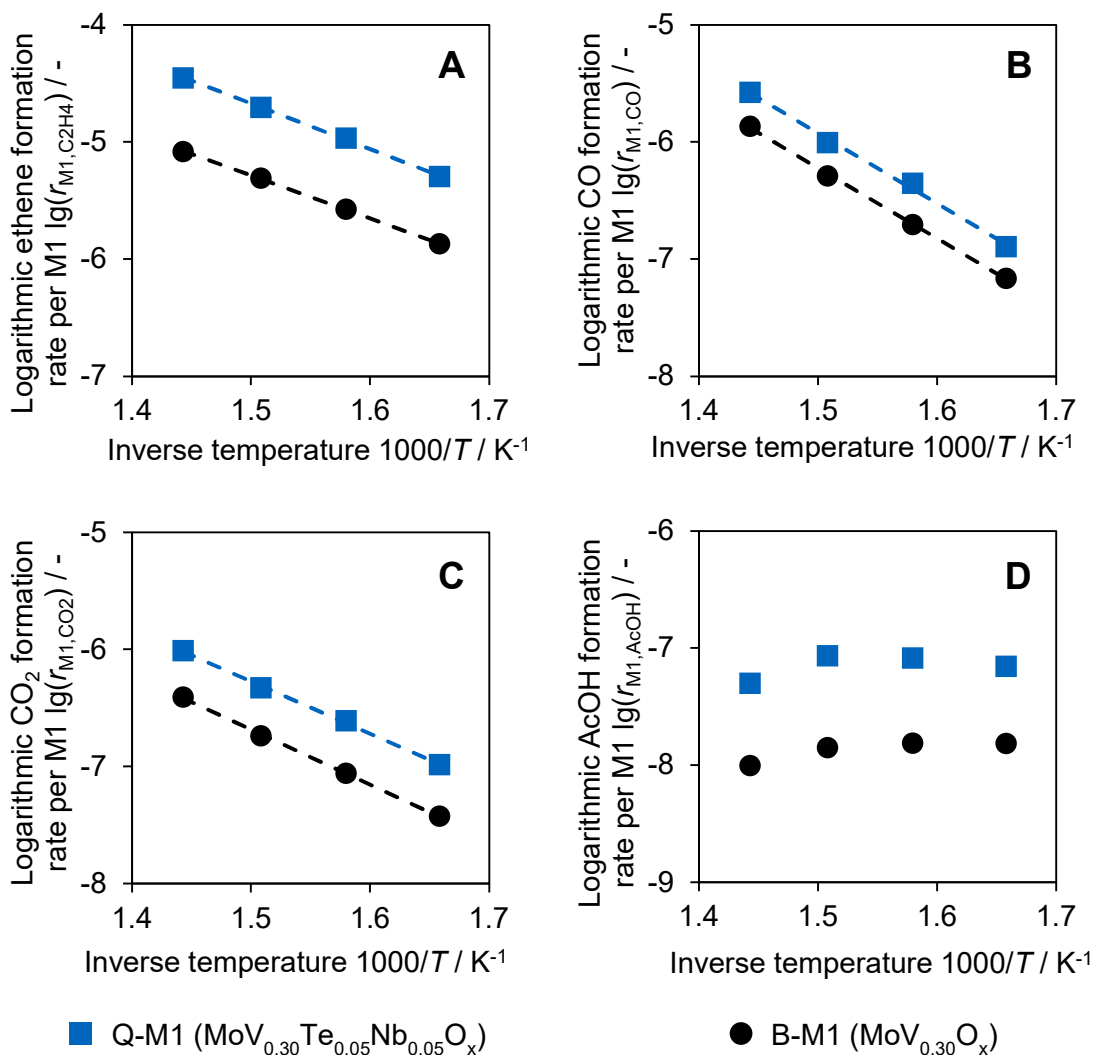
Figure 45: Ethene (A), CO (B), CO_2 (C) and acetic acid (D) formation rates in ethane oxidation over Q-M1 (blue squares) and B-M1 (black circles) normalized to weight of M1 phase. Reactions conditions applied: T = 330 – 420 °C, C_2H_6:O_2:He = 9:9:82, p = 1 bar(a), $WHSV$ = 17.4 h^{-1} (Q-M1), 4.8 h^{-1} (B-M1).

Under reaction conditions resulting in differential conversion, all products are formed with a higher rate (normalized per M1 phase content, Table 6) over Q-M1 compared to B-M1. This observation holds also true for normalization to mass of catalyst used, BET surface area as determined by N_2 adsorption (Table 6), and combination of BET area and M1 phase content (exemplary shown for ethene formation rates in Figure 46). In addition, it needs to be noted that rates over B-M1 are lower than on Q-M1, despite the higher V^{5+}/Mo fraction in B-M1. We speculate that V^{5+} in the channels in B-M1 does not contribute to an increase in the rates. Another possible explanation is a lower

concentration of active sites in M1, due to the high disorder and defects in B-M1, as indicated by the broad diffraction lines in XRD.
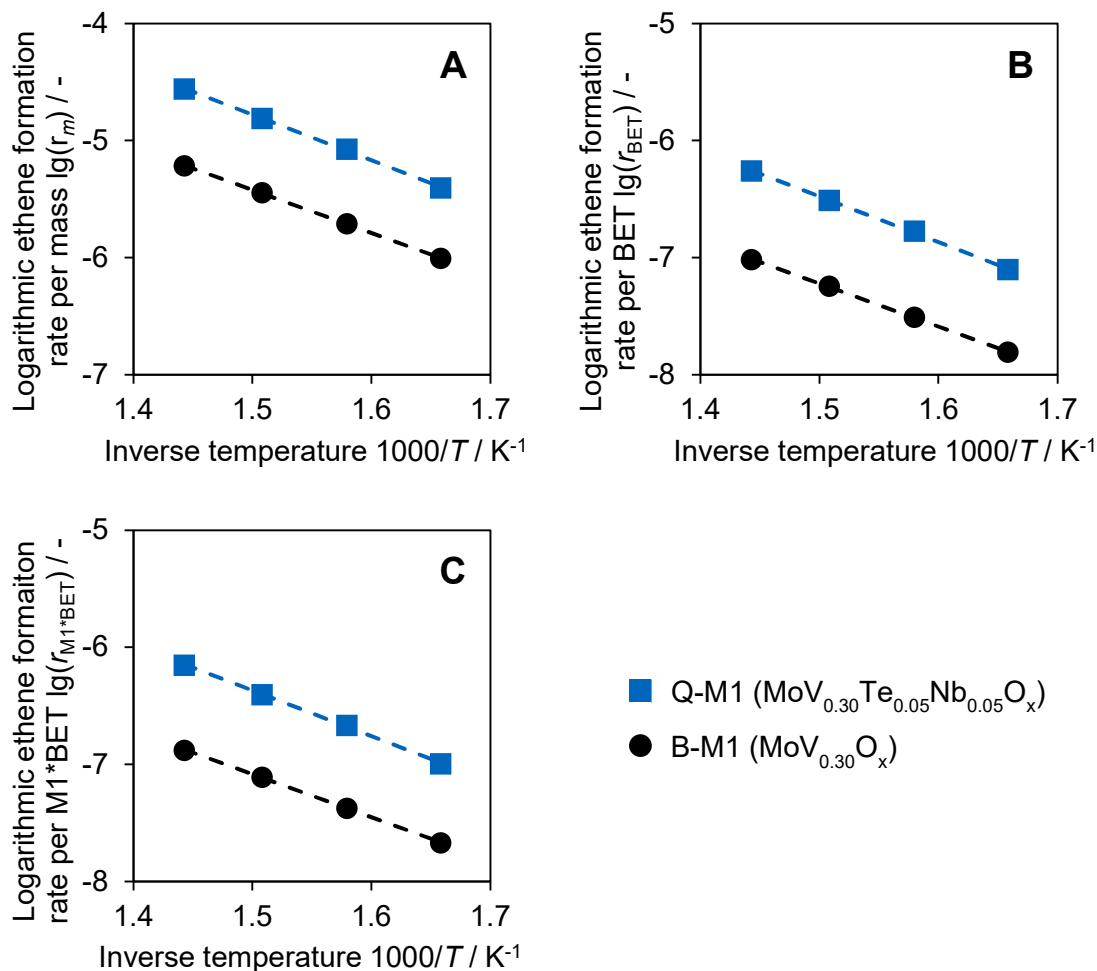
Figure 46: Ethene formation rates in ethane oxidation over Q-M1 (blue squares) and B-M1 (black circles) normalized to mass of catalyst (A), overall surface area (B) and surface area of M1 phase (C). Reactions conditions applied: T = 330 – 420 °C, $C_2H_6:O_2:He$ = 9:9:82, p = 1 bar(a), $WHSV$ = 17.4 h^{-1} (Q-M1), 4.8 h^{-1} (B-M1).

Virtually parallel lines in the Arrhenius plots in Figure 45 indicate that the two catalysts studied have identical apparent activation energies for each of the reaction pathways of ethane oxidation. The apparent activation energy obtained for ethene formation shows that this pathway has the smallest barrier, ca. 76 ± 1.2 kJ mol^{-1}, followed by CO_2 (91 ± 3.4 kJ mol^{-1}) and CO formation (120 ± 6.0 kJ mol^{-1}). The different activation energies for the three main reaction products ethene, CO and CO_2 imply that the rate

determining step is different for each of the three products, but similar over both catalysts.

Due to bending lines in the Arrhenius plot of acetic acid formation it was not possible to measure an energetic barrier. Possible reasons for this kinetic behavior include transport limitation effects or equilibration of acetic acid precursor species on the surface of the catalysts.

Results of ethane oxidation kinetic tests do not clarify the differences in selectivities observed at higher ethane conversion levels. However, the results point towards a direct formation of a fraction of carbon oxides and acetic acid from ethane. Yet, another fraction of these side products may also be formed by oxidation of ethene. In the next step, we therefore studied the kinetics of ethene oxidation over the catalysts to check for possible additional reaction pathways.

Figure 47 shows the selectivities as function of conversion for the reaction of ethene oxidation over Q-M1 and B-M1 catalysts. Carbon oxides and acetic acid were the only observed products. Finite axis intercepts in X-S projections indicate that there are direct reaction pathways for the formation of both carbon oxides and acetic acid over the two catalysts. Over both catalysts, CO is the main reaction product with virtual constant selectivity of S_{CO} = 75 % at conversion levels exceeding 5 %. But, at conversion levels below ca. 15%, there are significant differences between both catalysts with respect to CO_2 and acetic acid selectivities. In Q-M1, the second most abundant product is CO_2 (initial selectivity ca. 25 %) and only small amounts of acetic acid are formed. This product distribution is constant up to 15 % conversion level. Over B-M1, acetic acid has an initial selectivity of about 20 % and CO_2 only has an initial selectivity of about 10 %. Despite those differences at low conversions, product selectivities over both catalysts converge when conversion levels over B-M1 are larger than 30%.
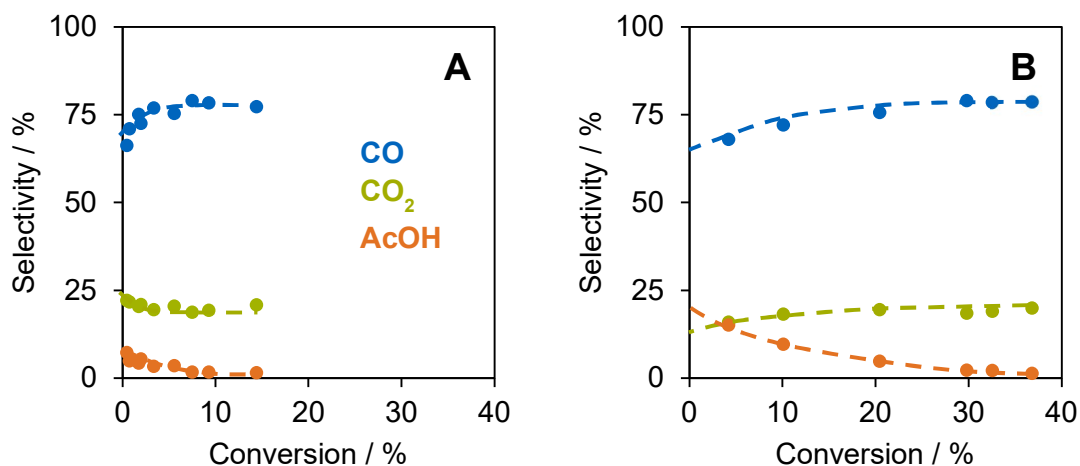
Figure 47: Ethene oxidation product selectivities obtained over Q-M1 (A) and B-M1 (B). Reactions conditions applied: T = 330 – 420 °C (Q-M1 and B-M1), C_2H_6:O_2:He = 3-9:3-9:82-94 (Q-M1), 9:9:82 (B-M1), p = 2.7 – 4.0 bar(a) (Q-M1 and B-M1), $WHSV$ = 16.9 – 19.3 h^{-1} (Q-M1), 4.8 h^{-1} (B-M1).

Activation energies of both samples for oxidation of ethene were determined by reactions under differential conversions in the temperature range of 330 – 420 °C. Arrhenius type plots of CO_x and acetic acid formation rates normalized to the weight of M1 phase are shown in Figure 48. Ethene oxidation occurs at similar rates (normalized to M1 content) over both catalysts in the temperature range of 330 – 420 °C, although with different selectivities. Contrary to ethane oxidation, there are pronounced differences in the energetic barriers to oxidize ethene over each catalyst (Table 8). Apparent E_As are 30 - 40 kJ mol^{-1} lower on B-M1 than on Q-M1 for both CO and CO_2. Apparent activation energy for acetic acid formation is zero, similar to ethane oxidation.

Similar energies of activation for CO formation and for CO_2 formation are obtained over each catalyst. This suggests that both products stem from a common pathway with the same rate determining step. The energetic barrier however is affected by the presence or absence of Te and Nb. The higher barriers for ethene oxidation compared to those for ethane (Table 8) measured on the Q-M1 catalyst agree well with the observed high selectivity to ethene over this material.
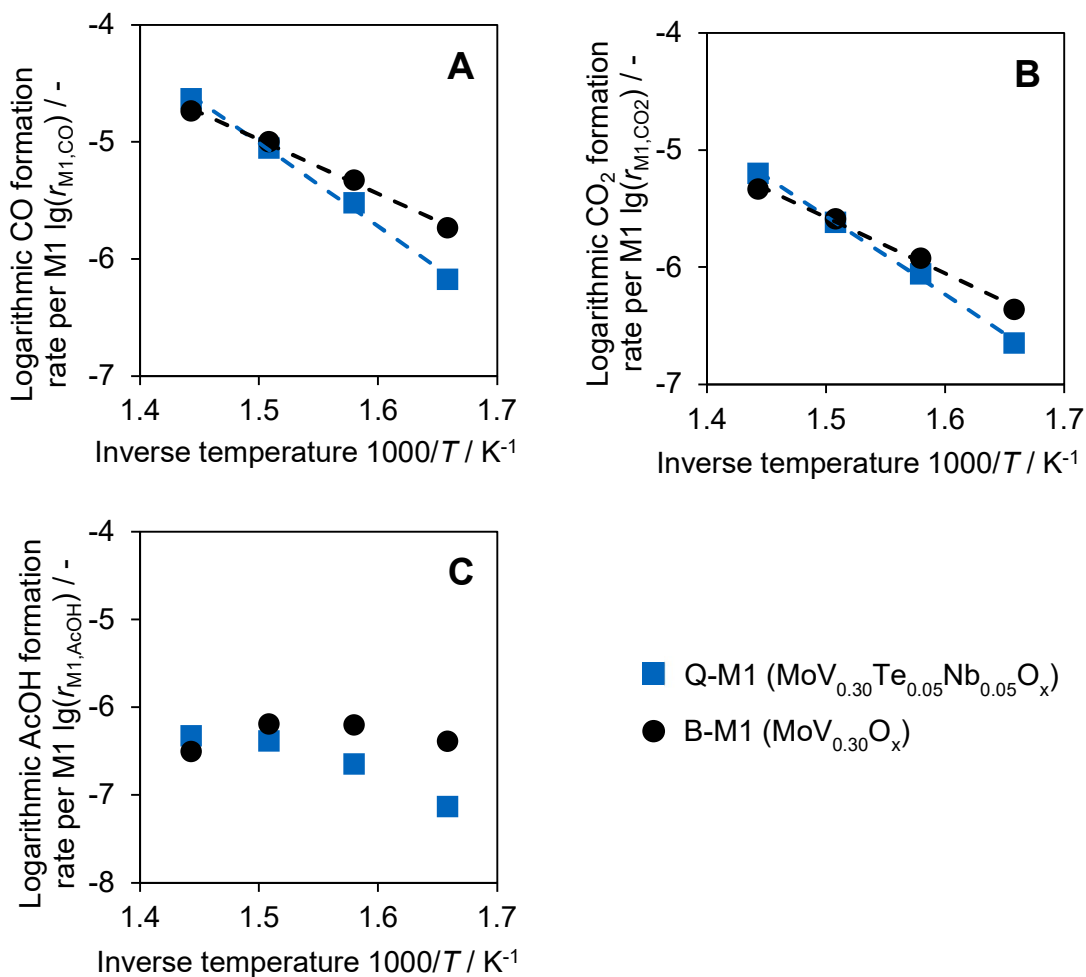
Figure 48: CO (A), CO_2 (B) and acetic acid (C) formation rates in ethene oxidation over Q-M1 (blue squares) and B-M1 (black circles) normalized to weight of M1 phase. T = 330 – 420 °C, $C_2H_6:O_2:He$ = 9:9:82, p = 4 bar(a), $WHSV$ = 17.1 h^{-1} (Q-M1), 4.8 h^{-1} (B-M1).

Table 8: Apparent activation energies E_A and corresponding standard deviation for all product formation pathways from ethane and ethene. Values are given in kJ mol^{-1}.

Feed	Q-M1		B-M1	
Product	Ethane	Ethene	Ethane	Ethene
Ethene	78 ± 1.2	N/A	74 ± 0.19	N/A
CO	120 ± 5.4	140 ± 5.6	120 ± 2.7	100 ± 1.6
CO_2	89 ± 2.7	130 ± 3.6	93 ± 2.1	100 ± 3.1
AcOH	0	0	0	0

4.5   Discussion of reaction pathways

Based on the kinetic experiments of ethane and ethene oxidation, three reaction pathways can be distinguished:

A) *Oxidative dehydrogenation of ethane to ethene*

This is the main reaction pathway over both catalysts. Identical activation energies on Q-M1 and B-M1 show that both catalysts share the same rate determining step and thus it can be concluded that the reaction mechanism is similar for M1 catalysts without Te and Nb and those with concentrations of those elements lower than 0.10 relative to Mo. Our $MoV_{0.30}Te_{0.05}Nb_{0.05}O_x$ M1 phase formulation (Q-M1) is intrinsically more active than the binary $MoV_{0.30}O_x$-M1 counterpart (B-M1) in spite of their similar V content, based on the differences observed in their reaction rates after normalization to key parameters such as M1 content and BET area (see Figure 46). This higher activity can be attributed to a higher active site density, which may result from i) creation of additional oxygen radical sites by Te reduction under reaction conditions [190] or ii) a higher concentration of V in active sites of the M1 framework based on its higher crystallinity and a V^{4+}/V^{5+} ratio falling into the range typical for M1 [210].

B) *Direct total oxidation of ethane*

Direct formation pathways of CO and CO_2 from C_2H_6, without release of gas phase intermediates, can be identified based on Delplot analysis results. Similar to the selective ethane oxidation pathway, activation energies were found to be identical on the binary and quaternary M1 variants. Again, this fact implies that the mechanism of ethane total oxidation does not depend on the presence of Te and Nb in M1 crystal phase. However, different activation energies for CO and CO_2 formation evidence that these two products do not share the same rate determining step in their ethane oxidation mechanisms.

C) *Total oxidation of ethene*

There is also a direct pathway to CO_x in the total oxidation of ethene. Contrary to what was observed for the total oxidation of ethane, the barrier for ethene oxidation was found to be higher for the catalyst containing Te and Nb, which agrees well with the observed higher ODH selectivity to ethene on Q-M1. For each catalyst, the E_A for CO and CO_2 formation are close to identical. This implies an identical rate determining step for formation of both carbon oxides from ethene. However, the site

responsible for the reaction is likely different in each of the two catalysts. In the case of B-M1, the somewhat higher concentration of XRD amorphous material and lower degree of long-range crystal structuring indicates a higher probability of other structures acting as unselective centers being present in the catalyst. While these sites might not be able to activate ethane, the kinetic analysis clearly shows their ability of oxidize ethene to CO_x with a barrier of ca. 100 kJ mol^{-1}.

ODH-E, i.e. selective hydrogen abstraction, activity of M1 phase is commonly ascribed to oxygen radical sites located in the pentameric ensemble of crystallographic sites S2-S4-S7 [75,135,141,142]. A recent DFT study examined the position of the active site for oxidative dehydrogenation in M1-MoVO$_x$ on the {001} crystalline plane [218]. In agreement with earlier proposals [219,220], bridging lattice oxygen sites connecting S4 and S7 metal framework sites were found to be the energetically most favored site for ODH-E.

Based on the kinetic results it can be assumed that at least two types of active species must be present on the surface of the M1-MoVO$_x$ catalyst: One selectively abstracting hydrogen from ethane and at least another one attacking the carbon-carbon bonds of ethane and ethene. CO/CO$_2$ ratios at differential hydrocarbon conversion are identical for B-M1 and Q-M1 catalysts but different for ethane (CO/CO$_2 \approx 2$) and ethene (CO/CO$_2 \approx 4$) oxidation. This points to different mechanistic origin of the carbon oxides formed in ethane and ethene total oxidation. The E_A calculated for ethane direct oxidation to CO_x is similar for quaternary and binary M1 catalysts, thus we conclude that this pathway, similar to ethane ODH pathway, is not affected by the presence of Te and Nb. Contrary, formation of a highly disordered MoV-M1 catalyst generates sites with lower barrier for total oxidation of ethene, thus leading to a poor selectivity in the overall ethane ODH reaction on this catalyst. Therefore, although the nature of the species responsible for the direct oxidation of ethane (pathway B) and ethene (pathway C) is unknown, it can be concluded that there are likely different active sites for total oxidation in B-M1 and Q-M1.

The kinetic behavior of acetic acid formation does not allow to draw conclusions on its formation pathways. However, some information is available on the pathways of its decomposition. Acetic acid total oxidation over MoVTeNbO$_x$ (mixture of M1 and M2 phases) has been reported to lead to identical concentrations of CO and CO$_2$ [132]. The fact that the ratio of carbon oxides on Q-M1 and B-M1 is much larger than 1 suggests that decomposition of adsorbed acetic acid (or its surface precursor) is not the only route

for formation of CO_x in ethane and ethene oxidation. This is in line with the finding that ethane and ethene total oxidation follow different reaction mechanisms to CO_x.

4.6   Conclusions

The presence of Te and Nb in M1-type catalysts affects reaction rates as well as product distribution in oxidative dehydrogenation of ethane. Presence of small concentrations of Te and Nb increase alkane activation rates by up to almost one order of magnitude compared to M1 phase containing only Mo and V. Catalysts with identical or excess amounts of Nb with respect to Te show highest selectivity to ethene. The high olefin selectivity of $MoVTeNbO_x$ compared to $MoVO_x$ results from higher energetic barriers for total oxidation of ethene. The differences in alkane and olefin oxidation rates are explained by a different ratio of selective to unselective sites.

4.7   Associated content and contributions

Part of the content of this chapter is based on the manuscript *On the promoting effects of Te and Nb in the activity and selectivity of M1 MoV-oxides for ethane oxidative dehydrogenation* submitted to Topics in Catalysis. The structure and content of this chapter differs from the manuscript. The synthesis protocol of the metal oxide catalysts was patented (see Chapter 13 of this work and references [191-193]).

Daniel Melzer performed the syntheses, physico-chemical analyses and kinetic tests of the mixed metal oxide catalysts, evaluated the data and prepared the manuscript. Philipp J. Donaubauer participated in computing selected kinetic reaction data. Takaaki Ikuno performed SEM imaging. XPS experiments and elemental quantification were performed by Physical Electronics GmbH, Ismaning, Germany. Dr. Gerhard Mestl and Dr. Klaus Wanninger advised the research. Dr. Maricruz Sanchez-Sanchez is the project leader and Prof. Dr. Johannes A. Lercher is the principal investigator of this project. They both supervised the research and discussed results and conclusions.

5 Summary and conclusion

In this dissertation, the effects of synthesis method and metal stoichiometry on the catalytic performance and stability of MoV(TeNb) mixed metal oxides for the oxidative dehydrogenation of ethane (ODH-E) were investigated.

In the first part of this work (Chapter 2), a new method for hydrothermal synthesis of $MoV(TeNb)O_x$ was established. Starting from aqueous suspensions of corresponding abundant single metal oxides combined with chelating additives it was possible to generate mixed metal oxide precursors with a metal stoichiometry in the range of $MoV_{0.22-0.30}Te_{0-0.18}Nb_{0-0.18}O_x$. Crystallization of the amorphous precursors to the catalytically active M1 crystal phase was possible for all quaternary metal combinations upon annealing in inert atmosphere at 650 °C. XRD and Rietveld analysis confirmed M1 phase yields up to about 75 wt.-%. However, secondary metal oxide phases were formed along with M1 phase. Adjustment of the chemical potential in the synthesis slurry by tuning metal stoichiometry to $MoV_{0.30}Te_{0-0.10}Nb_{0-0.10}$ and oxalic acid/Nb ratio of 1 allowed to precipitate crystalline M1 phase under hydrothermal conditions at 190 °C and autogenous pressure. Contrary to crystallization at 650 °C, at these conditions only trace amounts of secondary crystalline phases were formed. M1 phase crystallized at such low temperature gives significantly higher ODH-E rates compared to materials crystallized at high temperatures. Rates were found to increase with V content, agreeing with earlier proposals of vanadyl (V^{5+}) surface species, being the active sites. It was also found that small amounts of Te (Te/Mo = 0.05) lead to the highest rates for a given V content.

In the second part (Chapter 3), the chemical processes during M1 crystallization under hydrothermal conditions were studied in order to link M1 crystal properties to the high catalytic activity of materials prepared under such conditions. For this purpose, M1 crystal formation according to the procedure developed in chapter 2 of this thesis was compared to a literature reported method, in which crystallization takes place at more than 400 °C higher temperature. It was shown that the high activity of the low-temperature-crystallized samples is not only due to a higher surface area, but also to a higher density of active sites per m^2 of M1 phase. ADF-STEM images of M1-$MoVTeNbO_x$ synthesized by the new method showed highly corrugated crystal terminating surfaces. Conversely, M1 phase crystallized at 650 °C showed smooth surfaces preferentially terminated by thermodynamically stable M_6O_{21} units. It is concluded that the higher active site density of low-temperature crystallized M1 phase results from incomplete saturation

of growth sites, i.e. particle termination surfaces not having reached their thermodynamically most stable configuration. This is supported by the observation of a decrease in intrinsic catalytic activity with prolonged synthesis duration, which is attributed to reorganization of the crystal termination. Controlling the concentration of polyoxometalate clusters, acting as building block donors, near a threshold level for precipitation of solid material was identified as key to *in-situ* crystallization during hydrothermal synthesis.

In the third part of this thesis (Chapter 4), effects of metal stoichiometry on the activity and selectivity of M1-type catalysts in ODH-E were investigated. For this purpose, the ODH-E performance of a series of catalysts with $MoV_{0.30}Te_{0-0.10}Nb_{0-0.10}O_x$ stoichiometry was evaluated. It was found that presence of small amounts of Te and Nb (Te/Mo = Nb/Mo = 0.05) are both beneficial to high rates and high ethene selectivity. In contrast, a catalyst with identical V/Mo ratio, but not containing any Te or Nb ($MoV_{0.30}O_x$), showed lower activity and ethene selectivity compared to the quaternary samples, in spite of a similar M1 content and even higher V^{5+} concentration. Detailed kinetic studies on $MoV_{0.30}Te_{0.05}Nb_{0.05}O_x$ and $MoV_{0.30}O_x$ revealed the reason for the comparatively poor selectivity over $MoVO_x$: ethane selective oxidation rates over $MoVTeNbO_x$ are about one order of magnitude higher than on $MoVO_x$, with corresponding activation energies being identical. Conversely, rates of ethene total oxidation are similar on both catalysts, but the energetic barriers for undesired total oxidation are 30 – 40 kJ mol^{-1} lower on $MoVO_x$ than on $MoVTeNbO_x$. Three pathways in oxidation of ethane can be distinguished: selective partial oxidation of ethane to ethene (ODH-E), direct total oxidation of ethane to CO_x, and total oxidation of ethene to CO_x. Mechanistic considerations lead us to propose at least two different types of active sites: On the one hand a site catalyzing the first hydrogen abstraction from the alkane leading to the desired olefin product. This type of site is identical on $MoVTeNbO_x$ and $MoVO_x$. And on the other hand, there are sites catalyzing oxygen insertion in C-C single and double bonds, resulting in total oxidation of the hydrocarbon. Differences in energetic barriers for total oxidation of ethane and ethene found over $MoVTeNbO_x$ and $MoVO_x$ imply that their nature is different on both types of catalysts.

6 Zusammenfassung und Schlussfolgerung

Im Rahmen dieser Dissertation wurden die Auswirkungen des Syntheseweges und der Metallstöchiometrie auf die katalytische Leistungsfähigkeit und die Stabilität von MoV(TeNb)-Mischoxiden in der oxidativen Dehydrierung von Ethan (*oxidative dehydrogenation of ethane*, ODH-E) untersucht.

Im ersten Teil dieser Arbeit (Kapitel 2) wurde eine neue Vorschrift für die hydrothermale Synthese von MoV(TeNb)O_x entwickelt. Ausgehend von einer wässrigen Suspension der entsprechenden einzelnen Metalloxide zusammen mit Chelatbildnern war es möglich Mischoxidvorstufen mit einer Metallzusammensetzung von MoV$_{0.22-0.30}$Te$_{0-0.18}$Nb$_{0-0.18}$O$_x$ zu erzeugen. Es gelang durch thermische Behandlung in inerter Atmosphäre bei 650 °C alle quaternären amorphen Vorstufen zur katalytisch aktiven M1-Phase zu kristallisieren. Röntgenbeugungs- und Rietveld-Analyse bestätigten Ausbeuten an M1-Phase von bis zu etwa 75 Gew.-%. Jedoch bildeten sich neben der M1-Phase weitere sekundäre Metalloxidphasen. Eine Anpassung des chemischen Potentials in der Synthesesuspension durch Änderung der Metallstöchiometrie zu MoV$_{0.30}$Te$_{0-0.10}$Nb$_{0-0.10}$ und Einstellung des Oxalsäure/Nb-Verhältnisses auf 1/1 führte zum Ausfallen der M1-Kristallphase unter hydrothermalen Bedingungen bei 190 °C und autogenem Druck. Im Gegensatz zur Kristallisation bei 650 °C wurden bei diesen Bedingungen nur Spuren anderer (Misch)metalloxidphasen gebildet. M1-Phase, welche unter solch niedrigen Temperaturen kristallisierte, katalysiert die ODH-E mit erheblich höheren Raten als solche, die bei hoher Temperatur kristallisiert wurde. Es konnte gezeigt werden, dass die Raten mit dem Gehalt an V ansteigen. Dies stimmt mit früheren Berichten überein, welche Vanadyl (V^{5+})-Oberflächenspezies als aktives Zentrum vorschlagen. Darüber hinaus führen kleine Mengen an Te (Te/Mo = 0.05) zu den höchsten Raten bei vorgegebener Vanadiumkonzentration.

Im zweiten Teil (Kapitel 3) wurden die chemischen Prozesse, die bei der Kristallisation der M1-Phase unter hydrothermalen Bedingungen ablaufen, untersucht, um eine Korrelation zwischen der hohen katalytischen Aktivität und den Eigenschaften der M1-Kristalle aufzustellen. Dafür wird die Kristallbildung ausgehend von der in Kapitel 2 vorgestellten Methode mit einer in der Literatur beschriebenen Synthese verglichen, bei der zur Kristallisation eine mehr als 400 °C höhere Temperatur nötig ist. Es konnte gezeigt werden, dass die hohe katalytische Aktivität des bei niedriger Temperatur kristallisierten Mischoxides nicht nur aus einer größeren Oberfläche, sondern zusätzlich auch aus einer höheren Dichte an aktiven Zentren pro m² M1-Phase, resultiert. In ADF-

STEM-Bildern ist zu sehen, dass die gemäß neuer Vorschrift synthetisierten M1-MoVTeNbO$_x$-Kristalle eine deutlich geriffelte Oberflächenstruktur aufweisen. Im Gegensatz dazu hat M1-Phase, die bei 650 °C kristallisiert wurde, glatte Oberflächen, die bevorzugt an thermodynamisch stabilen M$_6$O$_{21}$-Einheiten abschließen. Daraus kann geschlossen werden, dass die höhere Dichte an aktiven Zentren der niedertemperatur-kristallisierten M1-Phase aus der unvollständigen Absättigung von Kristallwachstumsstellen resultiert. In anderen Worten ausgedrückt: Die niedertemperatur-kristallisierten M1-Kristalle haben ihre thermodynamisch stabilste Oberflächenkonfiguration noch nicht erreicht. Diese Schlussfolgerung wird weiterhin durch eine mit zunehmender Synthesedauer abnehmende intrinsische katalytische Aktivität belegt. Dieser Aktivitätsverlust wird mit einer Reorganisation der abschließenden Kristalloberflächen erklärt. Entscheidend für die *in-situ* Kristallisation während der Hydrothermalsynthese ist das Einstellen der Konzentration an Polyoxometalatclustern nahe der Grenze zum Ausfallen von Feststoff. Solche Cluster dienen dabei als Donoren von Kristallbausteinen.

Im dritten Teil dieser Arbeit (Kapitel 4) wurden die Effekte der Metallstöchiometrie auf die Aktivität und Selektivität von M1-Katalysatoren in der ODH-E untersucht. Dazu wurde die katalytische Leistung einer Serie von Katalysatoren mit der Zusammensetzung MoV$_{0.30}$Te$_{0-0.10}$Nb$_{0-0.10}$O$_x$ getestet. Es stellte sich heraus, dass kleine Mengen an Te und Nb (Te/Mo = Nb/Mo = 0.05) sowohl die Umsatzraten als auch die Selektivität zu Ethen erhöhen. Der Katalysator mit identischem V/Mo-Verhältnis, der jedoch kein Te und Nb enthält, (MoV$_{0.30}$O$_x$) zeigt niedrigere Aktivität und Selektivität im Vergleich zu den quaternären Proben. Dies gilt unabhängig von einem ähnlichen M1-Phasenanteil und sogar höherer V^{5+}-Konzentration. Aus detaillierten kinetischen Untersuchungen von MoV$_{0.30}$Te$_{0.05}$Nb$_{0.05}$O$_x$ und MoV$_{0.30}$O$_x$ ergab sich die Ursache für verhältnismäßig niedrige Ethenselektivität über MoVO$_x$: Die Raten der selektiven Oxidation von Ethan sind, bei vergleichbaren Aktivierungsenergien, über MoVTeNbO$_x$ etwa eine Größenordnung höher als über MoVO$_x$. Im Gegensatz dazu sind jedoch die Raten der Totaloxidation von Ethen über beiden Katalysatoren ähnlich und die energetische Barriere für die ungewollte Totaloxidation über MoVO$_x$ sogar 30 – 40 kJ mol^{-1} niedriger als über MoVTeNbO$_x$. Es kann zwischen drei Reaktionswegen in der Oxidation von Ethan unterschieden werden: die selektive Teiloxidation von Ethan zu Ethen (ODH-E), die direkte Totaloxidation von Ethan zu CO$_x$ und die Totaloxidation von Ethen zu CO$_x$. Auf Basis von mechanistischen Überlegungen schlagen wir mindestens zwei verschiedene Arten von aktiven Zentren vor: Einerseits Zentren, die die erste Abspaltung von Wasserstoff vom Kohlenwasserstoff, und damit die Bildung des Olefins, katalysieren.

Andererseits Zentren, die die Insertierung von Sauerstoff in C-C-Einfach- und -Doppelbindungen katalysieren, woraus die Totaloxidation der Kohlenwasserstoffe folgt. Unterschiede zwischen den energetischen Barrieren für die Totaloxidation von Ethan und Ethen über $MoVTeNbO_x$ und $MoVO_x$ deuten darauf hin, dass es sich um unterschiedliche Arten von aktiven Zentren auf beiden Katalysatoren handelt.

7 Experimental procedures

This chapter summarizes all standard experimental methods and procedures. Deviation of the standard procedures are clearly marked in the respective chapters and explained in detail there.

7.1 New synthesis method

MoO_3 (Honeywell), V_2O_5 (Treibacher), TeO_2 (5N+), $Nb_2O_5 \cdot 1.5H_2O$ (Alfa Aesar), citric acid (CA), oxalic acid (OA) and mono ethylene glycol (EG) were mixed as an aqueous dispersion (millipore grade). All reactants were used as purchased without further purification. The concentration of Mo was fixed at 0.5 mol L^{-1}. Metal stoichiometry was varied in the range of Mo:V:Te:Nb = 1:0.22–0.30:0–0.18:0–0.18. Concentration of synthesis additives relative to Mo was varied in the range Mo:CA:OA:EG = 1:0.075:0–0.18:0.075. The ratio Nb:OA was fixed at 1:1. The aqueous dispersion was directly mixed in the synthesis autoclaves. Hydrothermal synthesis was performed in two different types of autoclaves: A) A Teflon lined stainless steel autoclave without controlled stirring, but attached to a rotating shaft, and heated in a muffle furnace (volume H_2O = 75 mL) and B) a Premex Reactor AG hpm-p stainless steel autoclave including a blade stirrer (volume H_2O = 200 mL) heated by an external thermostat (Lauda E4G). All syntheses were performed at 190 °C and autogeneous pressure of 17.5 bar(a) for 48 h except otherwise stated in the manuscript. The crude precipitates were separated from the synthesis liquor by filtration (2-3 μm) and washed with 2.5 times the volume of ultra-pure water used in the initial reaction mixture.

In some cases, aliquots (about 5 mL, < 10 mg solid) have been extracted from the autoclave and immediately quenched in order to analyze the evolution of the slurry with time during hydrothermal synthesis. The solid was separated from the liquor by filtration, washed with ca. 12 mL of Millipore grade water and dried at 80 °C in static air.

7.2   Standard synthesis from soluble reactants

5.33 mmol $(NH_4)_6Mo_7O_{24}\cdot4H_2O$ were dissolved in 30 mL of H_2O (Millipore grade) at 80 °C. Aqueous solutions of 14.92 mmol $VOSO_4$, 3.73 mmol $Te(OH)_6$ and 3.73 mmol $(NH_4)NbO(C_2O_4)_2$ (80 °C and 15 mL, each) were added stepwise to the ammonium heptamolybdate solution. The mixture was vigorously stirred for 10 min before being transferred to a teflon lined stainless steel autoclave. Hydrothermal synthesis was performed at 175 °C and autogenous pressure for 20 h. The precipitate was separated from the synthesis liquor by filtration (2-3 μm) and washed with 2.5 times the volume of ultra-pure water used in the initial reaction mixture.

7.3   Thermal treatment

All crude precipitated materials were dried in static air at 80 °C for 16 h after filtration (materials denoted as "as-synthesized" or "low-temperature crystallized"). Optionally, two different thermal treatments could be applied to dried Mo-V-Te-Nb mixed metal oxide. A) Preconditioning to reaction temperature at 400 °C in flowing N_2 with a heating ramp of 15 °C min^{-1} and dwell time of 2 h. (materials denoted as "preconditioned"). B) Two-step profile with heating to 200 °C at 15 °C min^{-1} in flow of synthetic air and 2 h dwell time followed by 30 min flushing with flow of N_2 and subsequent heating to 600 °C or 650 °C at 15 °C min^{-1} in flow of N_2 and dwell time of 2 h (materials denoted as "high-temperature crystallized").

7.4   X-ray diffraction analysis

All measurements of the powdered samples were performed on a PANalytical Empyrian or PANalytical X'pert Pro diffractometers built in a Bragg-Brentano geometry (θ-2θ-goniometer), using copper-Kα radiation and operating at 45 kV and 40 mA. The scanning range was 5° to 70° 2θ with increments of 0.017°. For the quantification of the amorphous content, the metal oxide sample was thoroughly mixed with about 10 wt.-% of a fully crystalline Rutile (r-TiO_2) standard material obtained from NIST. Diffractogram and Rietveld analysis was performed using PANalytical Highscore Plus v3 software. Quantification of the amorphous content was done according to the procedure described elsewhere [148].

7.5   Nitrogen adsorption

Surface area, pore volume and pore size distribution were determined by N_2 physisorption at -196 °C using a Sorptomatic 1990 automated surface area and pore size analyzer. Prior to the measurements all samples were evacuated at a temperature of 250 °C and a pressure of 10^{-2} mbar for 2 h. Surface area was calculated according to the Brunauer-Emmett-Teller (BET) method and pore volumes and pore size distribution were calculated using the Barrett-Joyner-Halenda (BJH) model.

7.6   Inductively coupled plasma optical emission spectrometry

Elemental analysis was performed on an SPECTRO Analytical Instruments Inc. SPECTROFLAME and an Agilent 760 ICP-OES spectrometer. Metal concentrations were determined using 281.615 nm (Mo), 311.817 nm (V), 214.282 nm (Te) and 313.078 nm (Nb) emission lines. Solid mixed metal oxide samples were fused in soda-potash mixture at 800 °C before being dissolved in millipore grade water.

7.7   UV-vis spectroscopy

UV-vis spectra were recorded in absorbance mode on a Hitachi U3000 spectrometer in a wavelength range of 200 nm – 1000 nm with a scanning rate of 600 nm min^{-1} using a slit with of 5 nm in a commercial quartz cuvette with Millipore grade water in an identical cuvette as a reference.

7.8   Scanning electron microscopy

The morphology of M1 phase particles was characterized using a high-resolution scanning electron microscope 7500F ColdFEG (JEOL) operating at an accelerating voltage of 2.0 kV and emission current of 10 µA. Working distance was about 8 mm.

7.9   Scanning transmission electron microscopy

Characterization of the edge termination of synthesized M1 crystals was carried out on a Thermo Fisher Scientific aberration-corrected Titan 80/300 TEM/STEM operated at 300 keV, housed in the Environmental Molecular Sciences Laboratory (EMSL) at the Pacific Northwest National Laboratory (PNNL). Correcting the spherical aberration by the illumination aberration corrector, Titan STEM allows a larger beam convergence angle, providing a small electron probe of high current. All high-angle annular dark-field (HAADF) STEM micrographs reported here were acquired with a convergence semi-angle of 17.4 mrad after fine tuning of the probe corrector, and an ADF detector semi-angles of around 70 – 200 mrad. Special care was taking to limit electron dose and prevent electron-beam effects on the catalysts. TEM samples of the M1 catalysts were prepared by standard microtome technique.

7.10 Catalytic activity

The activity and stability of the catalyst samples was tested in a fixed bed plug flow reactor setup (Figure 49) in the temperature range of 280 – 420 °C and in the pressure range of 1 – 4 bar(a). Up to 200 mg (depending on the activity of the sample) of catalyst (150 – 212 μm) were diluted with SiC (150 – 212 μm) in the ratio of 1:5 in order to achieve homogeneous heat distribution within the catalyst bed. The catalyst bed was fixed in a 4 mm i.d. quartz-coated stainless-steel tubular reactor. The total gas feed flow was 50 - 132 sccm and composed of 3 - 9 mol-% C_2H_6, 3 - 9 mol-% O_2 and 82 - 94 mol-% inert gases (He and N_2). Weight hourly space velocity was adjusted to a maximum ethane conversion of $X(C_2H_6)$ < 15 % in Arrhenius type experiments in order to suppress secondary reaction pathways. Blank tests in the absence of catalyst showed no conversion of reactants at the most severe conditions tested. Online gas analysis was performed using a Shimadzu "GC 2014" gas chromatography system equipped with a TCD detector (connected to HayeSep N, HayeSep Q and MolSieve 5A columns) and a FID detector (connected to a HP-PlotQ column). The GC system is capable of quantifying C2-hydrocarbons and -oxygenates, carbon mono- and dioxide, oxygen and nitrogen. The latter was used as internal standard to ensure closure of the carbon balance within ± 2 %.The main reaction product was ethene under all tested conditions. Carbon monoxide, carbon dioxide and traces of acetic acid were the only detected side products.
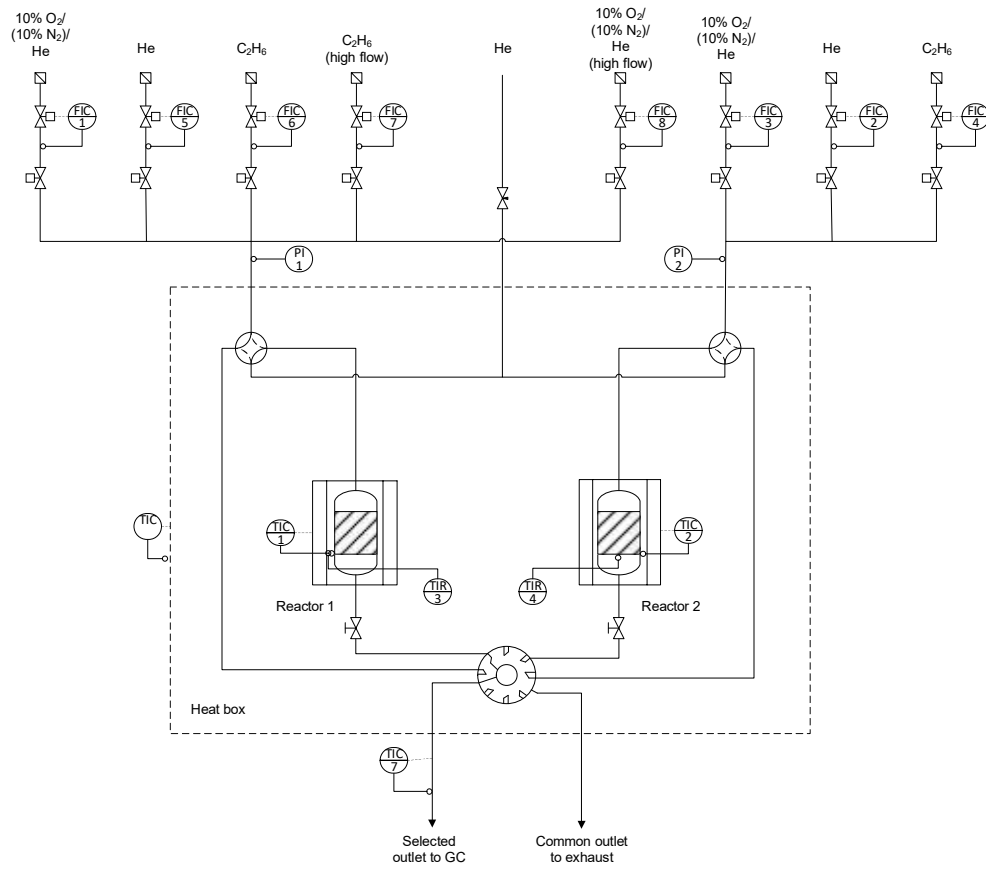
Figure 49: Flow sheet of reactor setup for catalytic testing.

8 References

1   Celaya Sanfiz, A. *et al.* Preparation of Phase-Pure M1 MoVTeNb Oxide Catalysts by Hydrothermal Synthesis—Influence of Reaction Parameters on Structure and Morphology. *Topics in Catalysis* **50**, 19-32, (2008).

2   Murphy, T. U.S. shale gas trends - economic and global implications. *Journal of Physics: Conference Series* **745**, 022004, (2016).

3   Siirola, J. J. The impact of shale gas in the chemical industry. *AIChE Journal* **60**, 810-819, (2014).

4   Eisele, P. & Killpack, R. in *Ullmann's Encyclopedia of Industrial Chemistry* (2012).

5   Obenaus, F. D., Wilhelm; Neumeister, Joachim. in *Ullmann's Encyclopedia of Industrial Chemistry*   (2011).

6   Zimmermann, H. & Walzl, R. in *Ullmann's Encyclopedia of Industrial Chemistry* (2012).

7   Plotkin,   J.   S.   *Beyond   the   Ethylene   Steam   Cracker*, <https://www.acs.org/content/acs/en/pressroom/cutting-edge-chemistry/beyond-the-ethylene-steam-cracker.html> (2016).

8   Plotkin,   J.   S.   *The   Propylene   Gap: How   Can   It   Be   Filled?*, <https://www.acs.org/content/acs/en/pressroom/cutting-edge-chemistry/the-propylene-gap-how-can-it-be-filled.html> (2015).

9   EIA,   U.   S.   *Ethane   production   at   Natural   Gas   Processing   Plants*, <https://www.eia.gov/outlooks/steo/data/browser/#/?v=27&f=A&s=&start=1997&end=2020&id=&maptype=0&ctype=linechart&linechart=ETFPPUS> (2019).

10   Maffia, G. J., Gaffney, A. M. & Mason, O. M. Techno-Economic Analysis of Oxidative Dehydrogenation Options. *Topics in Catalysis* **59**, 1573-1579, (2016).

11   Sabbe, M. K., Van Geem, K. M., Reyniers, M.-F. & Marin, G. B. First principle-based simulation of ethane steam cracking. *AIChE Journal* **57**, 482-496, (2011).

12   Sadrameli, S. M. Thermal/catalytic cracking of hydrocarbons for the production of olefins: A state-of-the-art review I: Thermal cracking review. *Fuel* **140**, 102-115, (2015).

13   Update, P. *US ETHYLENE COMPLEX CONSTRUCTION COSTS DATA 2018 – 2020*, <http://1.petchem-update.com/LP=19630?utm_campaign=4891-23JAN18-WK18-BD%20%28Karla%29&utm_medium=email&utm_source=Eloqua&elqTrackId=935d5544aade41199c38d13418644016&elq=a9b8ab69991c4152b6b73eee9d5b6917&elqaid=33734&elqat=1&elqCampaignId=17149> (2018).

14   Amghizar, I., Vandewalle, L. A., Van Geem, K. M. & Marin, G. B. New Trends in Olefin Production. *Engineering* **3**, 171-178, (2017).

15   EIA, U. S. *World Shale Resource Assessment*, <https://www.eia.gov/analysis/studies/worldshalegas/images/EIA_ARI_World_Shale_Gas_Oil_Basins_Logos_Map_092215_HighRes.jpg> (2015).

16   Gärtner, C. A., van Veen, A. C. & Lercher, J. A. Oxidative Dehydrogenation of Ethane: Common Principles and Mechanistic Aspects. *ChemCatChem* **5**, 3196-3217, (2013).

17   Baroi, C., Gaffney, A. M. & Fushimi, R. Process economics and safety considerations for the oxidative dehydrogenation of ethane using the M1 catalyst. *Catalysis Today* **298**, 138-144, (2017).

18   He, C. & You, F. Shale Gas Processing Integrated with Ethylene Production: Novel Process Designs, Exergy Analysis, and Techno-Economic Analysis. *Industrial & Engineering Chemistry Research* **53**, 11442-11459, (2014).

19   Torabi, A., Kazemeini, M. & Fattahi, M. Developing a mathematical model for the oxidative dehydrogenation of propane in a fluidized bed reactor. *Asia-Pacific Journal of Chemical Engineering* **11**, 448-459, (2016).

20   Alavi-Amleshi, S. M. Comparative study of propane oxidative dehydrogenation in fluidized and fixed bed reactor AU - Zaynali, Yousef. *Particulate Science and Technology* **35**, 667-673, (2017).

21   Aparicio-Mauricio, G., Ruiz, R. S., López-Isunza, F. & Castillo-Araiza, C. O. A simple approach to describe hydrodynamics and its effect on heat and mass

transport in an industrial wall-cooled fixed bed catalytic reactor: ODH of ethane on a MoVNbTeO formulation. *Chemical Engineering Journal* **321**, 584-599, (2017).

22   Cavani, F., Chieregato, A., López Nieto, J. M. & Millet, J.-M. M. Gas-Phase Oxidation of Alkanes. *Alkane Functionalization*, (2019).

23   Skoufa, Z., Giannakakis, G., Heracleous, E. & Lemonidou, A. A. Simulation-aided effective design of a catalytic reactor for ethane oxidative dehydrogenation over NiNbOx. *Catalysis Today* **299**, 102-111, (2018).

24   Rodríguez, M. L., Ardissone, D. E., López, E., Pedernera, M. N. & Borio, D. O. Reactor Designs for Ethylene Production via Ethane Oxidative Dehydrogenation: Comparison of Performance. *Industrial & Engineering Chemistry Research* **50**, 2690-2697, (2011).

25   Rodriguez, M. L. *et al.* Oxidative dehydrogenation of ethane to ethylene in a membrane reactor: A theoretical study. *Catalysis Today* **157**, 303-309, (2010).

26   Myint, M., Yan, B., Wan, J., Zhao, S. & Chen, J. G. Reforming and oxidative dehydrogenation of ethane with CO2 as a soft oxidant over bimetallic catalysts. *Journal of Catalysis* **343**, 168-177, (2016).

27   Bai, P. T., Rajmohan, K. S., Prasad, P. S. S. & Srinath, S. in *CO2 Separation, Purification and Conversion to Chemicals and Fuels* (eds Franz Winter, Rashmi Avinash Agarwal, Jan Hrdlicka, & Sunita Varjani) 93-117 (Springer Singapore, 2019).

28   Mukherjee, D., Park, S.-E. & Reddy, B. M. CO2 as a soft oxidant for oxidative dehydrogenation reaction: An eco benign process for industry. *Journal of CO2 Utilization* **16**, 301-312, (2016).

29   Grzybowska-Świerkosz, B. Active centres on vanadia-based catalysts for selective oxidation of hydrocarbons. *Applied Catalysis A: General* **157**, 409-420, (1997).

30   Mars, P. & van Krevelen, D. W. Oxidations carried out by means of vanadium oxide catalysts. *Chemical Engineering Science* **3**, 41-59, (1954).

31   Vannice, M. A. An analysis of the Mars–van Krevelen rate expression. *Catalysis Today* **123**, 18-22, (2007).

32   Grasselli, R. K. Fundamental Principles of Selective Heterogeneous Oxidation Catalysis. *Topics in Catalysis* **21**, 79-88, (2002).

33   Bielański, A. & Haber, J. Oxygen in Catalysis on Transition Metal Oxides. *Catalysis Reviews* **19**, 1-41, (1979).

34   Bielański, A. & Haber, J. *Oxygen in catalysis.* (M. Dekker, 1991).

35   Millet, J. M. M. Mechanism of first hydrogen abstraction from light alkanes on oxide catalysts. *Topics in Catalysis* **38**, 83-92, (2006).

36   Heracleous, E., Lee, A. F., Wilson, K. & Lemonidou, A. A. Investigation of Ni-based alumina-supported catalysts for the oxidative dehydrogenation of ethane to ethylene: structural characterization and reactivity studies. *Journal of Catalysis* **231**, 159-171, (2005).

37   Heracleous, E. & Lemonidou, A. A. Ni–Me–O mixed metal oxides for the effective oxidative dehydrogenation of ethane to ethylene – Effect of promoting metal Me. *Journal of Catalysis* **270**, 67-75, (2010).

38   Heracleous, E. & Lemonidou, A. A. Ni–Nb–O mixed oxides as highly active and selective catalysts for ethene production via ethane oxidative dehydrogenation. Part I: Characterization and catalytic performance. *Journal of Catalysis* **237**, 162-174, (2006).

39   Laveille, P., Biausque, G., Zhu, H., Basset, J.-M. & Caps, V. A high-throughput study of the redox properties of Nb-Ni oxide catalysts by low temperature CO oxidation: Implications in ethane ODH. *Catalysis Today* **203**, 3-9, (2013).

40   Heracleous, E. & Lemonidou, A. A. Ni–Nb–O mixed oxides as highly active and selective catalysts for ethene production via ethane oxidative dehydrogenation. Part II: Mechanistic aspects and kinetic modeling. *Journal of Catalysis* **237**, 175-189, (2006).

41   Chieregato, A., López Nieto, J. M. & Cavani, F. Mixed-oxide catalysts with vanadium as the key element for gas-phase reactions. *Coordination Chemistry Reviews* **301-302**, 3-23, (2015).

42   Vedrine, J. C. Heterogeneous Partial (amm) Oxidation and Oxidative Dehydrogenation Catalysis on Mixed Metal Oxides. *Catalysts* **6**, (2016).

43   Wachs, I. E. & Routray, K. Catalysis Science of Bulk Mixed Oxides. *ACS Catalysis* **2**, 1235-1246, (2012).

44   Argyle, M. D., Chen, K., Bell, A. T. & Iglesia, E. Effect of Catalyst Structure on Oxidative Dehydrogenation of Ethane and Propane on Alumina-Supported Vanadia. *Journal of Catalysis* **208**, 139-149, (2002).

45   Argyle, M. D., Chen, K., Bell, A. T. & Iglesia, E. Ethane Oxidative Dehydrogenation Pathways on Vanadium Oxide Catalysts. *The Journal of Physical Chemistry B* **106**, 5421-5427, (2002).

46   Chen, K., Bell, A. T. & Iglesia, E. The Relationship between the Electronic and Redox Properties of Dispersed Metal Oxides and Their Turnover Rates in Oxidative Dehydrogenation Reactions. *Journal of Catalysis* **209**, 35-42, (2002).

47   Chen, K., Iglesia, E. & Bell, A. T. Kinetic Isotopic Effects in Oxidative Dehydrogenation of Propane on Vanadium Oxide Catalysts. *Journal of Catalysis* **192**, 197-203, (2000).

48   Chen, K., Iglesia, E. & Bell, A. T. Isotopic Tracer Studies of Reaction Pathways for Propane Oxidative Dehydrogenation on Molybdenum Oxide Catalysts. *The Journal of Physical Chemistry B* **105**, 646-653, (2001).

49   Chen, K., Iglesia, E. & Bell, A. T. in *Studies in Surface Science and Catalysis* Vol. 136 (eds E. Iglesia, J. J. Spivey, & T. H. Fleisch) 507-512 (Elsevier, 2001).

50   Chen, K., Khodakov, A., Yang, J., Bell, A. T. & Iglesia, E. Isotopic Tracer and Kinetic Studies of Oxidative Dehydrogenation Pathways on Vanadium Oxide Catalysts. *Journal of Catalysis* **186**, 325-333, (1999).

51   Chen, K., Xie, S., Bell, A. T. & Iglesia, E. Structure and Properties of Oxidative Dehydrogenation Catalysts Based on MoO3/Al2O3. *Journal of Catalysis* **198**, 232-242, (2001).

52   Chen, K., Xie, S., Iglesia, E. & Bell, A. T. Structure and Properties of Zirconia-Supported Molybdenum Oxide Catalysts for Oxidative Dehydrogenation of Propane. *Journal of Catalysis* **189**, 421-430, (2000).

53   Kondratenko, E. V. & Brückner, A. On the nature and reactivity of active oxygen species formed from O2 and N2O on VOx/MCM-41 used for oxidative dehydrogenation of propane. *Journal of Catalysis* **274**, 111-116, (2010).

54   Malleswara Rao, T. V. & Deo, G. Kinetic parameter analysis for propane ODH: V2O5/Al2O3 and MoO3/Al2O3 catalysts. *AIChE Journal* **53**, 1538-1549, (2007).

55   Malleswara Rao, T. V., Vico-Ruiz, E., Bañares, M. A. & Deo, G. Obtaining the best composition of supported V2O5–MoO3/TiO2 catalyst for propane ODH reaction. *Journal of Catalysis* **258**, 324-333, (2008).

56   Shee, D., Deo, G. & Hirt, A. M. Characterization and reactivity of sol–gel synthesized TiO2–Al2O3 supported vanadium oxide catalysts. *Journal of Catalysis* **273**, 221-228, (2010).

57   Yang, S., Iglesia, E. & Bell, A. T. Oxidative Dehydrogenation of Propane over V2O5/MoO3/Al2O3 and V2O5/Cr2O3/Al2O3: Structural Characterization and Catalytic Function. *The Journal of Physical Chemistry B* **109**, 8987-9000, (2005).

58   Chen, K., Bell, A. T. & Iglesia, E. Kinetics and Mechanism of Oxidative Dehydrogenation of Propane on Vanadium, Molybdenum, and Tungsten Oxides. *The Journal of Physical Chemistry B* **104**, 1292-1299, (2000).

59   Grabowski, R. Kinetics of Oxidative Dehydrogenation of C2-C3 Alkanes on Oxide Catalysts. *Catalysis Reviews* **48**, 199-268, (2006).

60   Mitra, B., Wachs, I. E. & Deo, G. Promotion of the propane ODH reaction over supported V2O5/Al2O3 catalyst with secondary surface metal oxide additives. *Journal of Catalysis* **240**, 151-159, (2006).

61   López Nieto, J. M. *et al.* Oxidative Dehydrogenation of Alkanes over V-based Catalysts: Influence of Redox Properties on Catalytic Performance. *Journal of Catalysis* **185**, 324-332, (1999).

62   Nieto, J. M. L. The selective oxidative activation of light alkanes. From supported vanadia to multicomponent bulk V-containing catalysts. *Topics in Catalysis* **41**, 3-15, (2006).

63   Thorsteinson, E. M., Wilson, T. P., Young, F. G. & Kasai, P. H. The oxidative dehydrogenation of ethane over catalysts containing mixed oxides of molybdenum and vanadium. *Journal of Catalysis* **52**, 116-132, (1978).

64   Takashi, U. & Yukio, K. Production of Ethylene. Japan patent (1993).

65   TAKASHI, U., HIROYA, N., YUKIO, K. & SHIN, W. Method for producing an unsaturated carboxylic acid. (1994).

66   MASAKATSU, H. & ATSUSH, K. Process for producing nitriles. (1989).

67   Ushikubo, T., Oshima, K., Kayou, A. & Hatano, M. in *Studies in Surface Science and Catalysis* Vol. 112 (eds Can Li & Qin Xin) 473-480 (Elsevier, 1997).

68   Bagheri, S. & Julkapli, N. M. Mo3VOx catalyst in biomass conversion: A review in structural evolution and reaction pathways. *International Journal of Hydrogen Energy* **42**, 2116-2126, (2017).

69   Gartner, C. A., van Veen, A. C. & Lercher, J. A. Oxidative Dehydrogenation of Ethane: Common Principles and Mechanistic Aspects. *ChemCatChem* **5**, 3196-3217, (2013).

70   Grant, J. T., Venegas, J. M., McDermott, W. P. & Hermans, I. Aerobic Oxidations of Light Alkanes over Solid Metal Oxide Catalysts. *Chem Rev* **118**, 2769-2815, (2018).

71   Ueda, W. Establishment of Crystalline Complex Mo-V-Oxides as Selective Oxidation Catalysts. *Journal of the Japan Petroleum Institute* **56**, 122-132, (2013).

72   Li, X., Buttrey, D. J., Blom, D. A. & Vogt, T. Improvement of the Structural Model for the M1 Phase Mo–V–Nb–Te–O Propane (Amm)oxidation Catalyst. *Topics in Catalysis* **54**, 614-626, (2011).

73   Lunkenbein, T. *et al.* Direct imaging of octahedral distortion in a complex molybdenum vanadium mixed oxide. *Angew Chem Int Ed Engl* **54**, 6828-6831, (2015).

74   Yu, J. J., Woo, J., Borisevich, A., Xu, Y. & Guliants, V. V. A combined HAADF STEM and density functional theory study of tantalum and niobium locations in the Mo-V-Te-Ta(Nb)-O M1 phases. *Catalysis Communications* **29**, 68-72, (2012).

75   Grasselli, R. K. *et al.* Active centers, catalytic behavior, symbiosis and redox properties of MoV(Nb,Ta)TeO ammoxidation catalysts. *Topics in Catalysis* **38**, 7-16, (2006).

76   DeSanto, P. *et al.* Comparison of MoVTaTeO and MoVNbTeO M1 crystal chemistry. *Topics in Catalysis* **38**, 31-40, (2006).

77   Baca, M. & Millet, J.-M. M. Bulk oxidation state of the different cationic elements in the MoVTe(Sb)NbO catalysts for oxidation or ammoxidation of propane. *Applied Catalysis A: General* **279**, 67-77, (2005).

78   DeSanto, P. *et al.* Structural aspects of the M1 and M2 phases in MoVNbTeO propane ammomidation catalysts. *Zeitschrift Fur Kristallographie* **219**, 152-165, (2004).

79   Blom, D. A., Li, X., Mitra, S., Vogt, T. & Buttrey, D. J. STEM HAADF Image Simulation of the Orthorhombic M1 Phase in the Mo-V-Nb-Te-O Propane Oxidation Catalyst. *ChemCatChem* **3**, 1028-1033, (2011).

80   DeSanto, P. *et al.* Structural Characterization of the Orthorhombic Phase M1 in MoVNbTeO Propane Ammoxidation Catalyst. *Topics in Catalysis* **23**, 23-38, (2003).

81   Melzer, D. *et al.* Design and synthesis of highly active MoVTeNb-oxides for ethane oxidative dehydrogenation. *Nature Communications* **10**, 4012, (2019).

82   Blom, D. A., Pyrz, W. D., Vogt, T. & Buttrey, D. J. Aberration-corrected STEM investigation of the M2 phase of MoVNbTeO selective oxidation catalyst. *Microscopy* **58**, 193-198, (2008).

83   Kihlborg, L. Crystal structure on Mo5O14, a compound exhibiting two-dimensional disorder. *Arkiv foer Kemi* **21**, 427 - 437, (1963).

84   Katou, T., Vitry, D. & Ueda, W. Hydrothermal Synthesis of A New Mo–V–O Complex Metal Oxide and Its Catalytic Activity for The Oxidation of Propane. *Chemistry Letters* **32**, 1028-1029, (2003).

85   Ueda, W., Vitry, D. & Katou, T. Crystalline MoVO based complex oxides as selective oxidation catalysts of propane. *Catalysis Today* **99**, 43-49, (2005).

86   Sadakane, M. *et al.* Molybdenum–Vanadium-Based Molecular Sieves with Microchannels of Seven-Membered Rings of Corner-Sharing Metal Oxide Octahedra. *Angewandte Chemie International Edition* **47**, 2493-2496, (2008).

87   Botella, P., Concepción, P., Nieto, J. M. L. & Moreno, Y. The influence of Te-precursor in Mo-V-Te-O and Mo-V-Te-Nb-O catalysts on their catalytic behaviour in the selective propane oxidation. *Catalysis Today* **99**, 51-57, (2005).

88   Botella, P. *et al.* Selective oxidative dehydrogenation of ethane on MoVTeNbO mixed metal oxide catalysts. *J. Catal.* **225**, 428-438, (2004).

89   Solsona, B., Ivars, F., Concepción, P. & López Nieto, J. M. Selective oxidation of n-butane over MoV-containing oxidic bronze catalysts. *Journal of Catalysis* **250**, 128-138, (2007).

90   Botella, P., Dejoz, A., Lopeznieto, J., Concepcion, P. & Vazquez, M. Selective oxidative dehydrogenation of ethane over MoVSbO mixed oxide catalysts. *Applied Catalysis A: General* **298**, 16-23, (2006).

91   Woo, J., Sanghavi, U., Vonderheide, A. & Guliants, V. V. A study of M1/M2 phase synergy in the MoVTe(Nb,Ta)O catalysts for propane ammoxidation to acrylonitrile. *Applied Catalysis A: General* **515**, 179-189, (2016).

92   Amakawa, K. *et al.* Multifunctionality of Crystalline MoV(TeNb) M1 Oxide Catalysts in Selective Oxidation of Propane and Benzyl Alcohol. *ACS Catalysis* **3**, 1103-1113, (2013).

93   Kolen'ko Yury, V. *et al.* Synthesis of MoVTeNb Oxide Catalysts with Tunable Particle Dimensions. *ChemCatChem* **3**, 1597-1606, (2011).

94   Popova, G. Y. *et al.* Formation of active phases in MoVTeNb oxide catalysts for ammoxidation of propane. *Catalysis Today* **144**, 312-317, (2009).

95   Ishchenko, E. V. *et al.* The structure and catalytic properties of amorphous phase in MoVTeO catalysts for propane ammoxidation. *Applied Catalysis a-General* **476**, 91-102, (2014).

96   Girgsdies, F., Schlogl, R. & Trunschke, A. In-situ X-ray diffraction study of phase crystallization from an amorphous MoVTeNb oxide catalyst precursor. *Catalysis Communications* **18**, 60-62, (2012).

97   Chu, B., Truter, L., Nijhuis, T. A. & Cheng, Y. Performance of phase-pure M1 MoVNbTeOx catalysts by hydrothermal synthesis with different post-treatments for the oxidative dehydrogenation of ethane. *Applied Catalysis A: General* **498**, 99-106, (2015).

98   Concepción, P., Hernández, S. & Nieto, J. M. L. On the nature of active sites in MoVTeO and MoVTeNbO catalysts: The influence of catalyst activation temperature. *Applied Catalysis A: General* **391**, 92-101, (2011).

99   Nieto, J. M. L., Botella, P., Vazquez, M. I. & Dejoz, A. The selective oxidative dehydrogenation of ethane over hydrothermally synthesised MoVTeNb catalysts. *Chemical Communications*, 1906-1907, (2002).

100   Vitry, D. Mo-V-Te-(Nb)-O mixed metal oxides prepared by hydrothermal synthesis for catalytic selective oxidations of propane and propene to acrylic acid. *Applied Catalysis A: General* **251**, 411-424, (2003).

101   Deniau, B., Bergeret, G., Jouguet, B., Dubois, J. L. & Millet, J. M. M. Preparation of Single M1 Phase MoVTe(Sb)NbO Catalyst: Study of the Effect of M2 Phase Dissolution on the Structure and Catalytic Properties. *Topics in Catalysis* **50**, 33-42, (2008).

102   Nguyen, T. T., Aouine, M. & Millet, J. M. M. Optimizing the efficiency of MoVTeNbO catalysts for ethane oxidative dehydrogenation to ethylene. *Catalysis Communications* **21**, 22-26, (2012).

103   Qiu, C. *et al.* Synthesis of crystalline Mo–V–W–O complex oxides with orthorhombic and trigonal structures and their application as catalysts. *Catalysis, Structure & Reactivity* **1**, 71-77, (2015).

104   Sanchez Sanchez, M. *et al.* Aiding the Self-Assembly of Supramolecular Polyoxometalates under Hydrothermal Conditions To Give Precursors of Complex Functional Oxides. *Angewandte Chemie International Edition* **51**, 7194-7197, (2012).

105   Ishikawa, S., Zhang, Z. X. & Ueda, W. Unit Synthesis Approach for Creating High Dimensionally Structured Complex Metal Oxides as Catalysts for Selective Oxidations. *ACS Catalysis* **8**, 2935-2943, (2018).

106   Sadakane, M. *et al.* Assembly of a Pentagonal Polyoxomolybdate Building Block, [Mo6O21](6-), into Crystalline MoV Oxides. *European Journal of Inorganic Chemistry*, 1731-1736, (2013).

107   Ishikawa, S. *et al.* Multi-dimensional Crystal Structuring of Complex Metal Oxide Catalysts of Group V and VI Elements by Unit-Assembling. *Topics in Catalysis*, (2018).

108   Noack, J., Rosowski, F., Schlögl, R. & Trunschke, A. Speciation of Molybdates under Hydrothermal Conditions. *Zeitschrift für anorganische und allgemeine Chemie* **640**, 2730-2736, (2014).

109   Sadakane, M. *et al.* Synthesis of orthorhombic Mo-V-Sb oxide species by assembly of pentagonal Mo6O21 polyoxometalate building blocks. *Angew Chem Int Ed Engl* **48**, 3782-3786, (2009).

110   Ueda, W., Vitry, D. & Katou, T. Structural organization of catalytic functions in Mo-based oxides for propane selective oxidation. *Catalysis Today* **96**, 235-240, (2004).

111   Sanchez Sanchez, M. *et al.* Aiding the self-assembly of supramolecular polyoxometalates under hydrothermal conditions to give precursors of complex functional oxides. *Angew Chem Int Ed Engl* **51**, 7194-7197, (2012).

112   Canioni, R. *et al.* Selective conversion of {Mo-132} Keplerate ion into 4-electron reduced crown-capped Keggin derivative [Te5Mo15O57](8-). A key intermediate to single-phase M1 multielement MoVTeO light-alkanes oxidation catalyst. *Chemical Communications* **47**, 6413-6415, (2011).

113   Biswas, S. *et al.* Direct Observation of the Formation Pathway of [Mo-132] Keplerates. *Inorg Chem* **55**, 8285-8291, (2016).

114   Yin, P. *et al.* Reduction-Triggered Self-Assembly of Nanoscale Molybdenum Oxide Molecular Clusters. *Journal of the American Chemical Society* **138**, 10623-10629, (2016).

115   Ishikawa, S., Tashiro, M., Murayama, T. & Ueda, W. Seed-Assisted Synthesis of Crystalline Mo3VOx Oxides and Their Crystal Formation Mechanism. *Crystal Growth & Design* **14**, 4553-4561, (2014).

116   Chu, B., Truter, L. A., Nijhuis, T. A. & Cheng, Y. Oxidative dehydrogenation of ethane to ethylene over phase-pure M1 MoVNbTeOx catalyst in a micro-channel reactor. *Catalysis Science & Technology*, (2015).

117   Ishikawa, S., Yi, X. D., Murayama, T. & Ueda, W. Catalysis field in orthorhombic Mo3VOx oxide catalyst for the selective oxidation of ethane, propane and acrolein. *Catalysis Today* **238**, 35-40, (2014).

118   Jimenez, J., Mingle, K., Bureerug, T., Wen, C. & Lauterbach, J. Statistically Guided Synthesis of MoV-Based Mixed-Oxide Catalysts for Ethane Partial Oxidation. *Catalysts* **8**, (2018).

119   d'Alnoncourt, R. N. *et al.* The reaction network in propane oxidation over phase-pure MoVTeNb M1 oxide catalysts. *Journal of Catalysis* **311**, 369-385, (2014).

120   Grasselli, R. K., Lugmair, C. G. & Volpe, A. F. Towards an Understanding of the Reaction Pathways in Propane Ammoxidation Based on the Distribution of Elements at the Active Centers of the M1 Phase of the MoV(Nb,Ta)TeO System. *Topics in Catalysis* **54**, 595-604, (2011).

121   Hävecker, M. *et al.* Surface chemistry of phase-pure M1 MoVTeNb oxide during operation in selective oxidation of propane to acrylic acid. *Journal of Catalysis* **285**, 48-60, (2012).

122   Ishchenko, E. V. *et al.* Role of MoVTeNb oxide catalyst constituent phases in propane oxidation to acrylic acid. *Catalysis for Sustainable Energy* **1**, (2013).

123   Muthukumar, K., Yu, J., Xu, Y. & Guliants, V. V. Propane Ammoxidation Over the Mo–V–Te–Nb–O M1 Phase: Reactivity of Surface Cations in Hydrogen Abstraction Steps. *Topics in Catalysis* **54**, 605-613, (2011).

124   Oliver, J. M., Nieto, J. M. L. & Botella, P. Selective oxidation and ammoxidation of propane on a Mo–V–Te–Nb–O mixed metal oxide catalyst: a comparative study. *Catalysis Today* **96**, 241-249, (2004).

125   Ueda, W., Vitry, D., Kato, T., Watanabe, N. & Endo, Y. Key aspects of crystalline Mo-V-O-based catalysts active in the selective oxidation of propane. *Research on Chemical Intermediates* **32**, 217-233, (2006).

126   Naraschewski, F. N., Kumar, C. P., Jentys, A. & Lercher, J. A. Phase formation and selective oxidation of propane over MoVTeNbOx catalysts with varying compositions. *Applied Catalysis a-General* **391**, 63-69, (2011).

127   López Nieto, J. M. *et al.* Reaction products and pathways in the selective oxidation of C2–C4 alkanes on MoVTeNb mixed oxide catalysts. *Catalysis Today* **157**, 291-296, (2010).

128   Guan, J. *et al.* Synthesis and characterization of MoVTeCeO catalysts and their catalytic performance for selective oxidation of isobutane and isobutylene. *Journal of Catalysis* **251**, 354-362, (2007).

129   Weber, D., Weidler, P. & Kraushaar-Czarnetzki, B. Partial Oxidation of Isobutane and Isobutene to Methacrolein Over a Novel Mo–V–Nb(–Te) Mixed Oxide Catalyst. *Topics in Catalysis* **60**, 1401-1407, (2017).

130   Koltunov, K. Y., Ishchenko, E. V. & Sobolev, V. I. Promoting effect of 4-dimethylaminopyridine on selective oxidation of benzyl alcohol over MoVTeNb mixed oxides. *Catalysis Communications* **117**, 49-52, (2018).

131   Sobolev, V. I. & Koltunov, K. Y. MoVNbTe Mixed Oxides as Efficient Catalyst for Selective Oxidation of Ethanol to Acetic Acid. *ChemCatChem* **3**, 1143-1145, (2011).

132   Sobolev, V. I. & Koltunov, K. Y. Oxidative and non-oxidative degradation of C1–C3 carboxylic acids over V2O5/TiO2 and MoVTeNb oxides: A comparative study. *Applied Catalysis A: General* **466**, 45-50, (2013).

133   Korovchenko, P. *et al.* M1 to M2 Phase Transformation and Phase Cooperation in Bulk Mixed Metal Mo-V-M-O (M=Te, Nb) Catalysts for Selective Ammoxidation of Propane. *Topics in Catalysis* **50**, 43-51, (2008).

134   Botella, P., García-González, E., López Nieto, J. M. & González-Calbet, J. M. MoVTeNbO multifunctional catalysts: Correlation between constituent crystalline phases and catalytic performance. *Solid State Sciences* **7**, 507-519, (2005).

135   Naraschewski, F. N., Jentys, A. & Lercher, J. A. On the Role of the Vanadium Distribution in MoVTeNbO x Mixed Oxides for the Selective Catalytic Oxidation of Propane. *Topics in Catalysis* **54**, 639-649, (2011).

136   Grasselli, R. K. *et al.* Active centers in Mo–V–Nb–Te–Ox (amm)oxidation catalysts. *Catalysis Today* **91-92**, 251-258, (2004).

137   Zhu, Y., Lu, W., Li, H. & Wan, H. Selective modification of surface and bulk V5+/V4+ ratios and its effects on the catalytic performance of MoVTeO catalysts. *Journal of Catalysis* **246**, 382-389, (2007).

138   Chu, B., An, H., Nijhuis, T. A., Schouten, J. C. & Cheng, Y. A self-redox pure-phase M1 MoVNbTeOx/CeO2 nanocomposite as a highly active catalyst for oxidative dehydrogenation of ethane. *Journal of Catalysis* **329**, 471-478, (2015).

139   Ishchenko, E. V. *et al.* Effect of K and Bi doping on the M1 phase in MoVTeNbO catalysts for ethane oxidative conversion to ethylene. *Applied Catalysis A: General* **514**, 1-13, (2016).

140   Celaya Sanfiz, A. *et al.* How important is the (001) plane of M1 for selective oxidation of propane to acrylic acid? *Journal of Catalysis* **258**, 35-43, (2008).

141   Schlögl, R. Active Sites for Propane Oxidation: Some Generic Considerations. *Topics in Catalysis* **54**, 627-638, (2011).

142   Grasselli, R. K. & Volpe, A. F. Catalytic Consequences of a Revised Distribution of Key Elements at the Active Centers of the M1 Phase of the MoVNbTeOx System. *Topics in Catalysis* **57**, 1124-1137, (2014).

143   Ishikawa, S. *et al.* Redox Treatment of Orthorhombic Mo29V11O112and Relationships between Crystal Structure, Microporosity and Catalytic Performance for Selective Oxidation of Ethane. *The Journal of Physical Chemistry C* **119**, 7195-7206, (2015).

144   Ishikawa, S., Yi, X., Murayama, T. & Ueda, W. Heptagonal channel micropore of orthorhombic Mo3VOx as catalysis field for the selective oxidation of ethane. *Applied Catalysis A: General* **474**, 10-17, (2014).

145   Annamalai, L. *et al.* Influence of Tight Confinement on Selective Oxidative Dehydrogenation of Ethane on MoVTeNb Mixed Oxides. *ACS Catalysis* **8**, 7051-7067, (2018).

146   Cheng, M. J. & Goddard, W. A. In Silico Design of Highly Selective Mo-V-Te-Nb-O Mixed Metal Oxide Catalysts for Ammoxidation and Oxidative

Dehydrogenation of Propane and Ethane. *Journal of the American Chemical Society* **137**, 13224-13227, (2015).

147   Cheng, M. J. & Goddard, W. A. The Mechanism of Alkane Selective Oxidation by the M1 Phase of Mo-V-Nb-Te Mixed Metal Oxides: Suggestions for Improved Catalysts. *Topics in Catalysis* **59**, 1506-1517, (2016).

148   Melzer, D. *et al.* Atomic-Scale Determination of Active Facets on the MoVTeNb Oxide M1 Phase and Their Intrinsic Catalytic Activity for Ethane Oxidative Dehydrogenation. *Angew Chem Int Ed Engl* **55**, 8873-8877, (2016).

149   Carrero, C. A., Schloegl, R., Wachs, I. E. & Schomaecker, R. Critical Literature Review of the Kinetics for the Oxidative Dehydrogenation of Propane over Well-Defined Supported Vanadium Oxide Catalysts. *ACS Catalysis* **4**, 3357-3380, (2014).

150   Sprung, C., Yablonsky, S. G., Schlögl, R. & Trunschke, A. Constructing A Rational Kinetic Model of the Selective Propane Oxidation Over A Mixed Metal Oxide Catalyst. *Catalysts* **8**, (2018).

151   Che-Galicia, G., Quintana-Solórzano, R., Ruiz-Martínez, R. S., Valente, J. S. & Castillo-Araiza, C. O. Kinetic modeling of the oxidative dehydrogenation of ethane to ethylene over a MoVTeNbO catalytic system. *Chemical Engineering Journal* **252**, 75-88, (2014).

152   Valente, J. S., Quintana-Solórzano, R., Armendáriz-Herrera, H., Barragán-Rodríguez, G. & López-Nieto, J. M. Kinetic Study of Oxidative Dehydrogenation of Ethane over MoVTeNb Mixed-Oxide Catalyst. *Industrial & Engineering Chemistry Research* **53**, 1775-1786, (2014).

153   Kube, P. *et al.* Functional Analysis of Catalysts for Lower Alkane Oxidation. *ChemCatChem* **9**, 573-585, (2017).

154   Kube, P., Frank, B., Schlogl, R. & Trunschke, A. Isotope Studies in Oxidation of Propane over Vanadium Oxide. *ChemCatChem* **9**, 3446-3455, (2017).

155   Wernbacher, A. M., Kube, P., Hävecker, M., Schlögl, R. & Trunschke, A. Electronic and Dielectric Properties of MoV-Oxide (M1 Phase) under Alkane Oxidation Conditions. *The Journal of Physical Chemistry C*, (2019).

156   Caldararu, M. *et al.* Electrical conductivity of a MoVTeNbO catalyst in propene oxidation measured in operando conditions. *Catalysis Today* **155**, 311-318, (2010).

157   Heine, C. *et al.* Work Function, Band Bending, and Microwave Conductivity Studies on the Selective Alkane Oxidation Catalyst MoVTeNb Oxide (Orthorhombic M1 Phase) under Operation Conditions. *The Journal of Physical Chemistry C* **117**, 26988-26997, (2013).

158   Heine, C., Havecker, M., Trunschke, A., Schlögl, R. & Eichelbaum, M. The impact of steam on the electronic structure of the selective propane oxidation catalyst MoVTeNb oxide (orthorhombic M1 phase). *Physical Chemistry Chemical Physics* **17**, 8983-8993, (2015).

159   Leveles, L., Seshan, K., Lercher, J. A. & Lefferts, L. Oxidative conversion of propane over lithium-promoted magnesia catalyst: I. Kinetics and mechanism. *Journal of Catalysis* **218**, 296-306, (2003).

160   Leveles, L., Seshan, K., Lercher, J. A. & Lefferts, L. Oxidative conversion of propane over lithium-promoted magnesia catalyst: II. Active site characterization and hydrocarbon activation. *Journal of Catalysis* **218**, 307-314, (2003).

161   Morales, E. & Lunsford, J. H. Oxidative dehydrogenation of ethane over a lithium-promoted magnesium oxide catalyst. *Journal of Catalysis* **118**, 255-265, (1989).

162   Leveles, L., Fuchs, S., Seshan, K., Lercher, J. A. & Lefferts, L. Oxidative conversion of light alkanes to olefins over alkali promoted oxide catalysts. *Applied Catalysis A: General* **227**, 287-297, (2002).

163   Arndt, S. *et al.* A Critical Assessment of Li/MgO-Based Catalysts for the Oxidative Coupling of Methane. *Catalysis Reviews* **53**, 424-514, (2011).

164   Wang, D., Rosynek, M. P. & Lunsford, J. H. The role of Cl− in a Li+-ZnO-Cl− catalyst on the oxidative coupling of methane and the oxidative dehydrogenation of ethane. *Chemical Engineering & Technology* **18**, 118-124, (1995).

165   Wang, S., Murata, K., Hayakawa, T., Hamakawa, S. & Suzuki, K. Oxidative Dehydrogenation of Ethane over Alkali Metal Chloride Modified Silica Catalysts. *Energy & Fuels* **14**, 899-903, (2000).

166   Gaab, S., Find, J., Grasselli, R. K. & Lercher, J. A. in *Studies in Surface Science and Catalysis* Vol. 147 (eds Xinhe Bao & Yide Xu) 673-678 (Elsevier, 2004).

167   Gaab, S., Machli, M., Find, J., Grasselli, R. K. & Lercher, J. A. Oxidative Dehydrogenation of Ethane Over Novel Li/Dy/Mg Mixed Oxides: Structure–Activity Study. *Topics in Catalysis* **23**, 151-158, (2003).

168   Gärtner, C. A., van Veen, A. C. & Lercher, J. A. Highly Selective Supported Alkali Chloride Catalysts for the Oxidative Dehydrogenation of Ethane. *Topics in Catalysis* **57**, 1236-1247, (2014).

169   Tope, B., Zhu, Y. & Lercher, J. A. Oxidative dehydrogenation of ethane over Dy2O3/MgO supported LiCl containing eutectic chloride catalysts. *Catalysis Today* **123**, 113-121, (2007).

170   Gärtner, C. A., van Veen, A. C. & Lercher, J. A. Oxidative Dehydrogenation of Ethane on Dynamically Rearranging Supported Chloride Catalysts. *Journal of the American Chemical Society* **136**, 12691-12701, (2014).

171   Gaab, S., Find, J., Müller, T. E. & Lercher, J. A. Kinetics and mechanism of the oxidative dehydrogenation of ethane over Li/Dy/Mg/O/(Cl) mixed oxide catalysts. *Topics in Catalysis* **46**, 101-110, (2007).

172   Venegas, J. M., McDermott, W. P. & Hermans, I. Serendipity in Catalysis Research: Boron-Based Materials for Alkane Oxidative Dehydrogenation. *Accounts of Chemical Research* **51**, 2556-2564, (2018).

173   Grant, J. T. *et al.* Selective oxidative dehydrogenation of propane to propene using boron nitride catalysts. *Science* **354**, 1570-1573, (2016).

174   Loiland, J. A., Zhao, Z., Patel, A. & Hazin, P. Boron-Containing Catalysts for the Oxidative Dehydrogenation of Ethane/Propane Mixtures. *Industrial & Engineering Chemistry Research* **58**, 2170-2180, (2019).

175   Venegas, J. M. *et al.* Selective Oxidation of n-Butane and Isobutane Catalyzed by Boron Nitride. *ChemCatChem* **9**, 2118-2127, (2017).

176   Grant, J. T. *et al.* Boron and Boron-Containing Catalysts for the Oxidative Dehydrogenation of Propane. *ChemCatChem* **9**, 3623-3626, (2017).

177   Love, A. M. *et al.* Probing the Transformation of Boron Nitride Catalysts under Oxidative Dehydrogenation Conditions. *Journal of the American Chemical Society* **141**, 182-190, (2019).

178   Li, H. *et al.* O2 Activation and Oxidative Dehydrogenation of Propane on Hexagonal Boron Nitride: Mechanism Revisited. *The Journal of Physical Chemistry C* **123**, 2256-2266, (2019).

179   Muller, A. & Gouzerh, P. From linking of metal-oxide building blocks in a dynamic library to giant clusters with unique properties and towards adaptive chemistry. *Chemical Society Reviews* **41**, 7431-7463, (2012).

180   Beato, P. *et al.* Analysis of structural transformations during the synthesis of a MoVTeNb mixed oxide catalyst. *Applied Catalysis a-General* **307**, 137-147, (2006).

181   Mestl, G., Margitfalvi, J. L., Végvári, L., Szijjártó, G. P. & Tompos, A. Combinatorial design and preparation of transition metal doped MoVTe catalysts for oxidation of propane to acrylic acid. *Applied Catalysis A: General* **474**, 3-9, (2014).

182   Hagemeyer, A. *et al.* Catalyst material for oxidizing hydrocarbons, consisting of molybdenum, vanadium, niobium, tellurium, manganese, and cobalt. WO2013021034A1 (2013).

183   Hagemeyer, A. *et al.* Catalyst material for the oxidn. and/or the oxidative dehydrogenation of hydrocarbons. WO2013021020A1 (2013).

184   Valente, J. S. *et al.* Chemical, Structural, and Morphological Changes of a MoVTeNb Catalyst during Oxidative Dehydrogenation of Ethane. *ACS Catalysis* **4**, 1292-1301, (2014).

185   Tsuji, H., Oshima, K. & Koyasu, Y. Synthesis of Molybdenum and Vanadium-Based Mixed Oxide Catalysts with Metastable Structure: Easy Access to the MoVNbTe(Sb)Ox Catalytically Active Structure Using Reductant and Oxoacid. *Chemistry of Materials* **15**, 2112-2114, (2003).

186   Blom, D. A., Vogt, T., Allard, L. F. & Buttrey, D. J. Observation of Sublattice Disordering of the Catalytic Sites in a Complex Mo–V–Nb–Te–O Oxidation

Catalyst Using High Temperature STEM Imaging. *Topics in Catalysis* **57**, 1138-1144, (2014).

187 Pyrz, W. D. *et al.* Atomic-level imaging of Mo-V-O complex oxide phase intergrowth, grain boundaries, and defects using HAADF-STEM. *Proceedings of the National Academy of Sciences of the United States of America* **107**, 6152-6157, (2010).

188 He, Q., Woo, J., Belianinov, A., Guliants, V. V. & Borisevich, A. Y. Better Catalysts through Microscopy: Mesoscale M1/M2 Intergrowth in Molybdenum–Vanadium Based Complex Oxide Catalysts for Propane Ammoxidation. *ACS Nano* **9**, 3470-3478, (2015).

189 Masliuk, L. *et al.* Structural Complexity in Heterogeneous Catalysis: Cataloging Local Nanostructures. *Journal of Physical Chemistry C* **121**, 24093-24103, (2017).

190 Zhu, Y. Y. *et al.* Formation of Oxygen Radical Sites on MoVNbTeOx by Cooperative Electron Redistribution. *Journal of the American Chemical Society* **139**, 12342-12345, (2017).

191 Mestl, G. *et al.* Synthese eines MoVTeNb-Katalysators aus preisgünstigen Metalloxiden. DE 10 2017 000 861.2 (2017).

192 Mestl, G. *et al.* Synthese eines MoVNbTe-Katalysators mit reduziertem Gehalt an Niob und Tellur und höherer Aktivität für die oxidative Dehydrierung von Ethan. DE 10 2017 000 862.0 (2017).

193 Mestl, G. *et al.* Synthese eines MoVNbTe-Katalysators mit erhöhter spezifischer Oberfläche und höherer Aktivität für die oxidative Dehyxdrierung von Ethan zu Ethylen. DE 10 2017 000 865.5 (2017).

194 Oshihara, K., Hisano, T. & Ueda, W. Catalytic oxidative activation of light alkanes over Mo-V-based oxides having controlled surface. *Topics in Catalysis* **15**, 153-160, (2001).

195 Beckmann, W. in *Crystallization*   7-33 (Wiley-VCH Verlag GmbH & Co. KGaA, 2013).

196   Muller, A. *et al.* Archimedean synthesis and magic numbers: "Sizing" giant molybdenum-oxide-based molecular spheres of the keplerate type. *Angewandte Chemie-International Edition* **38**, 3238-3241, (1999).

197   Botar, B., Kogerler, P. & Hill, C. L. [{(Mo)Mo5O21(H2O)(3)(SO4)}(12)(VO)(30)(H2O)(20)](36-): A molecular quantum spin icosidodecahedron. *Chemical Communications*, 3138-3140, (2005).

198   Botar, B., Ellern, A., Sougrati, M. T. & Kogerler, P. Removing Compositional Boundaries in Mixed-Linker Keplerate Clusters. *European Journal of Inorganic Chemistry*, 5071-5074, (2009).

199   Petel, B. E., Brennessel, W. W. & Matson, E. M. Oxygen-Atom Vacancy Formation at Polyoxovanadate Clusters: Homogeneous Models for Reducible Metal Oxides. *Journal of the American Chemical Society* **140**, 8424-8428, (2018).

200   Ischenko, E. V. *et al.* Formation of active component of MoVTeNb oxide catalyst for selective oxidation and ammoxidation of propane and ethane. *Scientific Bases for the Preparation of Heterogeneous Catalysts: Proceedings of the 10th International Symposium* **175**, 479-482, (2010).

201   Oliver, J. M., Nieto, J. M. L., Botella, P. & Mifsud, A. The effect of pH on structural and catalytic properties of MoVTeNbO catalysts. *Applied Catalysis a-General* **257**, 67-76, (2004).

202   Schaffer, C., Todea, A. M., Gouzerh, P. & Muller, A. Spontaneous self-assembly of a giant spherical metal-oxide Keplerate: addition of one building block induces "immediate" formation of the complementary one from a constitutional dynamic library. *Chem Commun (Camb)* **48**, 350-352, (2012).

203   Trunschke, A. *et al.* The Impact of the Bulk Structure on Surface Dynamics of Complex Mo-V-based Oxide Catalysts. *ACS Catalysis* **7**, 3061-3071, (2017).

204   Shinotsuka, H., Tanuma, S., Powell, C. J. & Penn, D. R. Calculations of electron inelastic mean free paths. X. Data for 41 elemental solids over the 50 eV to 200 keV range with the relativistic full Penn algorithm. *Surface and Interface Analysis* **47**, 871-888, (2015).

205   Sanfiz, A. C. *et al.* Dynamics of the MoVTeNb Oxide M1 Phase in Propane Oxidation. *The Journal of Physical Chemistry C* **114**, 1912-1921, (2010).

206   Weber, T., Muijsers, J. C., van Wolput, J. H. M. C., Verhagen, C. P. J. & Niemantsverdriet, J. W. Basic Reaction Steps in the Sulfidation of Crystalline MoO3 to MoS2, As Studied by X-ray Photoelectron and Infrared Emission Spectroscopy. *The Journal of Physical Chemistry* **100**, 14144-14150, (1996).

207   Smith, M. R. & Ozkan, U. S. The Partial Oxidation of Methane to Formaldehyde: Role of Different Crystal Planes of MoO3. *Journal of Catalysis* **141**, 124-139, (1993).

208   Sawatzky, G. A. & Post, D. X-ray photoelectron and Auger spectroscopy study of some vanadium oxides. *Physical Review B* **20**, 1546-1555, (1979).

209   Bliznakov, G., Pesheva, Y., Klissurski, D., Marinov, M. & Kozhukharov, V. Methanol oxidation on V2O5MoO3TeO3 catalysts. *Applied Catalysis* **29**, 211-218, (1987).

210   Yun, Y. S. *et al.* Promoting effect of cerium on MoVTeNb mixed oxide catalyst for oxidative dehydrogenation of ethane to ethylene. *Applied Catalysis B: Environmental* **237**, 554-562, (2018).

211   Bahl, M. K., Watson, R. L. & Irgolic, K. J. X-ray photoemission studies of tellurium and some of its compounds. *The Journal of Chemical Physics* **66**, 5526-5535, (1977).

212   Geyer-Lippmann, J., Simon, A. & Stollmaier, F. Photoelektronenspektroskopie an Niobiodiden. *Zeitschrift für anorganische und allgemeine Chemie* **516**, 55-66, (1984).

213   Teixeira da Silva, V. L. S., Schmal, M. & Oyama, S. T. Niobium Carbide Synthesis from Niobium Oxide: Study of the Synthesis Conditions, Kinetics, and Solid-State Transformation Mechanism. *Journal of Solid State Chemistry* **123**, 168-182, (1996).

214   Dupin, J.-C., Gonbeau, D., Vinatier, P. & Levasseur, A. Systematic XPS studies of metal oxides, hydroxides and peroxides. *Physical Chemistry Chemical Physics* **2**, 1319-1324, (2000).

215   Sadakane, M., Kodato, K., Yasuda, N., Ishikawa, S. & Ueda, W. Thermal Behavior, Crystal Structure, and Solid-State Transformation of Orthorhombic Mo–V Oxide under Nitrogen Flow or in Air. *ACS Omega*, (2019).

216   Bhore, N. A., Klein, M. T. & Bischoff, K. B. Species rank in reaction pathways: Application of Delplot analysis. *Chemical Engineering Science* **45**, 2109-2116, (1990).

217   Bhore, N. A., Klein, M. T. & Bischoff, K. B. The delplot technique: a new method for reaction pathway analysis. *Industrial & Engineering Chemistry Research* **29**, 313-316, (1990).

218   Li, W.-Q., Fjermestad, T., Genest, A. & Rösch, N. Reactivity trends of the MoVOx mixed metal oxide catalyst from density functional modeling. *Catalysis Science & Technology*, (2019).

219   Dinda, S., Chiu, C.-c., Genest, A. & Rösch, N. Evaluation of density functionals for elementary steps of selective oxidation reactions. *Computational and Theoretical Chemistry* **1101**, 36-45, (2017).

220   Rugg, G., Genest, A. & Rösch, N. DFT Variants for Mixed-Metal Oxides. Benchmarks Using Multi-Center Cluster Models. *The Journal of Physical Chemistry A* **122**, 7042-7050, (2018).

9 List of Figures

10 List of Tables

11 List of Abbreviations

Å	Ångstrøm (10^{-8} m)	
at.-%	Fraction of atoms given in percent	
BET	Brunauer-Emmett-Teller method	
BJH	Barrett-Joyner-Halenda method	
°C	Degree Celsius	
C_n	Molecule containg n carbon atoms	
d	Lattice spacing	[Å]
DFT	Density functional theory	
E_A	Activation energy	[kJ mol^{-1}]
EG	Monoethylene glycol	
GC	Gas chromatography	
IMFP	Inelastic mean free path	[Å]
h	hour	
h^+	Hole in band	
HIM	Helium ion microscopy	
kJ	Kilojoule	
M	Metal site	
mg	Milligram (10^{-3} g)	
mL	Milliliter (10^{-9} m³)	
mmol	Millimol	
MvK	Mars-van-Krevelen (mechanism)	
n	Molar amount	[mol]
nm	Nanometer (10^{-9} m)	
OA	Oxalic acid	
ODH(-E)	Oxidative dehydrogenation (of ethane)	
p	Pressure	[Pa]
PFR	Plug flow reactor	

pH	pH value	
S	Selectivity	[%]
SEM	Scanning electron microscopy	
(HAADF-)STEM	(High angle annular dark field) scanning transmission electron microscopy	
t	Duration	[h]
T	Temperature	[K]
TOS	Time on stream	[h]
UV-vis	Ultra-violet to visible	
WHSV	Weight hourly space velocity	[h^{-1}]
wt.-%	Weight fraction given in percent	
X	Conversion	[%]
XRD	X-ray diffraction analysis	
(NAP-)XPS	(Near ambient pressure) X-ray photoelectron spectroscopy	
Y	Yield	[%]

12 Reprint permissions

13 List of publications

13.1 Journal contributions

Atomic-Scale Determination of Active Facets on the MoVTeNb Oxide M1 Phase and Their Intrinsic Catalytic Activity for Ethane Oxidative Dehydrogenation
D. Melzer, P. Xu, D. Hartmann, Y. Zhu, N. D. Browning, M. Sanchez-Sanchez, J.A. Lercher, Angew. Chem. Int. Ed. Engl. **2016**, 55, 8873-8877

Formation of Oxygen Radical Sites on MoVNbTeOx by Cooperative Electron Redistribution
Y. Zhu, P. V. Sushko, D. Melzer, E. Jensen, L. Kovarik, C. Ophus, M. Sanchez-Sanchez, J.A. Lercher, N.D. Browning, J. Am. Chem. Soc. **2017**, 139, 12342-12345

Design and synthesis of highly active MoVTeNb-oxides for ethane oxidative dehydrogenation
D. Melzer, G. Mestl, K. Wanninger, Y. Zhu, N.D. Browning, M. Sanchez-Sanchez, J. A. Lercher, Nature Comm. **2019**, 10, 4012

Intrinsic Kinetic Model for Oxidative Dehydrogenation of Ethane over MoVTeNb Mixed Metal Oxides: A Mechanistic Approach
P.J. Donaubauer, D.M. Melzer, K. Wanninger, G. Mestl, M. Sanchez-Sanchez, J.A. Lercher, O. Hinrichsen, Chem. Eng. J., **2019**, 383, 123195

On the promoting effects of Te and Nb in the activity and selectivity of M1 MoV-oxides for ethane oxidative dehydrogenation
D. Melzer, G. Mestl, K. Wanninger, A. Jentys, M. Sanchez-Sanchez, J.A. Lercher, Top. Catal., **2020**, submitted

13.2 Oral presentations

Low temperature crystallized M1-MoVTeNbOx for oxidative dehydrogenation of ethane
D. Melzer, G. Mestl, K. Wanninger, M. Sanchez-Sanchez, J.A. Lercher, World Congress of Oxidation Catalysis, Krakow, Poland, September 6th, 2017

Tuning particle properties of M1-MoVTeNb mixed oxide catalysts for outstanding activity in oxidative dehydrogenation of ethane
D. Melzer, J. Tseglakova, G. Mestl, K. Wanninger, Y. Zhu, N.D. Browning M. Sanchez-Sanchez, J.A. Lercher, DGMK conference, Dresden, Germany, October 9th, 2017

Imaging M1-MoVTeNbOx catalyst using environmental STEM: Electronic and structural changes under catalytically relevant conditions
D. Melzer, Y. Zhu, P. V. Sushko, N. D. Browning, M. Sanchez-Sanchez, J. A. Lercher, 13th European Congress on Catalysis, Florence, Italy, August 27th, 2017

Investigating ethane oxidative dehydrogenation over MoVNbTeOx catalysts by environmental STEM
Y. Zhu, E. Jensen, P. Sushko, L. Kovarik, D. Melzer, C. Ophus, M. Sanchez-Sanchez, J. A. Lercher, N. D. Browning, Materials Research Society 2016 Fall Meeting, Boston, MA, USA, November 29th, 2016

13.3 Poster presentations

Oxidative dehydrogenation of ethane over microporous Mo-V-Bi mixed oxides
D. Melzer, T. Schachtl, M. Sanchez-Sanchez, J. A. Lercher, 49. Jahrestreffen Deutscher Katalytiker, Weimar, Germany, March 16th – 18th, 2016

Oxidative Dehydrogenation of Ethane
P. Donaubauer, D. Melzer, M. Sanchez-Sanchez, O. Hinrichsen, J.A. Lercher, ScienceTalks@Clariant, Frankfurt am Main, Germany, July 7th, 2017

Crystallization of MoVTeNbOx for ethane oxidative dehydrogenation
D. Melzer, M. Sanchez-Sanchez, G. Mestl, K. Wanninger, J.A. Lercher, 51. Jahrestreffen Deutscher Katalytiker, Weimar, Germany, March 14th – 16th, 2018

Direct crystallization of highly active MoVTeNbOx M1 phase under hydrothermal conditions

D. Melzer, G. Mestl, K. Wanninger, M. Sanchez-Sanchez, J.A. Lercher, 12th International Symposium on the "Scientific Bases for the Preparation of Heterogeneous Catalysts", Louvain-La-Neuve, Belgium, July 8th – 12th, 2018

Role of M1-MoVTeNb metal oxide composition on the activity and selectivity in ethane oxidative dehydrogenation

D. Melzer, M. Sanchez-Sanchez, G. Mestl, K. Wanninger, J.A. Lercher, 52. Jahrestreffen Deutscher Katalytiker, Weimar, Germany, March 13th – 15th, 2019

Oxidative Dehydrogenation of Ethane over MoVTeNb Mixed Metal Oxides: Kinetic Investigation and Modelling

P.J. Donaubauer, D.M. Melzer, M. Sanchez-Sanchez, K. Wanninger, G. Mestl, J.A. Lercher, O. Hinrichsen, 52. Jahrestreffen Deutscher Katalytiker, Weimar, Germany, March 13th – 15th, 2019

M1-MoVTeNb metal oxide catalysts with high intrinsic activity in ethane oxidative dehydrogenation

D. Melzer, G. Mestl, K. Wanninger, Y. Zhu, M. Sanchez-Sanchez, J. Lercher, Europacat 2019, Aachen, Germany, August 19th – 23rd

Oxidative Dehydrogenation of Ethane over MoVTeNb Mixed Metal Oxides: Kinetic Investigation and Modeling

P. Donaubauer, D. Melzer, M. Sanchez-Sanchez, K. Wanninger, G. Mestl, J. Lercher, O. Hinrichsen, Europacat 2019, Aachen, Germany, August 19th – 23rd

13.4 Patents

Synthese eines MoVTeNb-Katalysators aus preisgünstigen Metalloxiden. DE 10 2017 000 861.2. 2017
G. Mestl, K. Wanninger, D. Melzer, M. Sanchez Sanchez, J. Tseglakova, J. Lercher

Synthese eines MoVNbTe-Katalysators mit erhöhter spezifischer Oberfläche und höherer Aktivität für die oxidative Dehydrierung von Ethan zu Ethylen. DE 10 2017 000 865.5. 2017
G. Mestl, K. Wanninger, D. Melzer, M. Sanchez Sanchez, J. Tseglakova, J. Lercher

Synthese eines MoVNbTe-Katalysators mit reduziertem Gehalt an Niob und Tellur und höherer Aktivität für die oxidative Dehydrierung von Ethan. DE 10 2017 000 862.0. 2017 .
G. Mestl, K. Wanninger, D. Melzer, M. Sanchez Sanchez, J. Tseglakova, J. Lercher

13.5 Awards

ScienceTalks@Clariant, Frankfurt am Main, Germany, July 7th, 2017, Best Poster Award: Second price

51. Jahrestreffen Deutscher Katalytiker, Weimar, Germany, March 14th – 16th, 2018, Best Short Presentation in Poster Workshop: Dehydrogenation

12th International Symposium on the "Scientific Bases for the Preparation of Heterogeneous Catalysts", Louvain-La-Neuve, Belgium, July 8th – 12th, 2018, Best Poster Award